Rare-Earth Elements Doped Novel Photonics Sources

Nitin Saurabh Jha

A dissertation submitted for the degree of Doctor of Philosophy

Heriot-Watt University

School of Engineering and Physical Sciences

July 2018

A B S T R A C T

This thesis presents the work carried out on the development of novel photonic sources based in rare-earth doped ions. It discusses in detail the properties of rare earth ions and its applications. The three major components of this work, namely, rare-earth doped solid state hosts, rare-earth doped speciality fibres, and rare-earth doped waveguide lasers have been presented in different chapters.

The host glasses for the rare-earth doped gain mediums have been prepared by the traditional melt-quenching technique and spectroscopic studies have been carried out on them. Experiments to realise multi-wavelength lasers operating in the visible range have been carried out on the samarium doped phosphate glasses, owing to samarium's unique multiple emission peaks at 561 nm, 596 nm, and 643 nm with violet-blue excitation. Due to the relatively low emission cross section value of trivalent samarium ions (3.911 X 10^{-22} cm^2 at 596 nm), it requires a much higher pump power. Due to the lack of high pump power diodes in the violet wavelength range, laser action could not be demonstrated. Further spectroscopic investigations on the samarium doped glasses and crystals revealed that the presence of excited state absorption could be a factor as well which discourages the realisation of laser emission in the sample.

Rare-earth doped multicore optical fibres have been designed and fabricated for the realisation of active multiplexer elements and multi-wavelength lasers. Optical fibres with six cores and two cores respectively have been fabricated. Each of the six cores of the fibre were doped with erbium with the aim to develop active multiplexer elements which could incorporate multiplexing and amplification together. The cores showed considerable gains, with the maximum gain of around 30 dB – 40 dB in the wavelength range of 1500 nm – 1600 nm. The cores of the two core fibre were doped with ytterbium and erbium/ytterbium with the aim to demonstrate simultaneous laser

action at 1 μm and 1.5 μm. The fibre, upon cladding pumping at 976 nm, demonstrated simultaneous laser emissions at 1061 nm and 1536 nm from the ytterbium and erbium/ytterbium doped cores, respectively. The laser action was observed with Fresnel reflection from the parallel cleaved facets of the fibre. The slope efficiency of the emission for both the cores were ~1%, which is quite low, considering the Fresnel reflection lasing.

CW modelocked waveguide laser has been demonstrated in ytterbium doped bismuthate glasses. The waveguides were inscribed by the ultrafast laser inscription technique. The waveguide laser operated at the repetition rate of around 1.94 GHz with the pulse duration of about 1.1 ps at the wavelength of 1029 nm.

To my parents

ACADEMIC REGISTRY
Research Thesis Submission

Name:	Nitin Saurabh Jha		
School:	IPaQS, EPS		
Version: *(i.e. First, Resubmission, Final)*	Final	Degree Sought:	PhD Physics

Declaration

In accordance with the appropriate regulations I hereby submit my thesis and I declare that:

1) the thesis embodies the results of my own work and has been composed by myself
2) where appropriate, I have made acknowledgement of the work of others and have made reference to work carried out in collaboration with other persons
3) the thesis is the correct version of the thesis for submission and is the same version as any electronic versions submitted*.
4) my thesis for the award referred to, deposited in the Heriot-Watt University Library, should be made available for loan or photocopying and be available via the Institutional Repository, subject to such conditions as the Librarian may require
5) I understand that as a student of the University I am required to abide by the Regulations of the University and to conform to its discipline.
6) I confirm that the thesis has been verified against plagiarism via an approved plagiarism detection application e.g. Turnitin.

* *Please note that it is the responsibility of the candidate to ensure that the correct version of the thesis is submitted.*

Signature of Candidate:		Date:	01/07/2018

Submission

Submitted By *(name in capitals)*:	NITIN SAURABH JHA
Signature of Individual Submitting:	
Date Submitted:	

For Completion in the Student Service Centre (SSC)

Received in the SSC by *(name in capitals)*:			
Method of Submission *(Handed in to SSC; posted through internal/external mail)*:			
E-thesis Submitted ***(mandatory for final theses)***			
Signature:		Date:	

Please note this form should be bound into the submitted thesis.
Academic Registry/Version (1) August 2016

ACKNOWLEDGEMENTS

I would like to thank my supervisor Professor Ajoy Kar for his invaluable guidance and support throughout my PhD. I am grateful to him for giving me the opportunity to carryout meaningful research under his supervision. I sincerely thank him for his optimistic attitude and continuous encouragement which has made this journey a lot easier and enjoyable.

I would like to take this opportunity to thank my second supervisor Dr Henry Bookey, who helped me with his valuable suggestions and discussions during the early days of my PhD which helped me get well acquainted with fibre optics. His timely inputs and suggestions throughout my PhD has been a great help as well.

I thank our collaborators at CSIR-CGCRI for fabricating the multicore fibres for us. I thank Dr Mukul Paul, Dr Mrinmay Pal, Dr Anirban Dhar, and Dr Shyamal Das, without whom, my work on fibre optics would not have been possible. I thank all the technical staff at CGCRI who were involved in the fabrication of the fibres as well.

I would like to express my gratitude toward Professor C K Jayasankar at Sri Venkateswara University, Tirupati for fabricating the rare-earth doped glasses for my work. I am also grateful to Devaraj and Venkat for their work in developing these glasses and also visiting and working in our labs at Heriot Watt.

I would like to thank Professor Günter Huber from University of Hamburg for allowing me to work in his labs. I would also like to thank Daniel-Timo Marzhal for his help and support in the labs at University of Hamburg.

I would like to thank our previous group members including Rose, who introduced me to ULI and showed me all the labs on my first day at Heriot Watt, Ashley, who helped me with my work with fibre optics, and Adam, for training me on waveguide lasers. I

would also like to thank our current group members including Mark, James, Fiona, and Giorgos for their help in and around the labs.

I am extremely thankful to my friends Shraddha, Anusha, and Hari, who made my life in Edinburgh a lot more enjoyable and unforgettable.

I would like to thank Scottish Universities of Physics Alliance (SUPA) for granting me a funding to carry out short term research at CGCRI, India. The research work in fabricating speciality optical fibres carried out with this funding was truly remarkable and helped me consolidate my knowledge in fibre optics.

I would also like to extend my gratitude towards the student support office for providing me with the help and support during my PhD.

I am ever thankful to my landlords, Albert and Fulmaya for making me feel at home over the last year. I would like to thank you both for all the meals and warmth.

I am also thankful to my partner, Hayley for the love and care she has shown during my PhD. She has been an inspiration and a pillar of support during the times of need.

Last, but not the least, I would like to thank my parents for putting their trust in me. I cannot thank them enough for going beyond their means to ensure that I get the best of the opportunities. I am also thankful to my siblings, Rashmi, Shipra, and Ishan for their love and support.

PUBLICATIONS BY THE AUTHOR

Peer reviewed journals:

1. **Nitin Jha**, Mukul C Paul, Ajoy K Kar, Anirban Dhar, Shyamal Das, Jayanta K Sahu, and Henry T Bookey, "Simultaneous Dual Wavelength Laser Operation at 1.06 μm and 1.53 μm in a Two-Core Fiber", under preparation for Optics Express.

2. **Nitin Jha**, Daniel-Timo Marzhal, Venkataiah Godugunuru, G. Devarajulu, K Linganna, C K Jayasankar, Gunter Huber, and Ajoy Kar, "Spectroscopic Investigations into the Excited State Absorption of Samarium Ions Doped Glasses and Crystals", under preparation for Optics Material Express

Conference papers

1. Adam Lancaster, Amol Choudhary, **Jha S. Nitin**, Rose Mary, David P. Shepherd, and Ajoy K. Kar. "1.94 GHz CW Modelocked Ytterbium Doped Bismuthate Glass Waveguide Laser", Advanced Solid State Lasers (Optical Society of America, 2015) October 2015. https://doi.org/10.1364/ASSL.2015.AM5A.22

2. **Nitin Jha**, K Linganna, C K Jayasankar, and Ajoy Kar, "Sm3+ Ions Doped Phosphate Glasses for Multiband Visible Laser Applications", CLEO: Science and Innovations OSA Technical Digest (online) (Optical Society of America, 2015) May 2015. https://doi.org/10.1364/CLEO_AT.2015.JTh2A.23

3. **Nitin Jha**, Ajoy Kumar Kar, Mukul C. Paul, Mrinmay Pal, Anirban Dhar, Shyamal Das, Jayanta K. Sahu, M. Nunez Velazquez, and Henry T. Bookey, “Multicore Optical Fibers for Multi-band Laser and Amplifier Applications”, 12th International Conference on Fiber Optics and Photonics. December 2014. https://doi.org/10.1364/PHOTONICS.2014.M2A.5

TABLE OF CONTENTS

LIST OF ABBREVIATIONS

ASE : Amplified Spontaneous Emission

CW : Continuous Wave

CWML : Continuous Wave Mode-Locking

EDFA : Erbium Doped Fibre Amplifier

ESA : Excited State Absorption

fs : Femto Second

IR : Infra-Red

LASER : Light Amplification by Stimulated Emission of Radiation

LIDAR : Light Detection And Ranging

MASER : Microwave Amplification by Stimulated Emission of Radiation

MCF : Multi-Core optical Fibre

MFC : Mass Flow Controller

MCVD : Modified Chemical Vapour Deposition

NA : Numerical Aperture

NIR : Near Infra-Red

ns : Nano Second

OVD : Outside Vapour Deposition

PCVD : Plasma Chemical Vapour Deposition

QML : Q-switched Mode-Locking

RE : Rare Earth

RI : Refractive Index

SDM : Space Division Multiplexing

SLD : Super Luminescence Diode

ULI : Ultrafast Laser Inscription

VAD :Vapour phase Axial Deposition

WDM : Wavelength Division Multiplexing

LIST OF FIGURES

LIST OF TABLES

तमसो मा ज्योतिर्गमय

(From darkness, lead me to light)

Chapter1

I N T R O D U C T I O N

1.1Background and Motivation

Eastern philosophers and ancient civilisations such as the Babylonians and the Egyptians believed that the universe was created by higher powers and the effects of the battles between them. On the other hand, they also had developed and mastered mathematics and philosophy. Although there might not be a direct relation between ancient philosophy and light, it sure has influenced and formed a basis for our modern thought process. Two of the most dominant aspects of nature that most people seem to be aware of are gravity and light. The effect of gravity is very obvious in everyday life and most people seem to be familiar with it. On the other hand, they are not quite aware of the extent of the impact that light, or the electromagnetic radiation has beyond the visible part of the spectrum. From eyesight to the internet, from communication to displays, the electromagnetic radiations rule our world.

From worshipping the sun, the primary source of natural light and inventing fire, humankind has come a long way. We have now found new ways to generate, control, and manipulate light. It has taken centuries of continuous research and extensive studies to understand the basic nature of light. A lot of different theories have been proposed over time to explain the true nature and predict the behaviour of light. The brightest minds of the last few centuries have tried to find out whether light behaved as a wave or particles. The Greeks thought of them as particles, and then Huygens in the 17^{th} century proposed they were waves. It was Newton who came up with the famous corpuscular theory of light suggesting the particle nature of light. Young soon after demonstrated his celebrated double slit experiment establishing the wave nature of light. The Scottish physicist, James Clerk Maxwell published his four equations

[11] that completely described how the electromagnetic waves behave which almost ended the battle on understanding and manipulating electromagnetism.

Einstein then proposed the particle nature of light in the beginning of the 20th century, and finally quantum mechanics established that it's both waves and particles.

Einstein continued to pioneer the research in electromagnetic theory and published one of his most celebrated papers in 1917 on the quantum theory of radiation [12], which was going to have a deep impact on the technological development associated with light. It predicted the phenomenon of "stimulated emission" which forms the foundation for the modern technology marvel we now know as lasers. Laser is an acronym for Light Amplification by the Stimulated Emission of Radiation. Charles Townes was the first person to utilise Einstein's theoretical work on stimulated emission to demonstrate a working device, which he called a MASER (Microwave Amplification by Stimulated Emission of Radiation) in 1953 demonstrating the amplified stimulated emission of electromagnetic radiation in the microwave range. It was not until 1960 when Theodore Maiman first demonstrated a working laser, operating in the visible spectrum [13], and it was referred to as "a solution seeking a problem" at first. But soon it triggered a surge of research and interest in this filed which led to the invention of a wide range of lasers operating at different wavelengths.

Currently, the laser industry is worth billions of pounds worldwide. Lasers have evolved as a multi-faceted and versatile tool for a myriad of applications, ranging from correcting vision defects, to cutting through steel and other materials, from scanning prices in super markets to applications in optical communication and data storage. The year 2010 was celebrated as the "50 years of lasers" to commemorate its remarkable progress. The approach behind laser development has seen a paradigm shift with the development of science, technology and medicine through these years with the need

for application specific lasers increasing manifolds. Therefore, after decades of continuous development and innovation, the field of laser technology still presents itself with endless possibilities in terms of applications.

The first laser demonstrated by Maiman operated at 694 nm and was based in ruby as the lasing medium. The first operation of laser in gaseous medium was demonstrated by Javan et al in 1960 [14] and used a mixture of He-Ne as the active medium. This laser operated at 1153 nm, but its operation in the visible range at 632.8 nm is preferred for various applications including laboratory demonstrations, bar-code readers, optical disc readers, and many more. It was realised soon that lasers could be useful in material processing and high power CO_2 lasers have been a revolution in this field. They have been extensively used in laser cutting, welding, and laser marking. With the development of semiconductor technology, diode lasers came into existence with direct applications in optical communication, as pump source for other lasers, laser printers, and laser pointers. All these lasers operate in the continuous wave (CW) mode, but certain applications required high peak power operation, which was not achievable with the CW lasers. This need resulted in the development of pulsed lasers with much higher irradiance in each pulse, which enabled the nonlinear interaction of light with matter through multiphoton absorption. These short pulses of laser have also found applications in studying the ultrafast dynamics of matter and commonly used in ultrafast laser spectroscopy.

With the multi-dimensional applications of lasers in every walk of life, researchers all around the globe have been looking into a large number of potential gain media including different solid state materials, doped with active ions, with emission wavelengths ranging from soft X-rays to the far infrared region of the electromagnetic spectrum. One of the most exciting groups of elements that have particularly led to a

lot of meaningful research are the rare-earth elements. The rare-earth elements consist of the fifteen lanthanide elements in the sixth row of the periodic table stretching from lanthanum to lutetium along with scandium and yttrium. Among many others, the photonic applications of the rare-earth elements include solid state lasers in the visible and infrared wavelengths, lasers in semiconductor materials, primarily Si [15], light emitting diodes operating in the visible and infrared [16], glass optical fibres for telecommunications [17], [18], [19], optical data storage, and displays [20].

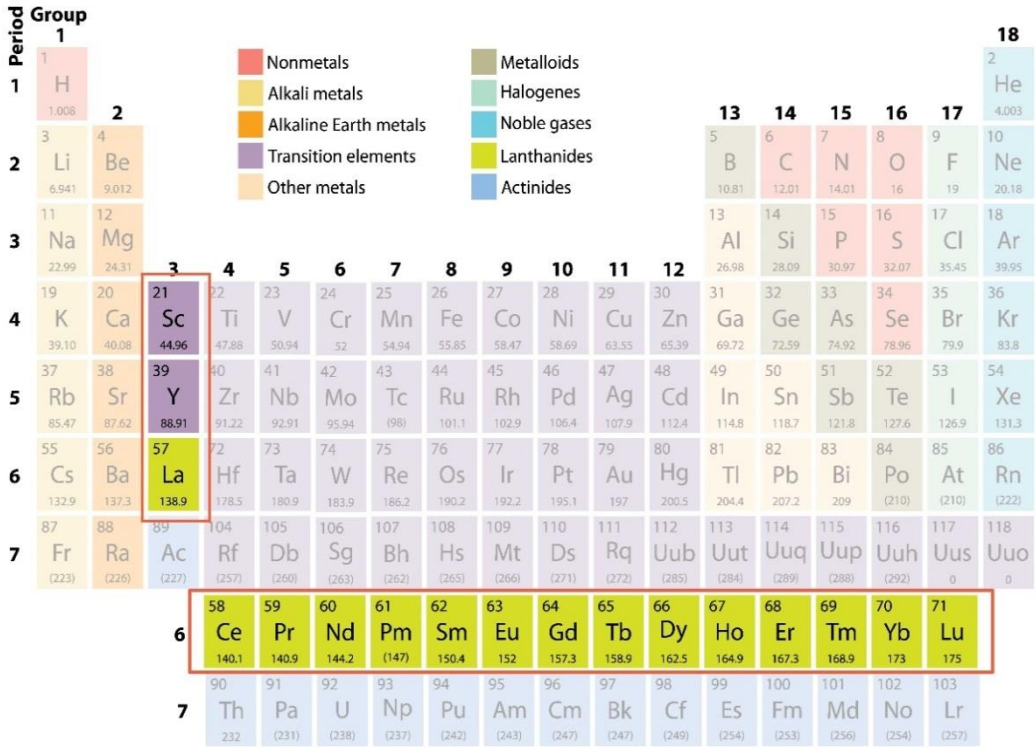

Figure 1. 1: Position of rare-earth elements or the Lanthanides in the periodic table [21]

The ever increasing demand of optical sources with applications in lighting and lasers has caused a rapid growth in the field of luminescence from rare-earth elements. Rare-earth elements have been revolutionary in the telecommunication industry by providing as active materials for lasers and amplifiers operating at wavelengths compatible with fibre telecommunication technology. Rare-earth materials have been

known for their luminescence properties for a very long time. It was in the year 1968, when the energy levels of lanthanide ions were investigated and reported first [22]. They have found applications in luminescent devices in the form of glasses, crystals and powders and have been used as an active ion in phosphors for CRT displays. The luminescence from the triply charged ions of erbium (Er^{3+}), europium (Eu^{3+}), terbium (Tb^{3+}), and cerium (Ce^{3+}) have been used to produce the red, green and blue for displays. Their emissions in the infrared region have also been extensively utilised for different laser sources. Figure 1.2 below shows the emission wavelengths of different rare-earth elements.

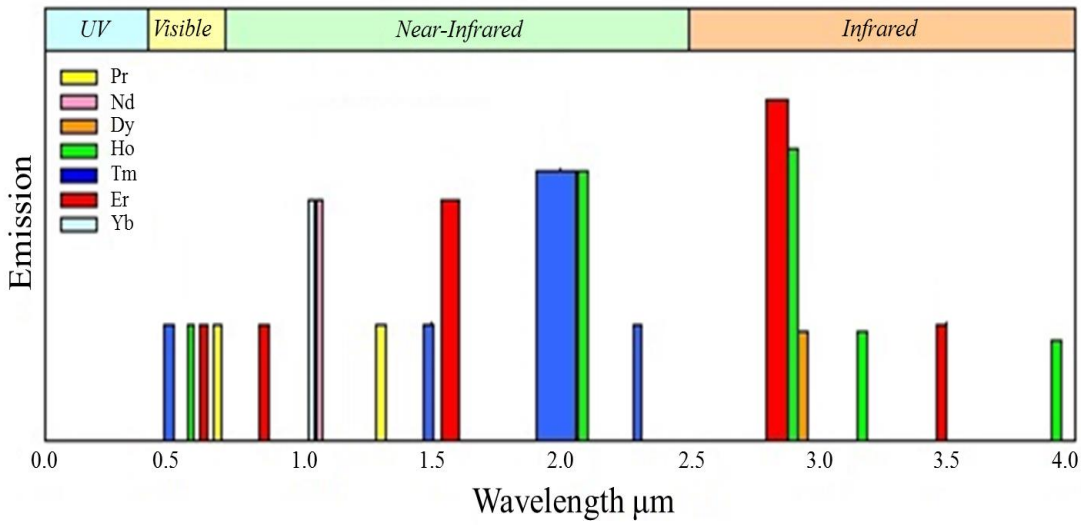

Figure 1. 2: Emission wavelengths of different rare-earth elements [2]

The majority of research in the 1960s was devoted in developing novel solid state lasers. One of the most important outcomes of this research was the development of neodymium based lasers. The first report of neodymium based laser came from Elias Snitzer [23] in 1961,where he reported achieving laser action in barium crown glass with neodymium ions. This work was immediately followed by the demonstration of Nd:YAG laser, which was reported in 1964 by Geusic, Marcos, and Van Uitert [24].

Nd:YAG lasers, since then have found applications in surgery [25] [26], manufacturing, and military. Ytterbium emerged as one of the alternatives for neodymium for lasers operating at 1 μm and is one of the other rare-earth elements which has been investigated extensively. It has a simple quasi-three-level system ensuring the absence of the detrimental excited state absorption and cross relaxation induced quenching. Ytterbium doped gain media have been in existence for a reasonably long time and its usefulness has been quite established [27], [28], [29]. It's now one of the most common and well established element for applications into high power fibre lasers operating a 1 μm.

Erbium, on the other hand, has been one of the most celebrated rare earth elements over few decades and found enormous applications as fibre amplifiers [30], [31] in telecommunications. The primary reason of the success of trivalent erbium, if one considers the telecommunication industry in particular, is that the ultra-low loss window of silica based optical fibres (1450 nm-1600 nm) coincides with its emission band around 1535 nm corresponding to the $^4I_{13/2}$-$^4I_{15/2}$ transition of the Er^{3+} ion.

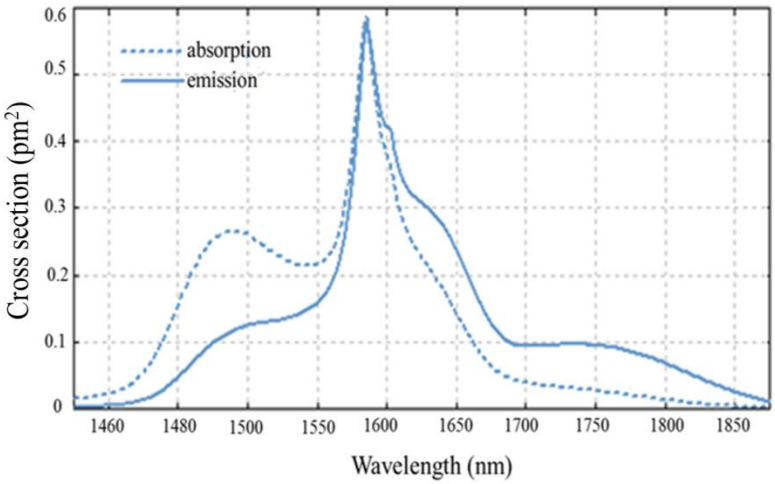

Figure 1. 3:Absorption and emission cross-section spectrum of the Er^{3+} ion in a phosphate host [32]

The development of erbium doped fibre amplifier (EDFA) in the 1980s [33], [34] allowed the transmission as well as amplification of optical signals in the telecommunication range, eradicating the need of expensive optical and electronic components. It has enabled a great deal of progress in long haul telecommunications, and has helped to standardise the 1.5 μm band as the communication band of choice. One of the major advantages that EDFA offered was the capability to produce gain at different wavelengths simultaneously, which are from 1525 nm to 1565 nm in the C-band, or the conventional band, and from1570 nm to 1610 nm in the long or L-band which is a great asset for applications into wavelength division multiplexing (WDM).

The versatility of rare earth elements is quite evident from the fact that they have also shown a lot of potential for applications in the visible spectrum of laser emission. Some of the most prominent ions which have been extensively studied for applications into visible luminescence are samarium, dysprosium, holmium, and praseodymium. Recent work in dysprosium has shown lasing in the yellow region at 583 nm [35]. An extensive study on the possibility of dysprosium as a viable material for white light luminescence has also been reported [20]. Praseodymium has proved to be quite a versatile material for visible laser applications. Laser operation in praseodymium doped crystals in the green, yellow and red spectral range has recently been reported by [36], [37]. Laser emission in the orange (607 nm) has also been reported by [38] recently. The first visible laser in holmium was reported back in 1965 by with a Xe-lamp pumping under cryogenic conditions. Room temperature laser operation was also reported for flash lamp pumped Ho:$YAlO_3$ by Kaminskii et al. [39].

It is quite evident from the research carried out in the past few decades that rare-earth elements have been exploited fully as active ions in both bulk and fibre media. One of the relatively recent advancements in this field has been the development of laser

inscribed waveguides in rare-earth doped media. The success of this technology could be attributed to the evolution of ultrafast lasers which are instrumental in inscribing these waveguides in the substrates. Laser realisation in different substrates, including glasses and crystals have been demonstrated by various groups operating at different wavelengths ranging from visible to infrared region [40], [41], [42]. The waveguide configuration has various advantages over the bulk media such as excellent beam confinement and good spatial overlap between the pump and the signal, resulting in improved laser efficiencies and lower pumping thresholds. These laser inscribed waveguides are also helping design compact and efficient sources of ultrafast lasers with high repetition rates [43], [44].

1.2 Scope of the thesis

Rare-earth elements have served the photonics and telecommunication industry for over half a century now. Their presence is inevitable and indispensable in all walks of life. Given the potential for applications in a wide range of fields, it is important that the technology involving the rare-earth elements should keep evolving. This requires a continuous and innovative approach in the research and development of novel optical devices, including lasers, amplifiers and luminescence sources.

The work presented in this thesis aims to develop photonic sources, with an emphasis on lasers operating at different wavelengths, ranging from the visible to the infrared range of the electromagnetic spectrum. It encompasses detailed theoretical and experimental investigations in order to exploit the fascinating advantages that rare-earth elements offer.

The research entails a very realistic approach of first investigating the materials for the active ions and hosts and then developing them into practical devices using state of the art technology, such as ultrafast laser inscription tools, optical fibre fabrication, stable

characterisation rigs, and advance mathematical tools. The active ions and hosts were selected keeping their applications in metrology, communication and spectroscopy in mind. The material development stage consisted of the development of the doped glasses, both for bulk and fibre applications. The glasses and fibres were characterised in order to assess their losses, absorption, emission, and propagation properties. This step was crucial in order to ensure the continuous improvement in the design parameters.

The work presented through this thesis is also quite unique in a way that it combines different technologies such as optical fibre fabrication, bulk media preparation, and ultrafast laser inscription technologies together in order to develop compact photonic devices. This work has gotten the best out of the current existing technologies and succeeded in giving more dimensions to the current domain of rare-earth elements technology.

1.3 Thesis Outline

The thesis has been structured in a way to incorporate different techniques separately, while they are combined together with the common aim to exploit the novel properties of rare-earth doped materials. The thesis follows the structure summarised below:

Chapter 2 discusses the spectroscopic properties of the rare-earth elements, with emphais on the ions used in this work. It also describes in detail the methods used for the preparation of the materials, including bulk media and optical fibres. It also introduces and discusses the ultrafast laser inscription (ULI) technology which has been used to inscribe channel waveguides in glass substrates.

Chapter 3 introduces the concept of multicore optical fibres (MCFs) and compares all the existing technologies based on it. It gives insight on the historical background and

future prospects of MCFs. It also gives some theoretical background on the propagation of light through waveguides. It also includes the details of the experimental work done with the MCFs such as characterisartion and laser realisation.

Chapter 4 investigates the spectroscopic properties of samarium in particular, within different host materials. It entails the details on the absorption and emission preoperties of samarium ions. It includes the experiments carried out to realise bulk lasers operating in the visible range. Further spectroscopic experiments are conducted to explore the deterring factors in realising the laser action with the material, such as excited state absorption and bleaching.

Chapter 5 deals with ytterbium ions as the active medium, doped in bismuthate glasses. It incorporates a bulk laser cavity followed by experiments on CW modelocking of the laser. ULI based waveguides in the same material have also been investigated and presented.

Chapter 6 summarises the results obtained in the thesis and analyses their impact. Conclusive remarks have been made and future implications and work have been discussed.

Chapter 2

MATERIALS AND METHODS

2.1 Introduction

Rare-earth elements have been the seeds of technology for the past few decades for they have been instrumental in bringing about the revolution in the fields of photonics [45], [46], [47], electronics, telecommunication [48], and defence [49]. The extent to which these elements have influenced and shaped modern technology is remarkable [50] [51], [52], [53]. This has been possible because of the extensive research that has gone into understanding the elementary nature and properties of these elements [54] [17, 55]. This chapter aims to present a detailed description of the electronic and optical properties of some of the important rare-earth elements in context of the thesis. These elements are important in the context of the work presented in this thesis and in the global research scenario as well. Some of these elements are erbium, which has revolutionised the field of optical telecommunication [33], ytterbium, which is widely being employed in tuneable sources around 1 μm [56], and samarium, which has shown vast promises for applications in visible sources [57, 58]. The motive is to discuss the properties that make them stand out as desirable materials for photonic applications.

Meanwhile, if we consider the optical communication's most celebrated work with erbium doped fibre amplifiers (EDFA) [48], or the demonstration of ultra-compact waveguide lasers [59], the rare-earth revolution has been fuelled by the parallel technologies that have developed alongside, with state of the art glass and fibre fabrication setups [60], [61], modern telecommunication systems, and ultrafast laser inscription (ULI) technology [62] being a few of them. In order to understand the

impact of rare-earth elements, it is important to discuss the technologies associated with them as well. Therefore, this chapter also aims to introduce the technologies that have been contributory in the development of rare-earth elements as the "technology metals". The following sections describe the details of the processes involved in this work, which are, optical fibre drawing, glass preparation, and ultrafast laser inscription. All of these three techniques have been instrumental in the realisation of photonic devices and serve as the basis of this thesis.

Optical fibre fabrication is a sophisticated process and all the steps involved need proper attention. The steps involved in the fibre fabrication, ranging from preform fabrication to fibre drawing have been discussed in detail in section 2.4. The fibres produced for this work through this method are multi-core, multiple rare-earth doped fibres with potential applications in multi-band lasers and amplifiers [63]. The novel design of the fibres also resulted in a new technique of fibre fabrication, which involves the formation of composite preforms, which also has been described.

The success of rare-earth based devices also relies on the availability of suitable host materials. It requires the development of appropriate glasses and crystals to serve as hosts for the rare-earth dopants. The glasses chosen for this work were fluorophosphates glasses, which have been selected for various advantages over others, which are discussed in the following sections. This chapter incorporates the processes involved in the fabrication of phosphate glasses for the visible laser development work. Samarium doped glasses have been developed for applications into lasers operating in the yellow-orange range of the spectrum.

The ULI technology has been instrumental in miniaturising the laser circuitry and forms a significant component of the work. This technique has been used to fabricate buried channel waveguides in different substrates in order to demonstrate compact,

ultrafast waveguide lasers. A few different substrates, such as phosphate and bismuthate glasses have been used for waveguide fabrication with this technique. The process of the optimisation of parameters for waveguide fabrication has been discussed along with the details of the experimental set up.

2.2 Rare-earth elements and their properties

Despite their name, the rare-earth elements are available in plentiful amounts in nature. They are not quite rare, but they tend to exist together in compounds. Large deposits of rare-earth elements are found in Scandinavia, South Africa, China, and Australia. Rare-earth elements are a group of seventeen elements belonging to the periodic table, including fifteen lanthanides as well as scandium and yttrium.

This group of elements has baffled chemists for a very long period of time. Each of these elements form the same type of compounds with very similar properties, and the elements could themselves be identified from each other by relatively small differences in solubilities and molecular weights of the compounds they formed [64]. The optical and electronic properties of these elements make them irreplaceable in the world of technology. The physical and opto-electronic properties are being discussed in the following sections.

a. Physical properties

Rare-earth elements share many common properties, which make them quite difficult to separate. They are generally silver, silvery-white or grey in appearance. They have high lustre, but tarnish quite readily in air. The solubility of the rare-earth elements differs very slightly. They usually have high electrical conductivities. They are found with non-metals, usually in the 3+ oxidation state.

b. Opto-electronic properties

The rare-earth elements are the group of chemically similar elements with partially filled 4f shell in common. These elements usually take on a 3+ ionic state (RE^{3+}), while the 2+ ionic states are also known to exist. The RE^{3+} states are known to be much more stable as they are predominantly independent of their surrounding due to the shielding of the 4f electronic levels from external field by $5s^2$ and $5p^6$ outer shell electrons.

The 3+ ions all exhibit intense narrow-band intra-4f luminescence in a wide variety of hosts, and the shielding provided by the $5s^2$ and $5p^6$ electrons means that rare-earth radiative transitions in solid hosts resemble those of the free ions and electron–phonon coupling is weak. Although some of the divalent species such as samarium and europium also exhibit luminescence, it is the trivalent ions that are of most interest.

Figure 2.1 shows energy level diagrams for the isolated 3+ ions of each of the 13 lanthanides with partially filled 4f orbitals from cerium (n=1) to ytterbium (n=13). It also shows the emission levels and wavelengths of the elements. Most of the rare-earth (RE^{3+}) emissions are within the f-manifold. Nevertheless, for some ions such as Eu^{2+} and Ce^{3+}, broad band emissions are also known. In these cases, the emissions are from the 5d-4f transitions. The broadening in the spectra results from the electrons participating in chemical bonding.

(a)

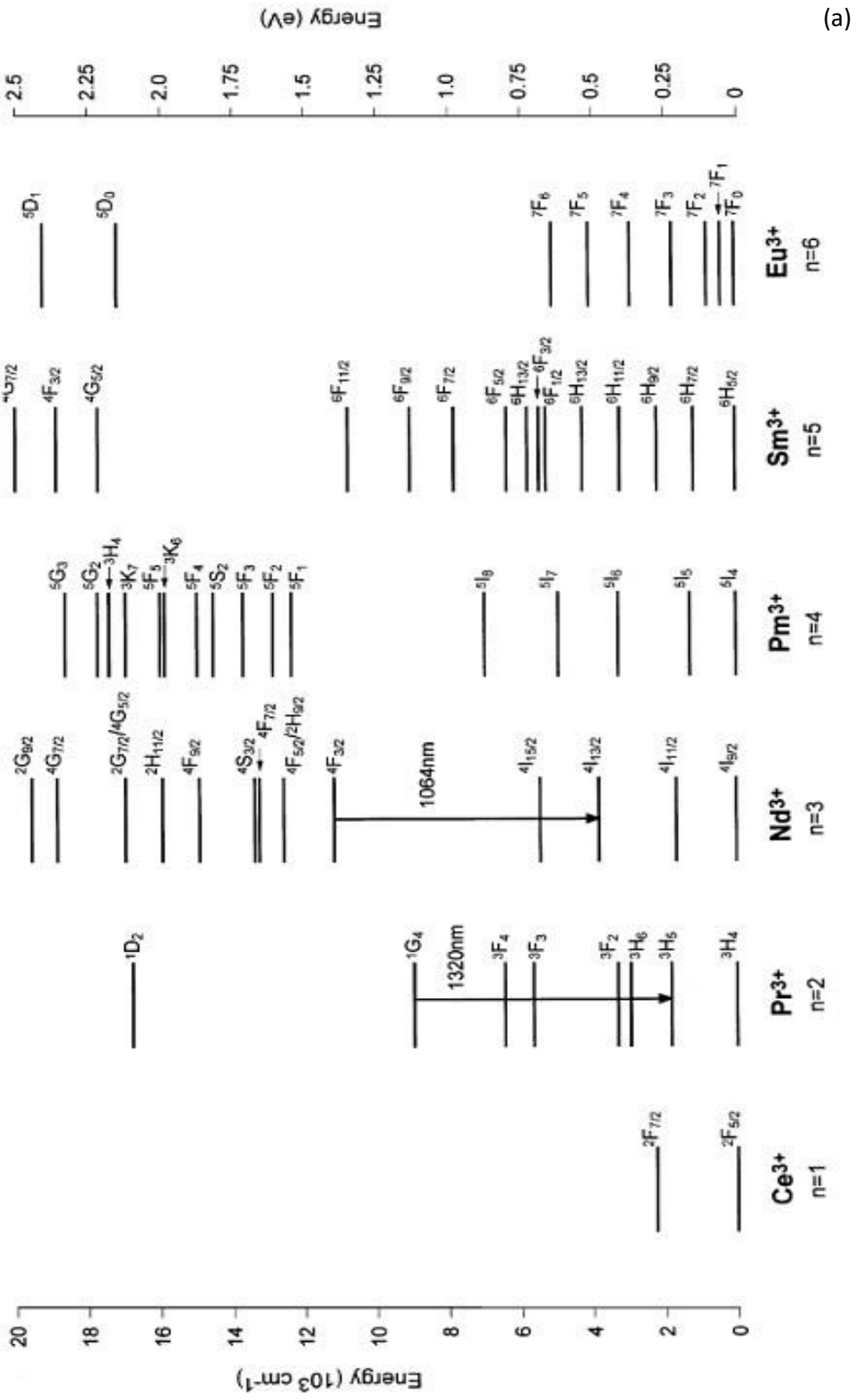
Energy (eV)
2.5
2.25
2.0
1.75
1.5
1.25
1.0
0.75
0.5
0.25
0
Energy (10³ cm⁻¹)
20
18
16
14
12
10
8
6
4
2
0
Ce3+ n=1
Pr3+ n=2
Nd3+ n=3
Pm3+ n=4
Sm3+ n=5
Eu3+ n=6
1064nm
1320nm

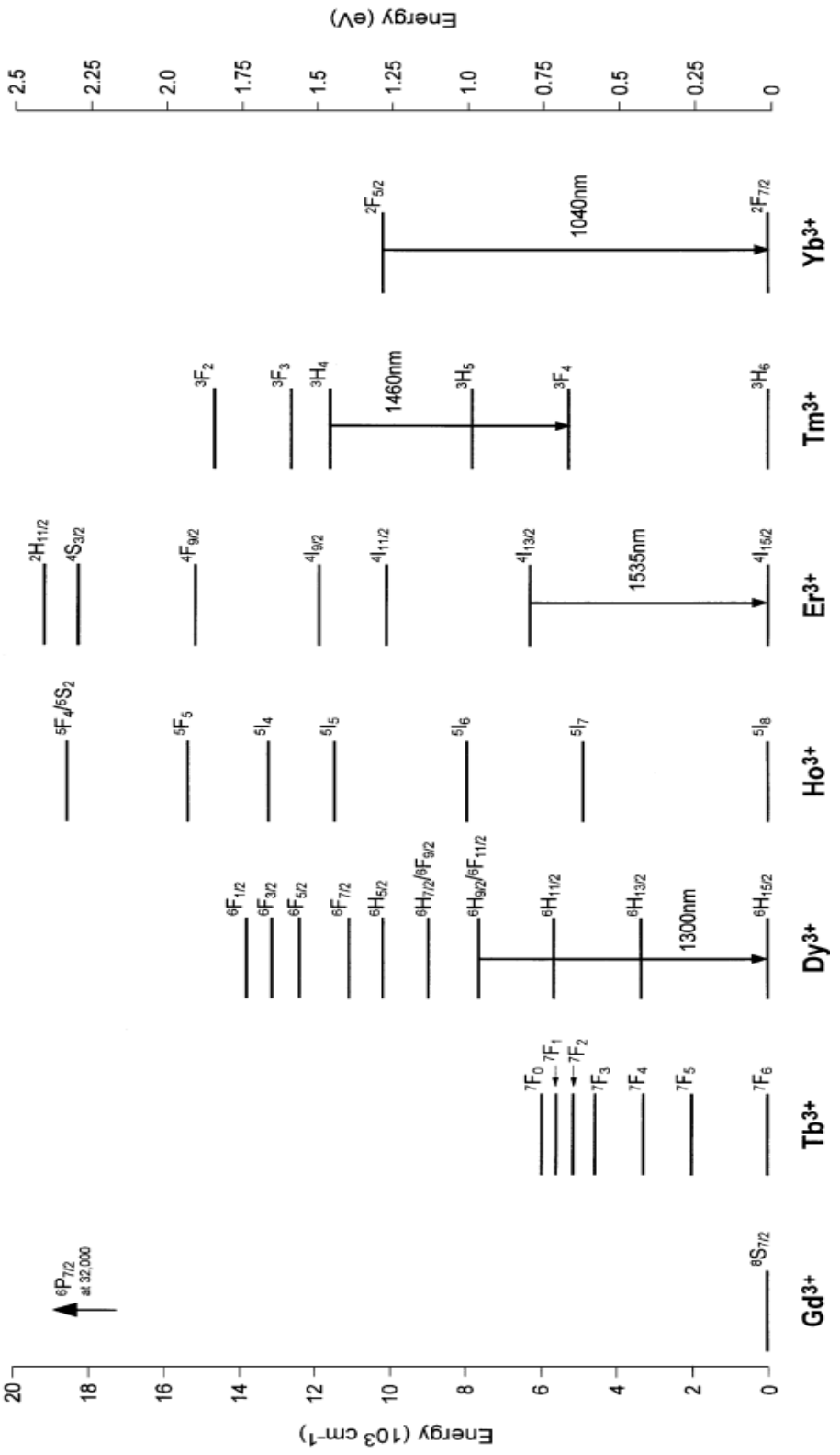

Figure 2. 1: (a) and (b) Electronic structure of some of the rare-earth elements [3]

The emission in erbium (Er3+) around 1550 nm, which falls in the telecommunication window, coincides with the intra-4f $^4I_{13/2} \rightarrow {}^4I_{15/2}$ transition as shown in Figure 2.1. This transition line allowed the transmission and amplification of signals in the 1530-1560 nm region without the necessity for expensive optical to electrical conversion [56]. Few other RE^{3+} elements that are suitable candidates for optical amplifiers are Tm^{3+}, Pr^{3+}, Nd^{3+}, and Dy^{3+}. The Er^{3+} and Tm^{3+} ions are the choice for the 1400–1600 nm window centered at 1550 nm, based on the $^4I_{13/2} \rightarrow {}^4I_{15/2}$ transition of Er^{3+} ion and the $^3H_4 \rightarrow {}^3F_4$ transition of Tm^{3+} ion. The $^4F_{3/2} \rightarrow {}^4I_{13/2}$ emission of Nd^{3+} ion, the $^1G_4 \rightarrow {}^3H_5$ transition of Pr^{3+} ion and the $^6F_{11/2}(^6H_{9/2}) \rightarrow {}^6H_{15/2}$ transition of Dy^{3+} ion are all potentially useful for the 1300 nm telecommunication window.

There are a lot of direct and indirect mechanisms for the existence of a number of excitation pathways in rare-earth elements, namely resonant optical excitation, cathodoluminescence, and electroluminescence in semiconductor hosts being the direct mechanism. Indirect mechanism includes carrier mediated excitation transfer in semiconductors, and dipole–dipole Forster–Dexter coupling in insulators.

2.3 Host materials

The radiative properties of rare-earth elements are highly dependent on the host materials they are doped in [65]. Different materials including semiconductors and insulators have been studied as hosts for these ions. When it comes to semiconductors, silicon has been of particular importance [66], [67] and interest for applications in the integration of microelectronics with photonics [3]. However, the indirect bandgap of silicon has been a deterring factor, limiting such integration. The III-V semiconductor heterostructures are another option for hosts for rare-earth ions and have been extensively studied since its first demonstration in the early 1980s [68], [69]. The use

of gallium nitride as host material is relatively new, but the progress has been quite rapid, especially with erbium doped gallium nitride [70].

Among insulators, silica is the most common host for rare-earth elements, primarily because of its deployment in fibre technology [17]. The development of silica based optical fibres started a revolution in optical communication and has led to the rapid increase in bandwidth capacity. Owing to the development of silica based fibres, ultralow loss transmission of 0.2 dB/km has been made possible. The advent of erbium doped fibre amplifier (EDFA) has enabled long haul communications [48]. EDFA is considered to be a mature technology now and has improved multi-folds over years in terms of low noise figures, linear gain response, and relatively flat gain profiles.

A significant amount of research has also gone into developing the planar analogue of the EDFA in order to integrate them with other optical elements such as splitters and multiplexers in a monolithic design. Breakthrough in this field came with the introduction of ultrafast laser inscription technology to inscribe 3D waveguides within glass and crystal substrates. Waveguides in different rare-earth doped substrates have been demonstrated and the technology is rapidly maturing into a versatile tool for the production of compact laser systems [62].

Besides silica, phosphate glasses also have been utilised because of the several advantages they offer over their silicate and borate counterparts such as high transparency, low melting point, high thermal stability and high gain density [71], [72].

Host materials are as important as the active dopants when it comes to the development of candidates for potential laser applications. The earliest work on samarium was carried out in silica based optical fibres and a laser action was reported at 651 nm [57] but the high concentration doping in silica glass was quite impractical

because of the severe segregation of Sm^{3+} ions. This made the development of compact laser devices quite unrealistic. On the other hand, multicomponent glasses, such as phosphate and fluorophosphates glasses can be doped with high concentration of rare earth ions without concentration quenching. There has been a substantial interest and research in the area of samarium doped crystal growth as well. One of the most recent demonstrations of laser operation in the orange and red spectral range has been reported in Sm^{3+}-doped lithium lutetium tetrafluoride ($LiLuF_4$) and strontium hexaaluminate ($SrAl_{12}O_{19}$) crystals [73]. Glass materials are quite attractive as host materials because of their ability to be cast in large pieces, more homogeneity, and cost reduction. Fluorophosphate glasses have been studied as host materials and they have been reported to shift the IR cut off edge towards longer wavelengths making them highly suitable for fibre amplifiers [74]. The other favourable properties of fluorophosphate glasses are the wide range of transparency (up to$\sim$10μm), no tendency of crystallisation which is critical during optical fibre drawing, low phonon energy (compared to all fluoride glass) ($\sim$1200cm^{-1}), low non-radiative loss due to low multiphonon relaxation, and high rare earth durability. Phosphate glasses were selected for this work as the host material because of their several advantages over conventional silicate and borate glasses due to their unique properties such as high transparency, low melting point, high thermal stability, and high gain density [71], [72].

Based on the previous work and spectroscopic details, the following host glass compositions were identified and fabricated.

Sample name	Composition (mol%)	Total weight of glass (g)	Weight of RE (g)	Density (g/cc)	Concentration (moles/lit)
PKANZSm1.0	$45P_2O_5$ + $15K_2O$ + $10Al_2O_3$ + $14Na_2O$ +$15ZnO$ + $1Sm_2O_3$	10	0.2808	2.8105	0.2262×10^{-3}
PKANZSm2.0	$44.5P_2O_5$ + $15K_2O$ + $10Al_2O_3$ + $13.5Na_2O$ + $15ZnO$ + $2Sm_2O_3$	10	0.5510	2.8731	0.454×10^{-3}
PKSASm1.0	$60.5P_2O_5$ + $14K_2O$ + $13.5SrO$ + $11Al_2O3$ + $1Sm_2O_3$	15	0.3939	2.7370	0.206×10^{-3}
PKSASm2.0	$60P_2O_5$ + $14K_2O$ + $13SrO$ + $11Al_2O_3$ + $2Sm_2O_3$	20	1.032	2.7791	0.411×10^{-3}

Table 2. 1: List of hosts glasses with their compositions for samarium doping

These glasses were prepared by Mr Godugunuru Venkat and Devarajulu Gelija in the research group of Professor C K Jayasankar at Sri Venkateswara University in India using their facilities, and then sent to Heriot Watt University for further experiments. The concentration of the rare-earth ions in mol/lit can be calculated by the relation

$$C\ (mol/lit) = \frac{Density}{Total\ weight\ of\ glass} * \frac{Weight\ of\ RE}{Mol\ weight\ of\ RE} * 1000\ mol/lit$$

Where, mol weight of Sm_2O_3 = 348.72 g/mol

One of the disadvantages of phosphate glasses is their hygroscopic nature. Addition of Al_2O_3 improves the Al^{3+} ions which act as an ionic cross-linker between different chains, inhibiting hydration reactions and improving chemical durability. By addition of alkali or alkaline earth metal cation of smaller field strength such as Na, K or Ba and Mg to a fluoride host, the fluorescence properties of RE^{3+} ion can be enhanced to a considerable extent. Fluoride compounds also help to remove the –OH group from the host glass which cause absorption at around 1400 nm.

All the samples were prepared by the conventional melt-quenching technique at Sri Venkateswara University, Tirupati, India.

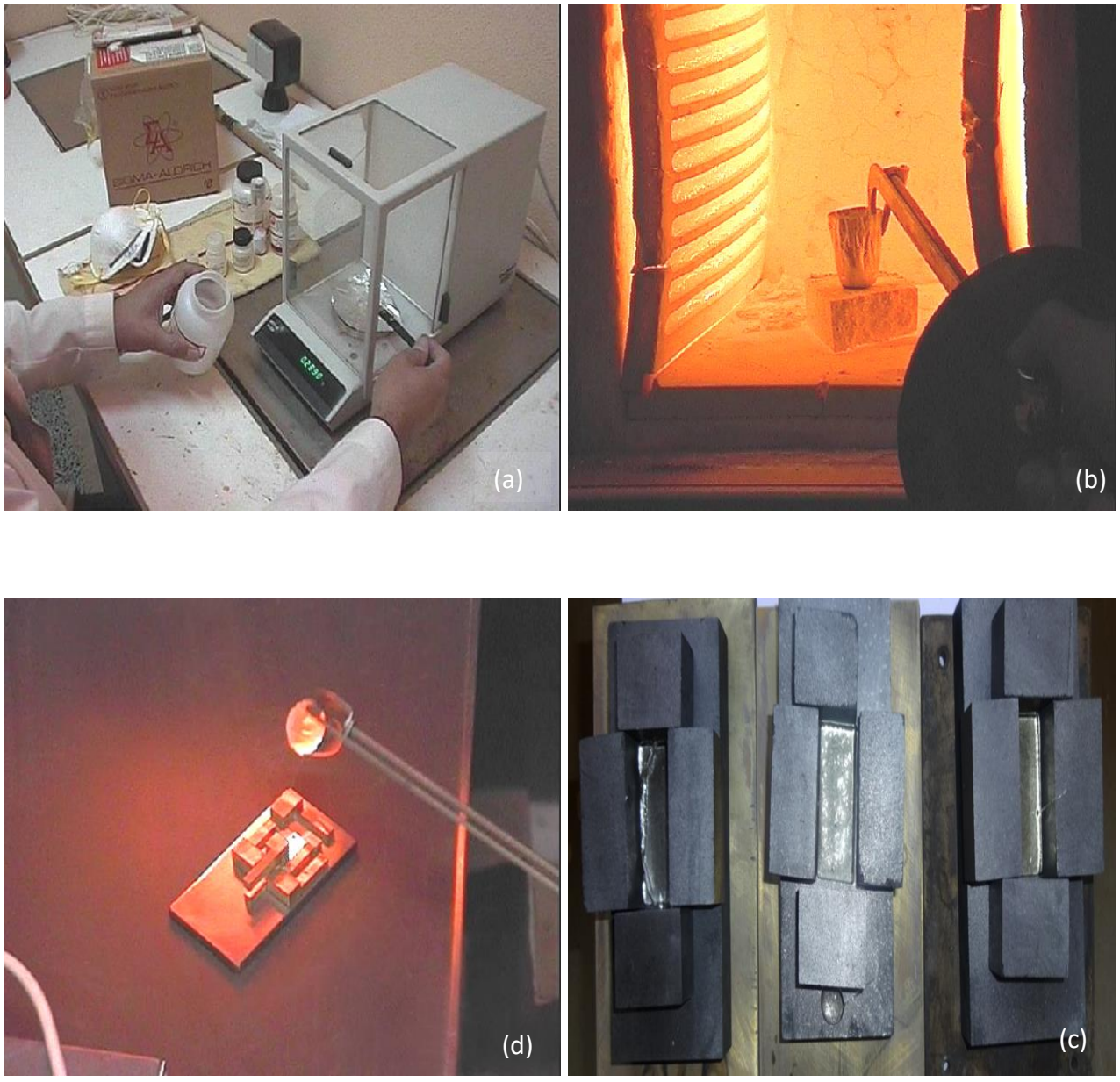

Figure 2. 2: Different steps involved in the preparation of samarium doped phosphate glass including (a) mixing of constituents by accurate measurements, (b) Melting, and (c) & (d) Annealing in graphite and copper crucibles (Picture courtesy: SV University)

Figure 2.2 above shows the different steps involved in the preparation of the samarium doped phosphate glasses. Glass preparation involves the preparation of the appropriate

mixtures of raw materials, a melting and an annealing process. The appropriate amounts of raw materials required for each glass sample were calculated according to the mol % of each component of the glass and weighed to produce the reaction mixture.

Approximately 30 g of raw materials were weighed, well mixed and crushed in an agate mortar and then homogeneous mixture was taken into a platinum crucible and then transferred to melting furnace which was preheated to temperatures between 1200 °C to 1250 °C (melting temperature), depending on glass compositions. The crucible was covered with a platinum lid to avoid excessive loss of materials during the melting process. The melt was then cast onto a casting mould, within an annealing furnace, which had been pre-heated approximately to the glass transition temperature (T_g). Table 2.2 shows the materials that can be used for the casting mould, as the glass does not wet them due to their lower expansion coefficients. The glass was then annealed near its T_g for 2 h and finally cooled to room temperature at a rate of 0.5 °C/min.

Material	**Thermal expansion, α ($\times 10^{-6}$/°C)**
Graphite	~ 3.0
Brass	~ 11.0
Stainless steel	~ 6.5

Table 2.2: Potential materials for casting moulds with their thermal expansion coefficients

The annealing schedule was followed for all the glasses as follows: from casting, the glasses were held at a temperature near their T_g for 2 hours and then slowly cooled to room temperature at a rate of 0.5 °C/min. This was carried out to eliminate the stresses that might be present in the glass. In a homogeneous glass, these stresses may be due to the rapid cooling of the glass through the glass transition region (approximated by

the glass T_g), leaving inadequate time for the constituent atoms to occupy the lowest energy sites. Within the transition region, microstructure changes can occur. These changes require an increasing amount of time to occur as the temperature is reduced. Hence, most glass properties, such as Tg and thermal expansion coefficient (α), depend on time and temperature (thermal history). This means that a change in the heating and cooling rate can induce variations in glass properties. For a glass cooled at a low rate, the glass is able to shrink to a metastable equilibrium volume and becomes dense. However, if the glass undergoes rapid cooling, there is insufficient time for contraction and the glass structure that freezes has a greater volume. Upon heating to the glass transition region, the structure elements of the glass are rearranged into denser and lower energy sites, leading to a reduction of the glass volume. Such structural changes can affect the glass property measurements.

2.4 Fibre fabrication

The history and origin of fibre optics goes back to the year 1840 when physicists Daniel Colodon and Jacques Babinet demonstrated that light could be directed along jets of water. In the year 1884, the Irish physicist John Tyndall showed that light could travel through curved streams of water by setting up a water tank with a water stream coming out of one end. As he shone light into the tank along the outgoing stream, the light followed the water arc down, proving that light could bend along a proper channel. By the end of the 19^{th} century, bent quartz rods could carry light, which was patented to be used for dental illuminations. In the 1920s, John Logie Baird and W. Hansell patented the idea of using arrays of hollow pipes to transmit images for television. The first ever demonstration of image transmission through a fibre optic bundle was carried out by a medical student called Heinrich Lamm in the year 1930, with an aim to probe the inaccessible parts of the body. The next step up in the fibre

optic revolution was the independent reports of imaging fibre optic bundles by Dutch physicist Abrahan van Heel and British physicists H. Hopkins and Narinder Kapany in the year 1954.

The losses in the fibre optic bundles were still quite high to be not suitable for long haul applications. It was in the later 1960s, when a young Shanghai born engineer named Charles K. Kao took the responsibility of studying the properties of bulk glasses and concluded that the high losses in the earlier fibres could be attributed to the impurities present, not to the glass itself. His findings were published in 1966 [75] and caused a worldwide curiosity in trying to decrease the fibre losses. Later in 2009, he was awarded the Nobel Prize in physics for his pioneering work in fibre optics. A few years later, Corning Inc. demonstrated the first single mode fibres operating with a loss less than 20 dB/km. They made cylindrical preforms by depositing purified materials from their vapour phase, rather than trying to purify materials externally. The vapour phase deposition increased the purity of the fibres many fold and laid the seeds of the fibre optic revolution. The primary advantage of this method lies in the fact that during the vapour phase deposition, the impurities, being at a different vapour pressure are left out and only the desired vapours are allowed to be deposited in the tube. The refractive indices of the core and cladding were controlled by adding controlled levels of dopants. Over the years, fibre losses have dropped dramatically, owing to the improved fabrication techniques and shift to the longer operating wavelengths, where the losses are inherently low. The vapour based deposition for the fabrication of fibres laid foundation for the development of ultra-low loss fibres and still forms the basis of modern day fibre fabrication technology.

The first step in the manufacture of modern optical fibres is the fabrication of cylindrical preforms, which is carried out by the chemical vapour deposition method,

also commonly known as the Modified Chemical Vapour Deposition Method (MCVD). The preforms are then processed and fibres are drawn with the help of the fibre pulling towers. In the next following sections, the vapour deposition method to fabricate optical fibre preforms and fibre drawing techniques have been explained in detail. The fibres were fabricated at CSIR-Central Glass and Ceramics Research Institute in Kolkata, India by the research group of Dr Mukul Paul.

2.4.1 Modified Chemical Vapour Deposition (MCVD)

MCVD was developed as a primary technique to fabricate ultra-low loss optical fibres for transmission purposes with pioneering contributions from Corning Inc., Bell Laboratories, and University of Southampton. This method has resulted in fibre propagation losses as low as less than 0.2 dB/km owing to the high purity materials and absence of contamination [76]. There are a few variants of this process, such as, Outside vapour deposition (OVD), vapour phase axial deposition (VAD or AVD), and Plasma chemical vapour deposition (PCVD) and they differ in many respects such as material purity, the degree and precision of refractive index control, mechanical strength of fibres, and the deposition efficiency.

MCVD is carried out through a multistep process which involves a thoroughly cleaned and characterised glass tube mounted on a lathe. Different chemicals in their vapour phase are fed through the inlets into this tube to be deposited along its walls. A uniform heat supplies keeps the chemical reaction going inside the tube to ensure the deposition. The schematic diagram of the MCVD setup is shown in Figure 2.4 and Figure 2.3 below shows the primary steps involved in the MCVD process. The second step after the tube is mounted is the deposition of the cladding and core layers, which is facilitated by the constant supply of the chemical vapour of $SiCl_4$-O_2 along with $POCl_3$-O_2 and/or $GeCl_4$-O_2. Other dopants such as Al_2O_3, Y_2O_3, Re^{3+}, Ag are doped

directly in these layers using the solution doping method, which forms the next step. The rare earth ions are doped in the porous core-cladding structure via this method and it is then sintered and collapsed into a solid rod, which forms the preform. This preform is then mounted on the fibre drawing tower where the fibre is drawn from it. The details of the process is included in the next section.

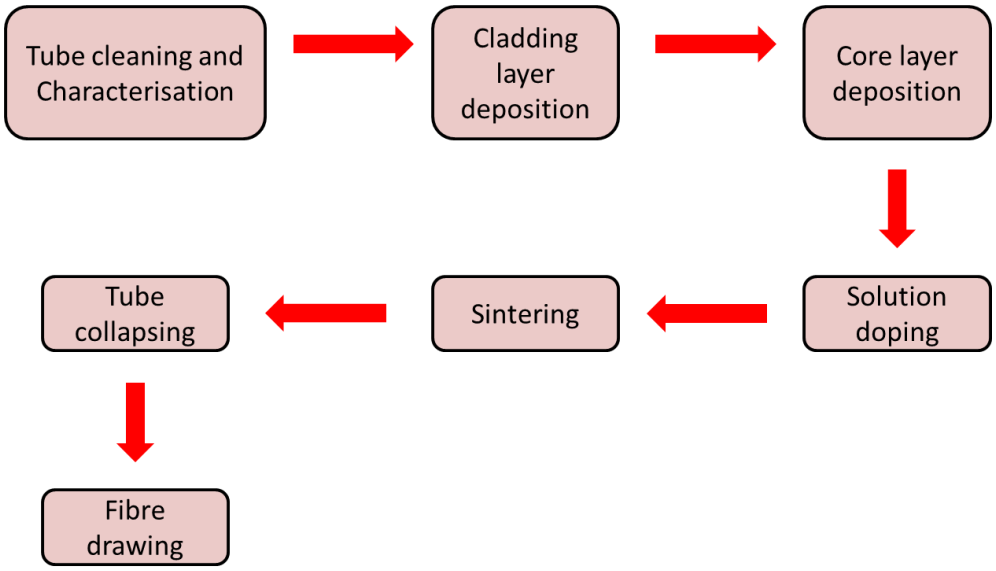

Figure 2. 3: Schematic diagram of the MCVD process

In this process, the chemical reagents are first entered in a gas stream in controlled amounts by passing carrier gas such as oxygen (O_2) through liquid dopant sources such as $SiCl_4$, $GeCl_4$ and $POCl_3$. These liquid halides have sufficiently high vapour pressures at room temperature and are typically used as liquid source for dopant. Figure 2.3 above shows the labelled schematic diagram of a typical MCVD setup.

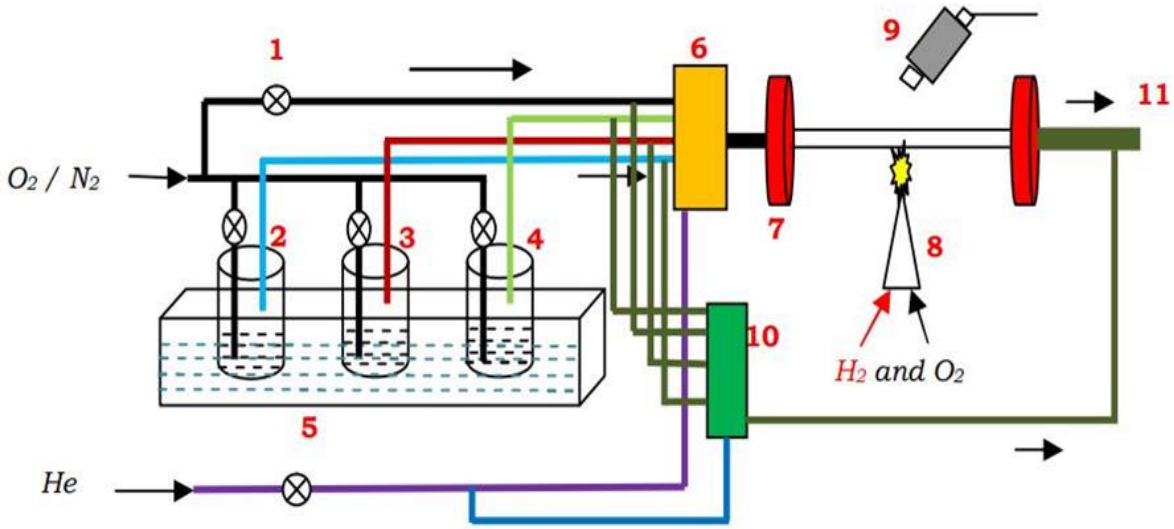

Figure 2. 4: Schematic diagram of the MCVD setup

The chemical reagents are mixed in the desired combination and injected into a high purity rotating silica tube which is heated by a travelling flame torch. Figure 2.3 above shows a schematic diagram of a typical MCVD system which consists of the following parts as labelled:

1. Mass flow controller (MFC)
2. $SiCl_4$ bubbler jar
3. $GeCl_4$ bubbler jar
4. $POCl_3$ bubbler jar
5. Constant temperature liquid bath
6. Vapour mixing manifold or run manifold
7. Tube holding chuck in MCVD lathe along with a loaded silica tub
8. H_2-O_2 gas burner
9. Pyrometer for temperature detection at the reaction zone
10. Vent manifold
11. Scrubber unit

MCVD process is the high temperature oxidation of injected reagents inside the rotating tube which is heated by an external heat source. The vapours in the gas phase react at high temperatures to form soot particles of SiO_2, GeO_2, and P_2O_5 and the following chemical processes take place in the deposition process

$$SiCl_4(g) + O_2(g) = SiO_2(s) + 2Cl_2(g)$$

$$GeCl_4(g) + O_2(g) = GeO_2(s) + 2Cl_2(g)$$

$$4POCl_3(g) + 3O_2(g) = 2P_2O_5(s) + 6Cl_2(g)$$

The generated Cl_2 during soot layer deposition removes residual moisture content from the inner atmosphere of the substrate tube and deposited as a porous soot layer. After soaking the porous substrate tube in RE-chloride solution, the heat from the moving torch fuses the composite soot to form a transparent glassy layer inside the substrate tube. The tube is then collapsed into a solid rod, which is known as the optical preform [77], [78]. The design process of the core and cladding layers is highly controlled and determines the optical parameters of the fibre such as refractive index step, and geometry. The modal behaviour of the fibre, i.e. whether the fibre would be single or multimode also depends on this process. For single mode fibres, usually a single layer of deposition is sufficient, while for multimode fibres, the cladding deposition could be 2-6 layers thick. Most of the communication fibres are single mode at the operating wavelength, whereas fibres used for lasers and amplifiers could be single or multimode. The overcladding process is used to create a specific cut-off wavelength in a single mode wavelength [78]. It also helps to make preforms with larger diameters. The processes involved in MCVD can be summarised as follows:

a. Tube characterisation

The silica tube is first characterised for uniformity in cross sectional area, straightness and concentricity.

b. Tube cleaning

The silica tube is rinsed and cleaned to remove dust and moisture from the inside wall using distilled water and acetone.

c. Tube mounting in MCVD lathe and alignment

The tube is mounted on the lathe and aligned properly with the flame torch. Misalignments of the tube could lead to a temperature gradient throughout the length of the deposition. Figure 2.4 below shows the substrate tube mounted on the lathe and the MCVD control panel.

Figure 2. 5: (a) MCVD lathe with mounted substrate tube and (b) MCVD control panel(Picture has been provided by CSIR:CGCRI, which has been taken during one of their MCVD runs)

d. High temperature flame polishing

The tube is heated at 1800±100° C maintaining an O_2 gas atmosphere inside the tube in order to get rid of any impurities present inside the tube, which could create attenuations in the fibre and are highly undesirable.

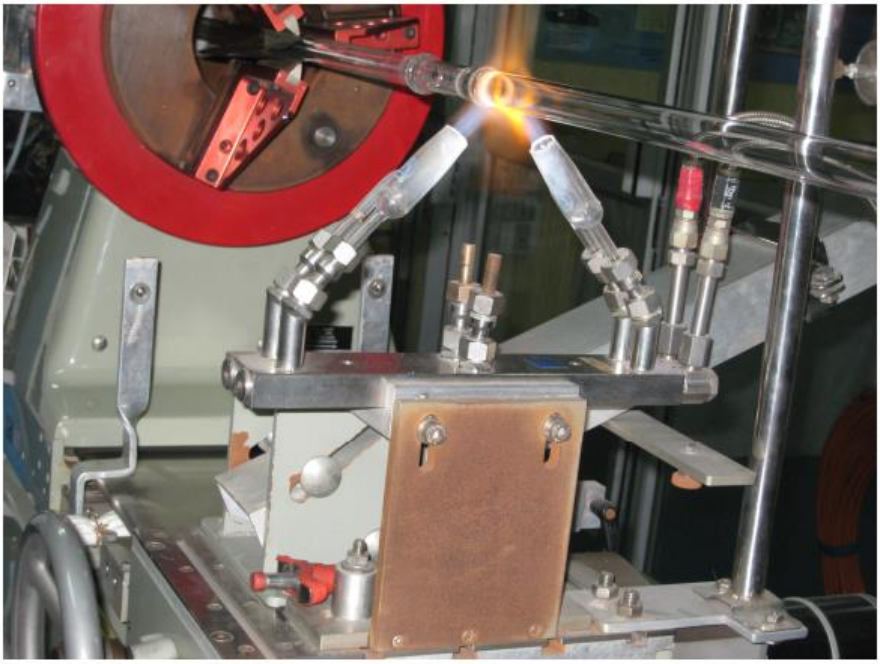

Figure 2. 6: Flame polishing on MCVD lathe during preform fabrication (Picture courtesy: CSIR:CGCRI)

e. Etching of inside surface of the substrate tube

Etching is carried out if necessary for further cleaning at 1850 ± 100 °C using CCl_2F_2, maintaining an O_2-CCl_2F_2-He atmosphere and the process is repeated a few times if required.

f. Cladding layer deposition

The inner cladding layer on the inner wall of the substrate tube is carried out by a chemical vapour of $SiCl_4$-O_2 at a temperature of around 1850 °C. Dry O_2 is bubbled through the $SiCl_4$ bubble jar in a controlled manner in order to produce the $SiCl_4$-O_2 chemical vapour. The $SiCl_4$-O_2 oxidises in the substrate tube and forms fine SiO_2 glass particles which are deposited on its inner walls. The chemical reaction taking place during the cladding layer deposition is

$$SiCl_4(g) + O_2(g) = SiO_2(s) + 2Cl_2(g)$$

g. Core layer deposition

The unsintered core layer is deposited onto the inside wall of the cladding layer. The chemical vapours used for this step are $SiCl_4$-O_2 or $SiCl_4$-O_2 along with $POCl_3$-O_2 and/or $GeCl_4$-O_2. Other dopants such as Al_2O_3, Y_2O_3, Re^{3+}, Ag are doped directly in the these layers using the solution doping method, which is described in details in the later section. The refractive index profile of the core depends upon the layer thicknesses and dopants concentrations. Compounds like GeO_2 and P_2O_5 are employed to increase the refractive index of the core glass. Figure 2.6 below shows the core layer deposition process.

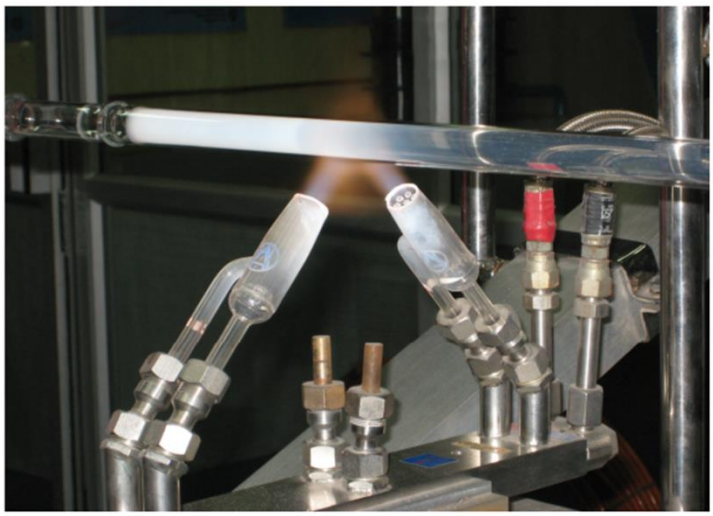

Figure 2. 7: Flame polishing on MCVD lathe during preform fabrication (Picture courtesy: CSIR:CGCRI)

In order to achieve the desired refractive index change in the core, it is critical to have a control of the injection of the reactant vapours. One way of controlling is to monitor the O_2 gas flow rate within the bubble jars placed in the liquid bath during the reaction. This flow creates bubbles in the liquid halides that are kept in the bubble jars. When the bubbles burst, they create a saturated atmosphere of reagent halide vapour within the bubble jar. This reagent vapour is delivered into the tube through the injection line of MCVD setup. A dopant control program is worked out on the basis of

the RI change per mol% of dopants in SiO_2 and the flow of the supplied materials at desired temperature in order to supply a desired amount of reagent.

In order to enable uniformity in thickness and deposition, it is important to have a saturated chemical vapour environment during the delivery of vapour within the tube. Therefore, it is vital to keep the vapour pressure in the bubble jars under constant saturated condition. The only factor that affects the vapour pressure of the bubble jars is temperature. So in order to maintain a constant vapour pressure, the bubble jars are kept in a constant temperature bath.

The chemical processes going on during the core layer deposition can be summarised through the following reactions:

$$SiCl_4(g) + O_2(g) = SiO_2(s) + 2Cl_2(g)$$

$$GeCl_4(g) + O_2(g) = GeO_2(s) + 2Cl_2(g)$$

$$4POCl_3(g) + 3O_2(g) = 2P_2O_5(s) + 6Cl_2(g)$$

As can be seen from the above chemical equations, during this process, the chemical vapours of the ingredients are oxidised to form fine glassy soot particles of SiO_2, GeO_2, and P_2O_5 and are deposited on the inner wall of the tube as the unsintered layer.

h. Solution doping

The vapour pressures of the rare-earth elements are quite low at ambient conditions. Due to this constraint, it is important to introduce a new technique in order to incorporate them into the core. This is where the solution doping technique comes in quite useful. There are a few other techniques utilised for doping as well such as: aerosol delivery, heated chloride source, and vapour transport using organic compounds [79], [77], [78]. Solution doping technique was first introduced in 1987 by [80] and has proved to be quite convenient and efficient over the other techniques. It is

a very controlled way of incorporating compounds like RE^{3+}, Al_2O_3, PbO_2, BaO, and Y_2O_3. in the fibre core. The purpose of doping Al_2O_3 is mostly to increase the refractive index of the core. It has been reported by [79] that one mole of Al_2O_3 increased the refractive index of SiO_2 by 1.81 X 10^{-3} units.

Figure 2.7 below shows the schematic diagram and the actual experimental set up used for solution doping. It essentially consists of a U-shaped tube with an outlet at the bottom.

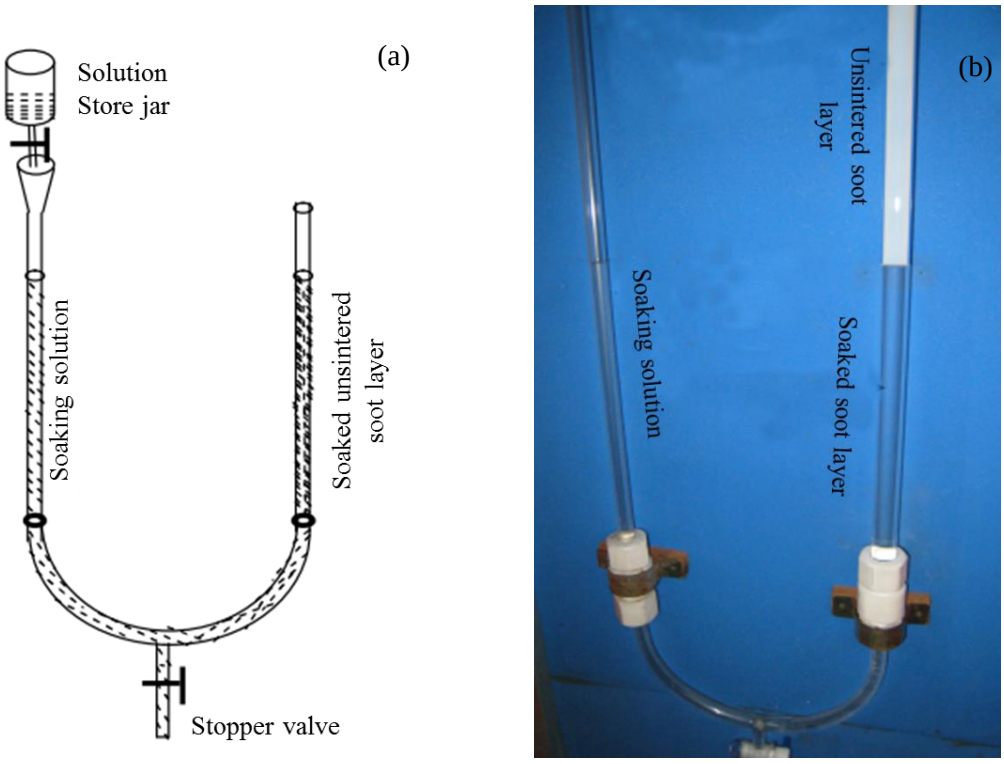

Figure 2. 8: Solution doping technique (a) schematic (b) experimental setup [4]

Solution doping is a multi-step process and the first step involved is the removal of the substrate tube from the MCVD lathe without disturbing the deposited porous layer. The substrate tube is then placed on the right arm of the U-shaped tube. An alcoholic or aqueous solution of the desired dopants is poured into a jar in the left arm of the tube. The solution then drips down slowly and steadily into the tube. The tube is kept

in this position for 45-60 minutes. During this period, the solute ions enter the porous layers and the doping continues until equilibrium in chemical potential is achieved between the solute ions and the porous layers. After the soaking is complete, the solution is released from the tube using the valve at the bottom. After the solution is completely drained from the tube, dry Ar gas is passed through it for about 60 minutes to remove the solvents and dry the porous layer. The tube is then mounted back on the MCVD lathe for further processing.

i. Oxidation and sintering of core layer

The next step involved with preform fabrication is to coalesce the porous core layer into a solid mass by heating in presence of certain chemicals. This process is known as sintering. After the unsintered core layer is drained out of the solvents and dried, it is loaded back onto the MCVD lathe for sintering. In this process, the soaked layer is oxidised using a mixture of oxygen and helium, during which the temperature is slowly raised from 800^{o}C to 1000^{o}C. The ratio of the O_2 to He depends on the kind of chemicals desired through the reaction. In case of Tm-Yb and Er doped preforms, the amount of O_2 is kept much higher than that of He, as in this case, we require the oxides of these doped elements. Following the oxidation, the temperature is further increased slowly from 1200^{o}C to 2000^{o}C keeping the O_2 and He atmosphere constant. After subsequent heat treatment, the porous glass layer transforms into a transparent glass layer. This process involves multiple chemical changes, depending on the dopants, which have been summarised in the equations below:

$$4TmCl_3(s) + 3O_2(g) = 2Tm_2O_3(s) + 6Cl_2(g)$$

$$4YbCl_3(s) + 3O_2(g) = 2Yb_2O_3(s) + 6Cl_2(g)$$

$$Bi(NO_3)_3(s) + Bi_xO_y(s) = NO_2(g) + O_2(g)$$

$$2AgNO_3(s) + 2Ag(s) = 2NO_2(g) + O_2(g)$$

$$4AlCl_3(s) + 3O_2(g) = 2Al2O_3(s) + 6Cl_2(g)$$

$$4Al(NO_3)_3(s) + 2Al2O_3(s) = 12NO_2(g) + 3O_2(g)$$

$$4YCl_3(s) + 3O_2(g) = 2Y2O_3(s) + 6Cl_2(g)$$

$$4Y(NO_3)_3(s) + 2Y_2O_3(s) = 12NO_2(g) + 3O_2(g)$$

j. Tube collapsing

The final step in the preform fabrication is the collapsing of the sintered core layer into a uniform glass rod. Collapsing is carried out at a temperature of above 2000^{o}C. For collapsing, it is necessary that the pressure inside the tube is low. The speed of the burner is decreased stepwise to half of its initial speed. The low gas pressure and high temperature help the tube collapse and a uniform glass rod is obtained. Figure 2.8 below shows the tube collapsing process in progress.

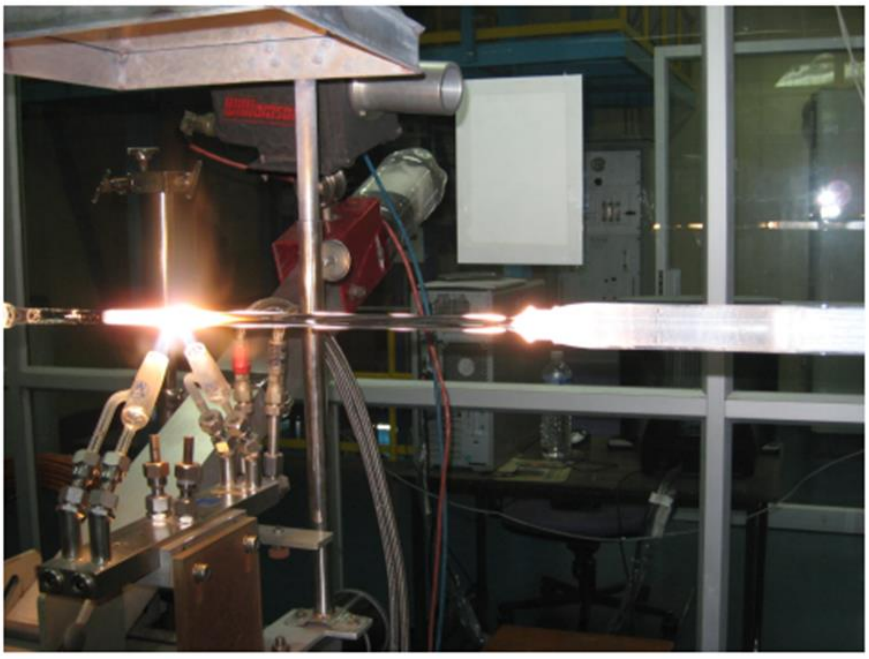

Figure 2. 9: Collapsing process of the sintered core (Picture courtesy: CSIR:CGCRI)

Later, optical fibres are drawn from these preforms on the fibre drawing tower.

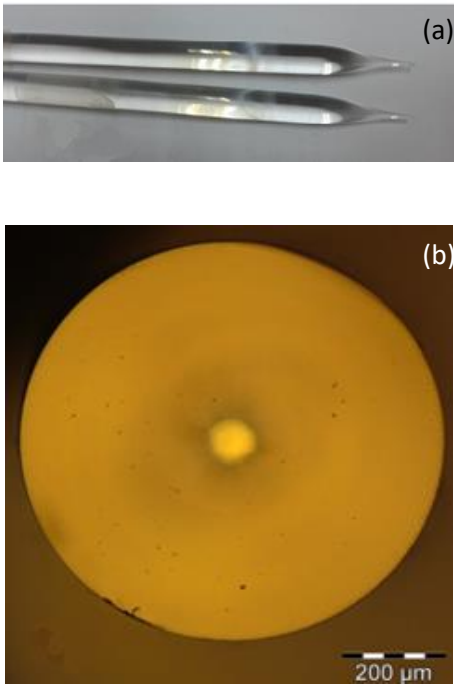

Figure 2. 10: (a) Image of two preforms fabricated and (b) cross section of one Tm-Yb doped optical preforms' tip of ~1 mm [4]

2.4.2 Fabrication of multicore fibre preforms

The basic principle behind the fabrication of multicore preforms is quite similar to that of the conventional single core fibres as described above. It follows the MCVD process, with a few changes in the fabrication method. The multicore fibres fabricated for this project were double cladded. This was done with the aim to cladding pump the fibres for higher power applications. The steps involved in the fabrication of the multicore preform was the preparation of a passive solid preform, followed by its ultrasonic drilling in the desired pattern and then finally insertion of the rare-earth doped preforms in these holes to form a compact multicore preform. The ultrasonic drilling was carried out at the University of Southampton by the research group of Professor Jayanta K Sahu. This composite preform is then taken to the fibre drawing tower for fibre pulling, the details of which are discussed in the next section. The rare-

earth doped preforms were also prepared by MCVD process, followed by solution doping.

The standard GeO_2 preform was also made by MCVD technique and the doping levels of each dopant was monitored by Electron probe micro-analyser (EPMA). An electron probe micro-analyser is a micro-beam instrument used primarily for the *in situ* non-destructive chemical analysis of minute solid samples. It is fundamentally the same as a scanning electron microscope (SEM), with the added capability of chemical analysis. An electron microprobe operates under the principle that if a solid material is bombarded by an accelerated and focused electron beam, the incident electron beam has sufficient energy to liberate both matter and energy from the sample in the form of electrons and x-rays. Of most common interest in the analysis of geological materials are the secondary and back-scattered electrons, which are useful for imaging a surface or obtaining an average composition of the material. Various detectors, including wavelength dispersive spectrometers, arranged around the sample chamber that are used to collect x-rays and electrons emitted from the sample. The EPMA measurements were outsourced to Department of Geosciences, University of Massachusetts. The doping levels of GeO_2 in standard GeO_2 doped preform rod was around 6.0 mol%. The doping level of Er_2O_3 was around 1000 ppm in Erbium doped preform rods. The refractive index profile of each preform rod was measured by preform analyser. The RI profile of standard GeO_2 doped as well as erbium doped preform rods are shown in Figure 2.10 (a) and 2.10 (b) respectively. The RI profile was generated with 630 nm laser light using optical preform analyser of 'Photon Kinetics' (model: PK2600) at CSIR-CGCRI.

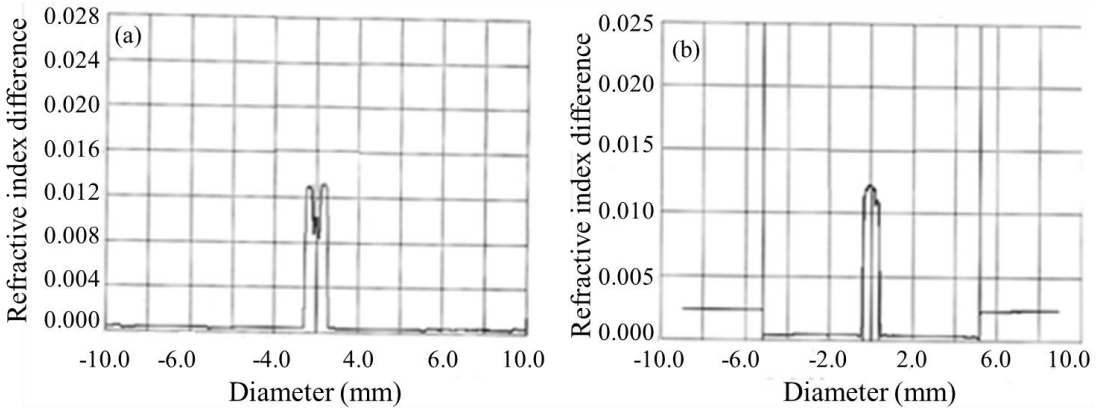

Figure 2. 11: Refractive index profile of (a) standard GeO_2 doped and (b) Erbium doped preform rods [4] measured by the preform analyser

As can be seen from Figure 2.11 (a) and (b), the refractive index plot shows irregularity in the form of unexpected dip in the centre. This could be attributed to the non-uniformity introduced in the centre of the cores while collapsing the tube. This non-uniformity appears to be quite apparent in the preforms, but it does not play a significant role after the fibre is drawn due to a considerable change in its scale. Some length of fibre from each preform rods were initially drawn for preliminary geometrical and optical characterizations. The cross-sectional view of standard GeO_2 doped as well as erbium doped fibres drawn from their respective preform rods are shown in Figure 2.12 (a) and Figure 2.12 (b) respectively

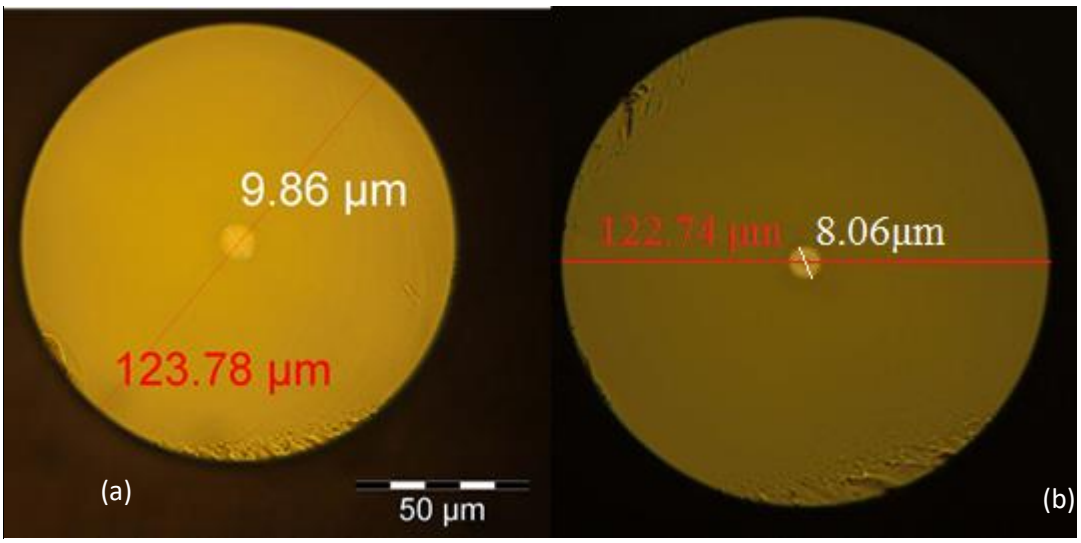

Figure 2. 12: Cross-sectional view of (a) standard GeO_2 doped and (b) Erbium doped fibres drawn from their respective preform rods

After fabrication of preform, etching was done to remove the silica cladding to make the Erbium-doped, Tm-Yb-codoped and Er-Yb-codoped silica glass based rods of having diameter around 3.0 mm using suitable strength of HF solution. The parameters of etching process was optimised for getting uniform etching of silica cladding from each rare-earths doped preform rods. The initial diameter of the GeO_2 doped preform was around 23.0 mm with the NA of around 0.17 and core diameter of 1.15 mm through overcladding process. This 23 mm GeO_2 preform is the outer preform which is to be drilled in order to accommodate for the six rare-earth doped and a central passive core. The deposition of germanium doped silica layer was done within 25/20 mm silica tube, where outer diameter of the tube is 25 mm and inner diameter of the tube is 20 mm, to make the NA around 0.17 which serve as a central un-doped core. The schematic dimensional view of six holes based GeO_2 doped preform rod is shown below in Figure 2.13.

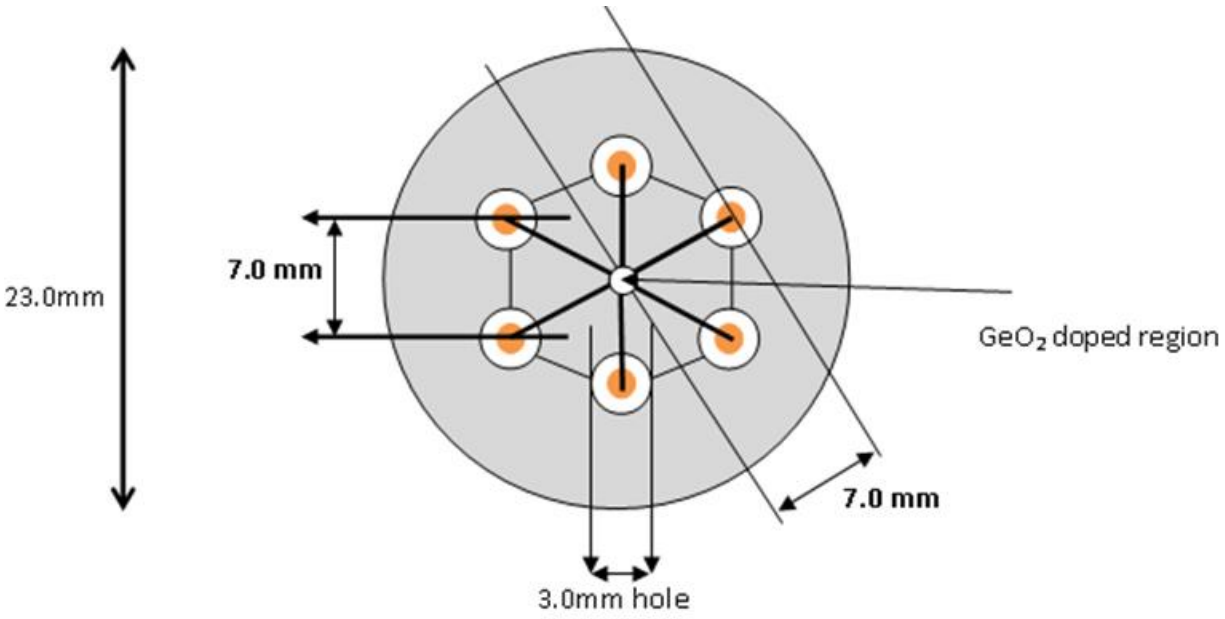

Figure 2. 13: Schematic dimensional view of six holes based GeO_2 doped preform rod

Six holes each around 3.0 mm diameter were created at the vertex of a Hexagon as shown above. The centre of each hole was 7.0 mm distance from the centre of GeO_2 doped region. The distance from centre of one hole to centre of another hole along each arm is around 7.0 mm. The average diameter of the preform rod is around 23.0 mm. The length of GeO_2 doped preform rod is around 23.0 mm. After inserting six erbium doped rods into modified GeO_2 doped preform, the six core based erbium doped optical fibre was drawn with fluorinated low RI resin using the fibre drawing tower. The microscopic view of seven core based erbium doped optical fibre and 5 core erbium-ytterbium doped fibres are shown below in Figure 2.14, with the central cores being the passive GeO_2 doped cores in both cases As mentioned earlier, these fibres were fabricated at CGCRI, and characterised at Heriot Watt University. The images below were taken with a transmission microscope at Heriot Watt. The black spot in Figure 2.14 (b) can be attributed to random defects arising due to improper contact between the drilled holes and the rare-earth doped preforms. If the inner walls of the drilled holes, or the outer surface of the rare-earth doped preforms are not

smooth, it could cause air bubbles to be trapped between them. These air bubbles in the composite preform can manifest as random hollow non-guiding defects in the fibre. These defects were later removed by chemically polishing the holes and the preforms with hydrofluoric acid (HF). The later batches of the MCFs were found to be defect free after the chemical polishing.

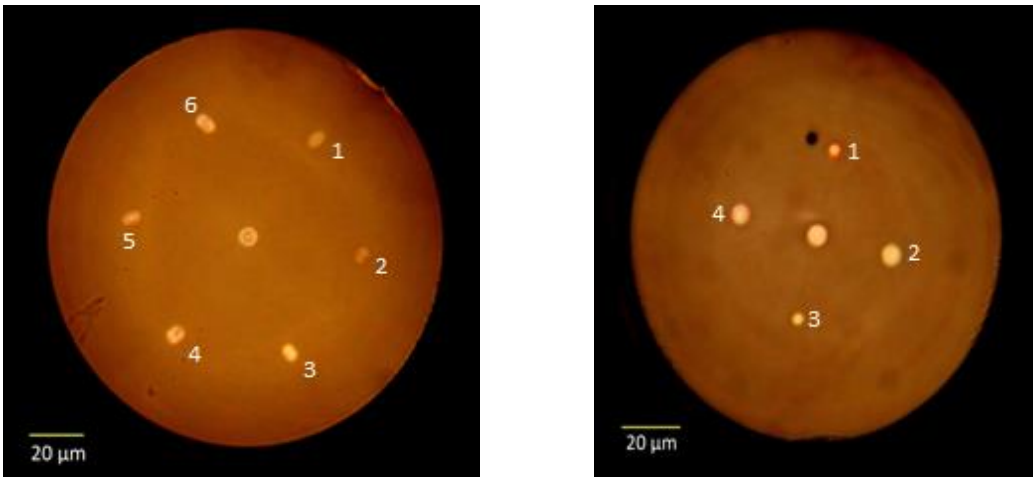

Figure 2. 14: Microscopic view of seven core based erbium doped and five core based Er-Yb fibre

This was the general method followed for the fabrication of further two core fibres as well, which were used in the later stages of the project. Figure 2.15 below shows the schematic diagram for the proposed dual core Yb/Er-Yb fibre and Figure 2.16 shows the microscopic images of the actual dual core fibre drawn from the composite preform.

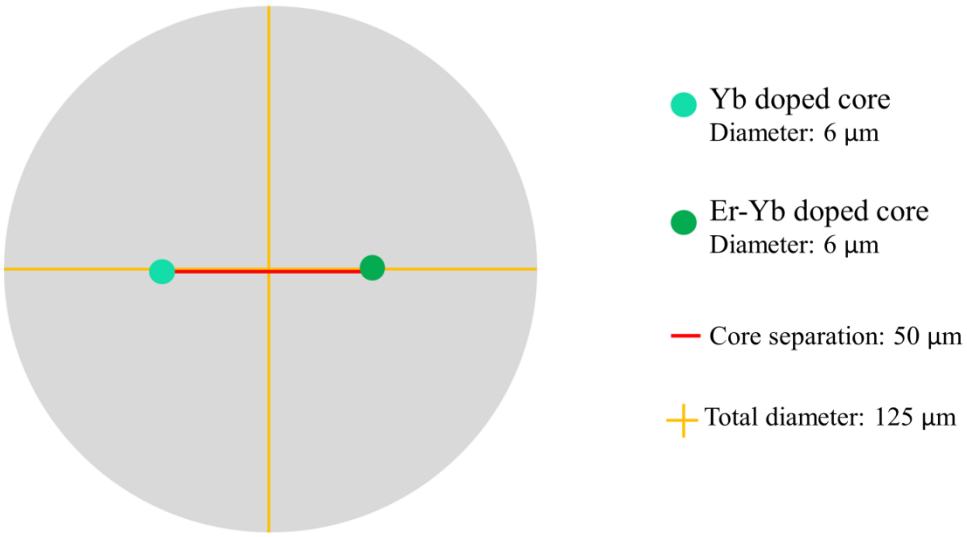

Figure 2. 13: Design specifications of the dual core fibre

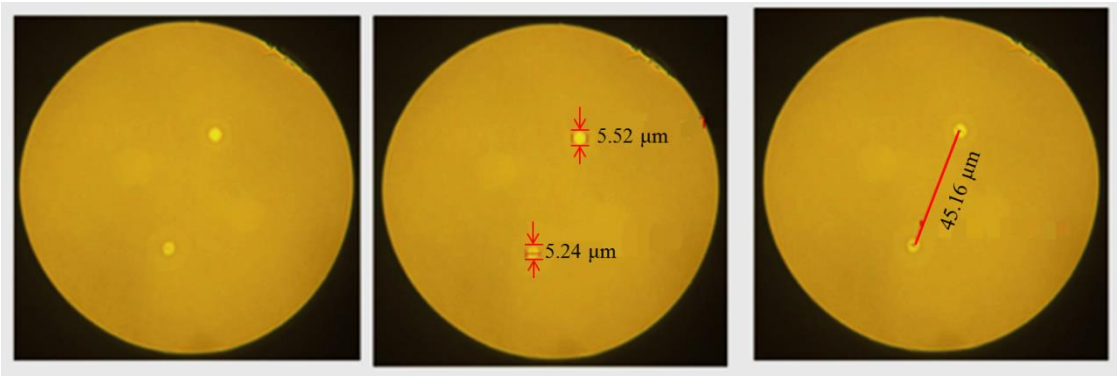

Figure 2. 16: Microscopic images of the cross section of the dual core fibre

2.4.3 Fibre Drawing

Optical fibre production is a multi-step process which starts from the fabrication of a preform, which is carried out by the modified chemical vapour deposition (MCVD) method, the details of which have been discussed in the previous sections. The preform is then taken to a fibre drawing tower which where it is softened in a furnace

and drawn into thin strands of the fibre. The thickness and coating of the fibres can be precisely controlled to suit the requirements.

❖ **Components of a fibre drawing system:**

In order to understand the details of the fibre drawing process, it is essential to understand all the components that make up the fibre drawing system. A fibre drawing system is essentially composed of different elements suited to serve different purposes. The main components are as shown in Fig 2.17 below:

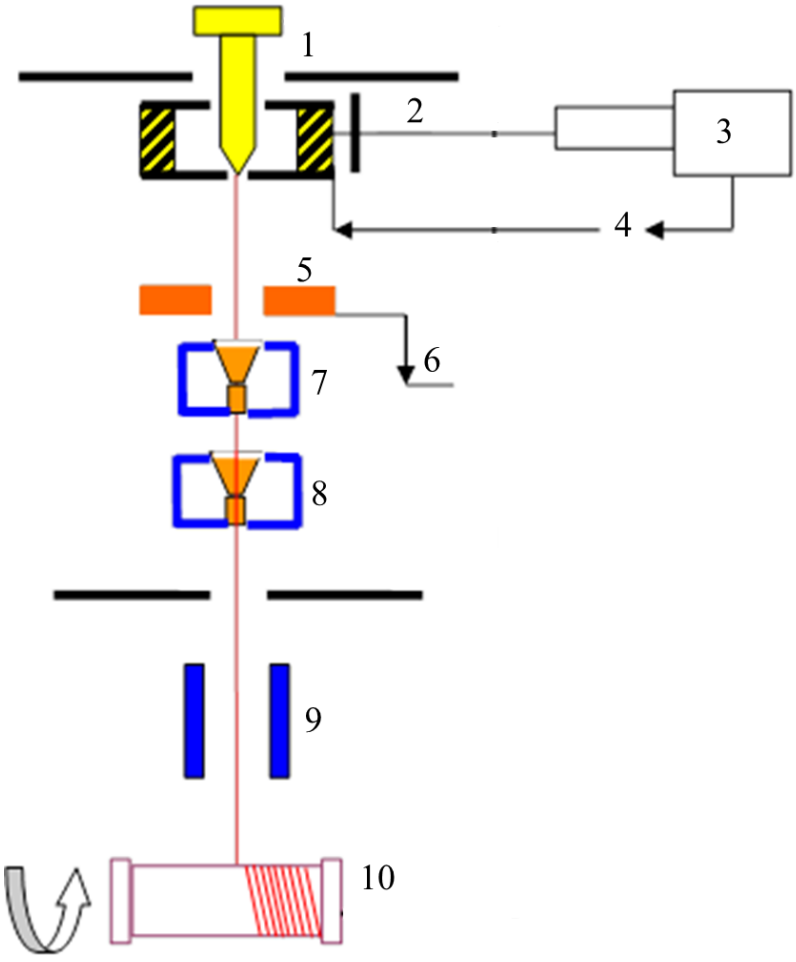

Figure 2. 17: Components of a fibre drawing tower (1. Preform, 2. Heating furnace, 3. Pyrometer, 4. Temperature regulator, 5. Diameter measuring device, 6. Speed regulator, 7. Primary resin coating cup, 8. Secondary resin coating cup, 9. UV curing oven, 10. Drawing and winding machine)

All these components are mounted on a very stable tower the height of which is usually more than 8 metres. Figure 2.18 shows the image of the fibre drawing tower installed at CSIR-CGCRI which was used for fabricating the fibres for this work. The overall fibre drawing tower can be broadly categorised into three zones, based on their functionalities:

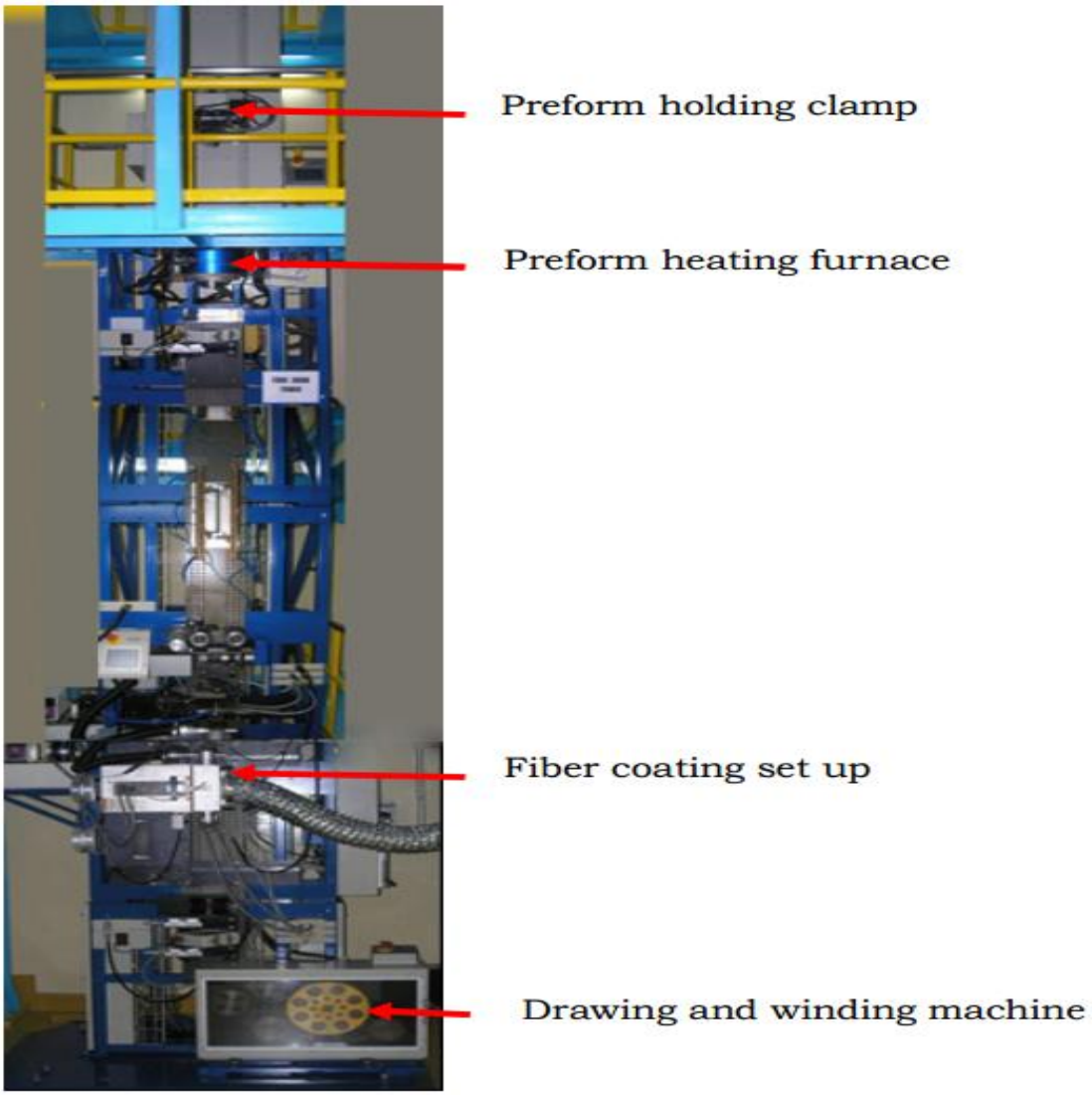

Figure 2. 18: Fibre drawing tower at CGCRI (picture courtesy: CSIR-CGCRI)

a. **Heating zone**: It includes a high temperature furnace with a precision temperature controller. The tip of the preform is lowered into a high-purity graphite furnace. The softening point of silica lies in the range of 1400 to 2350°C. In order to heat the silica

preform to this temperature range, an electrical high temperature furnace is used with an optimal heating zone configuration. A broad temperature distribution along the furnace yields a mild temperature gradient. Once the softening point of the preform tip is reached, gravity takes over and allows a molten gob to "free fall" until it has been stretched into a thin strand.

b. **Cooling zone**: The fibre exiting from the bottom of the furnace by free drawing is cooled rapidly by the surrounding air or by blowing helium gas. An ideal high speed cooling system should be able to provide a sufficient distance between the furnace and the coating applicator. It should also allow a gas blowing device around the fibre to facilitate an effective cooling.

c. **Coating zone**: The application of a thin layer coating on an optical fibre is to provide a protection of its surface and to preserve the pristine state of its strength. Different candidates for coating materials include organic materials like UV curable material such as Epoxy Acrylate and Urethane)., thermally curable material or inorganic coatings such as metallic, silicon nitride, and carbon. The coating used during this project was organic epoxy resin.

2.5 Ultrafast laser inscription

Laser technology has matured enough to enable new pathways to achieve compact and efficient photonic devices. One of the relatively recent developments in the field of ultrafast lasers is their application into fabricating micro-structured photonic components. This technique is known as ultrafast laser inscription (ULI) and has revolutionised the world of photonics. This technology has emerged as a versatile tool for the fabrication of novel photonic components with potential applications in active and passive functionalities. It has given a new and effective approach for creating the

lab on chip components and holds immense promises for the miniaturisation of photonic devices.

The success story of the ULI technique began in the year 1996 when K. M Davis and his research group [59] demonstrated the fabrication of waveguides in silica glass using femtosecond lasers. The phenomenon of femtosecond laser inscribed waveguides in transparent substrates is based on the nonlinear absorption of high energy pulses by the substrate leading to localised energy deposition. This results in a permanent modification in the refractive index of the material which is heavily dependent on the properties of the incident laser radiation and the substrate under study.

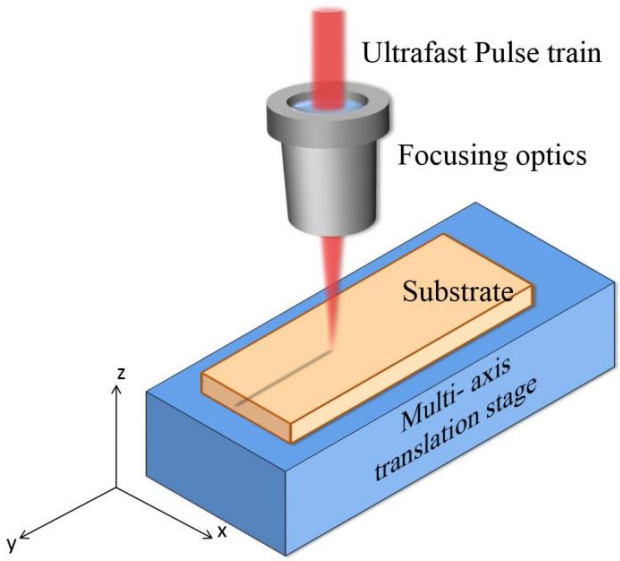

Figure 2. 19: Schematic diagram of the ULI process [5]

The ULI technique has found extensive applications since its first advent, leading to demonstrations of devices in different substrates [62], [81], [82]. The choice of substrate is based on the intended application. For passive devices, where the micro-machined substrate chip is undoped and does not require any external pumping, fused silica is extensively employed [81]. For applications into active devices, where the

substrates are usually doped with ions and are pumped need to be pumped externally, such as lasers and amplifiers, glass hosts allowing higher active ion solubility than silica and borosilicate is preferred. ULI based waveguide lasers and amplifiers have also been demonstrated in laser crystals and ceramics [83], [7].

The permanent modification in the refractive index of the substrate is the result of nonlinear absorption facilitated by the high irradiance of the ultrashort laser pulses. There are mainly two ways in which the nonlinear absorption phenomenon can take place, namely nonlinear photo-ionisation and avalanche ionisation [84], [85]. Nonlinear photo-ionisation refers to the direct excitation of electrons from valence band to conduction band by the nonlinear absorption of the laser pulses. It is further classified into two types, namely tunnelling ionisation and multiphoton ionisation, depending on the laser frequency and irradiance. Avalanche ionisation, on the other hand, can be considered to be a sequence of two processes, namely, free-carrier absorption and impact ionisation [86]. The "seed" electron in the conduction band can linearly absorb incident laser photons in a sequential manner and promote itself to even higher energy levels within the conduction band.

The pulse duration of the laser radiation plays a major role in the type of photoionisation occurring in the substrate. Pulses with lower peak irradiances such as picosecond and nanosecond (ns) pulses have less probability for multiphonon and tunnelling ionisation. The probable absorption mechanism with these pulses is avalanche ionisation. The initial seed electron required to feed the avalanche process depends on the presence of impurities in the materials. The impurities present in the substrate introduce real energy levels within the material bandgap allowing linear absorption processes to promote a valence band electron into the conduction band. In the case of fs laser interaction, the high pulse irradiances initiate nonlinear

photoionisation processes to generate free electrons in the material. The energy absorbed by the electron plasma in the material after the laser irradiance is transferred to the lattice by thermal diffusion. The nonlinear absorption occurs at a time scale of its pulse duration in the case of fs laser pulses, which is much shorter than the ps timescale required for thermal diffusion. The material, therefore, remains under a highly non-equilibrium situation where hot dense electrons with temperatures much higher than the surrounding ions are present within a cold lattice. The main energy transfer routes after this laser irradiation follows electron-ion collisions at a ps timescale and recombination of electrons with ions at a ns timescale, finally leading to a thermal equilibrium. Most importantly, these processes are manifested as different types of permanent material modifications in the irradiated volume, as discussed in the next section.

2.5.1 ULI based waveguides

As discussed earlier, the ULI technique is quite a versatile technique to fabricate waveguides in different substrates by inducing material modifications within the material. These waveguides can be 3D by translating the sample in the XYZ direction to give the modification region the shape desired. The inscription conditions such as the laser irradiance, the focussing optics, and the translation speed of the multi-axis stage are optimised and the refractive index variations are obtained at the focus of the inscription laser within the sample. If the modification causes an increment in the refractive index of the substrate and the modified region acts as the core of the waveguide which confines the guided light. Such waveguides are termed as the Type I waveguides [59], [6]. In most single and poly crystalline substrates, where Type I modifications are not an option, optical waveguides are written by inscribing damage lines. The strain fields between the two damage lines confine light and act as a

waveguide in such conditions. Such waveguides are termed as the Type II waveguides and are commonly inscribed in $LiNbO_3$ and YAG materials [83], [7].

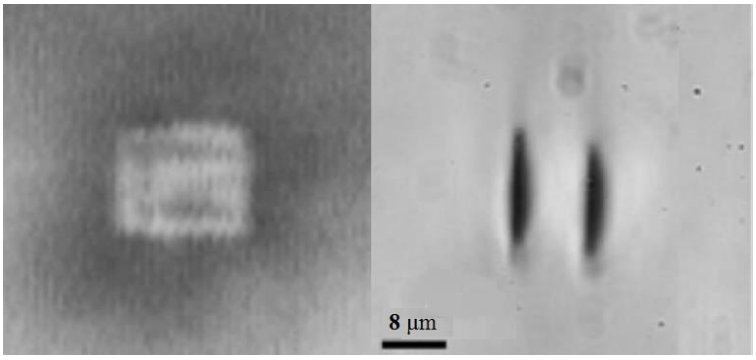

Figure 2. 20: (a) Type I waveguide [6], (b) Type II waveguide [7]

Figure 2.20 above shows type I and II waveguides inscribed in different substrates. Figure (a) is the type I waveguide, where a positive change of refractive index is introduced and the modified region acts as the guiding medium. Type 1 waveguides are usually not a problem for passive waveguides, but since the guidance occurs in the modified region, the radiative properties of the active waveguides might be slightly altered because of the change. Figure (b) shows the kind of waveguides where two damage lines of lower refractive index modification are inscribed parallel to each other and the guidance occurs because of optical strain in between. In materials that exhibit a negative change in the refractive index, few other novel fabrication techniques are used, such as depressed cladding structure [87] and double cladding structure [88].

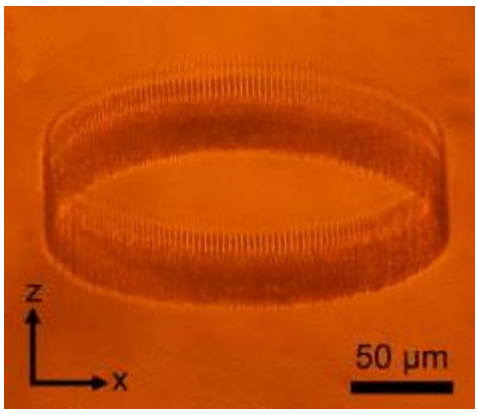

Figure 2. 21: Type II waveguide in ZnSe host [8]

Figure 2.21 above shows a Type II waveguide inscribed in a ZnSe host. The surrounding darkened region is the modified area with a reduced refractive index, whereas the central region is unmodified, which acts as the guiding medium.

The Type I and Type II waveguides are all formed by the combination of a lot of different factors that come into play during the inscription. The properties of these waveguides depend upon a lot of external factors, other than the material properties. Some of the major parameters that play a major role in the waveguide properties are namely:

a. Inscription laser parameters

   The ultrafast laser used for the inscription plays a major role in the waveguide properties. In order to optimise the best waveguide conditions, it is important to vary some of the laser parameters. Some of the laser parameters that can be varied are:

   i. Pulse energy: The pulse energy determines the energy deposited at the focal volume of the laser, and hence a very important parameter.

   ii. Laser pulse repetition rate: It determines the thermal accumulation in the focal volume, thus affecting the cross section of the waveguides.

iii. Polarisation: It plays a major role in crystal substrates, where the laser absorption is related to the alignment of the crystallographic axis with respect to the incident laser polarisation [89].

iv. Pulse duration: It affects the nature of modification and the resulting waveguide properties.

b. Laser focussing optics: It determines the spatial extend of the modified region.

c. Multi-axis translation stage parameters: The speed of translation allows the control over the pulse fluence. The fluence can be increased or decreased by decreasing or increasing the translation stage respectively, hence changing the waveguide properties. Faster translation speeds can reduce heat accumulation.

2.5.2 ULI setup

In order to achieve a controlled and reproducible waveguide inscription, it is important to have a highly stable system in place. The ULI setup used for fabricating waveguides typically consists of a femtosecond laser system, beam steering and controlling optics, beam focussing optics, and a multi-axis, high resolution translation stage.

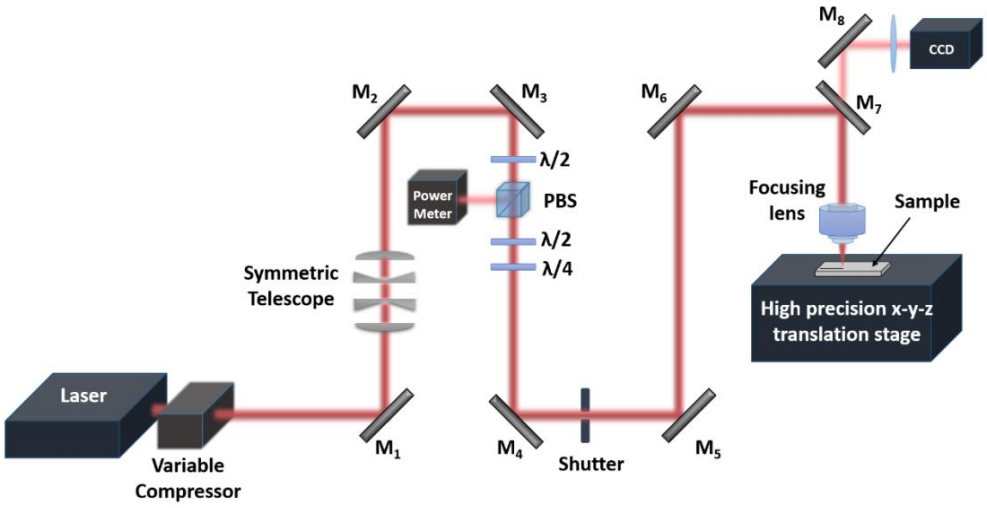

Figure 2. 22: Schematic diagram of the ULI setup [5]

Figure above shows the schematic diagram of the ULI setup used for the experiments carried out for this work. The details of the different components are as below:

i. **Ultrafast laser**: The laser system used for the experiment was a Yb-doped fibre laser, IMRA FCPA μJewel D400. The repetition rate for this laser could be varied from 100 kHz to 5 MHz. An adjustable compressor was used to change the pulse duration by varying the linear chirp on the laser output, with the range varying from 350 fs to 3 ps. The laser emission is at 1047 nm with a linearly polarised output with an average power of ~350 mW.

ii. **Beam controlling optics**: The output beam from the compressor is steered with the help of the mirrors along with other components to control the beam parameters. The polarisation beam splitter in combination with a half wave plate is used for the calibrated attenuation of the beam. A half wave plate and a quarter wave plate are further used to rotate the plane of polarisation and obtain a circularly polarised light. The beam is then steered into the vibration insensitive granite gantry with a beam focussing lens in place. The lens focuses the light into the substrate which is placed onto a multi-axis translation stage.

iii. **Multi-axis translation stage**: The substrate is fixed on a mount over the automated high-precision, air-bearing x-y-z translation stage system, Aerotech ABL1000. It translated the substrate in 3D in order to move the focal point of the laser beam in the desired shape. The translation stage is computer controlled and very stable.

2.6 Summary

The chapter discussed in details the basic techniques and methods used in this work for the fabrication of various rare-earth doped photonic devices. Rare-earth elements have been introduced and some of their opto-electronic properties have been described in the beginning of the chapter. Their relevance in modern day photonic technology has been discussed. The methods used to demonstrate the practical implementations of rare-earth doped elements such as doped glass preparation, specialty fibre optics fabrication, and ultrafast laser inscription has been discussed. Samarium doped phosphate glasses have been prepared via melt-quenching technique for the applications into visible lasers. Samarium has been chosen because of its promising radiative properties in the visible range.

Specialty optical fibres have been designed and fabricated with the aim to demonstrate multiband fibre lasers operating in the near IR range. Traditional MCVD technique has been used in addition to some innovative techniques of drilled preform to form composite multi-rare-earth doped preforms to draw fibres from. Dual core fibres with Er-Yb and Yb doped cores have been successfully fabricated.

ULI technique has been discussed which has been used to fabricate channel waveguides in glass substrates to demonstrate compact ultrafast lasers. ULI technique is instrumental in the miniaturisation of photonic devices making the realisation of monolithic lab on chip devices more feasible. In the current work, Yb doped bismuthate glasses have been used to fabricate buried waveguides in them to realise compact ultrafast lasers operating at 1 micron.

Chapter 3

SAMARIUM FOR VISIBLE SOURCES

3.1 Introduction

Samarium as a chemical element baffled and perplexed the chemists of the 1800s. The discovery of cerium in 1803 initiated the narrative of samarium, as it was suspected of harbouring other metals. Carl Gustaf Mosander, a Swedish chemist, in 1839 claimed to have extracted lanthanum and didymium from it, although his claim of obtaining didymium was proved false later. It was spectroscopically discovered in 1853 by a Swiss chemist named Jean Charles Galissard de Marignac in didymia. Meanwhile, Heinrich Rose, a German chemist carried out his independent studies on a mineral he renamed as 'samarskite', after Colonel Samarsky-Bykhovets, who had provided him with the samples [90]. He concluded that it mostly contained niobium – an element that was initially called columbium. Samarskite soon became the primary source of raw material of choice for extracting new rare-earth elements. In 1879, a French chemist named Lecoq de Boisbaudran isolated a new metal oxide and proposed the name samarium, deriving it from the same root as that of the mineral [91]. Samarium itself yielded other rare earth elements such as gadolinium in 1886 and europium in 1901. With continued research and improved isolation techniques, samarium compounds were obtained in pure form by 1904 [92].

Samarium has been found out to be a fairly reactive element, as it combines with a wide range of elements in relatively mild conditions. Its most common compounds are the oxides, chalcogenides, and the halides. While the most common oxide of samarium is Sm_2O_3, it is also one of the few lanthanides which form a monoxide

SmO. Samarium forms sulphide, selenide, and telluride in the trivalent state, but the divalent chalcogenides such as SmS, SmTe and SmSe are also known.

After its discovery and isolation, samarium has evolved as a versatile element with a wide range of applications. One of the major applications of samarium has been into high-strength magnets. It was particularly important because of its use in samarium-cobalt permanent magnets ($SmCo_5$ and Sm_2Co_{17}) in the 1970s and 80s. After 1985, the samarium based magnets were readily replaced by the neodymium based magnets due to the high raw material costs associated with them. However, due to the resistance to demagnetisation at higher temperatures and corrosion, the former are still critical in aircraft industry and military applications. Owing to their strong absorption of neutrons of a samarium isotope ^{147}Sm, it is also used in nuclear reactors as control rods. It has found applications in the treatment of cancer [93] and pain reliever in the case of cancer spreading to the bone [94].

Other than applications in high-strength magnets and medical science, samarium has also established itself in the field of optics along with other rare-earth elements such as erbium, ytterbium, neodymium and the likes. While erbium, ytterbium, and neodymium have been extensively used for applications into optical sources in the near-IR range [48], [29], [95], a number of elements of this family have been studied and used for applications into the visible region of the spectrum, the major thrust being in lasers, displays and luminescent devices [96], [97]. Samarium has created a niche for itself in the visible emission domain, owing to its seemingly promising radiative properties. Some of the most prominent ions which have been extensively studied for applications into visible luminescence beside samarium are dysprosium, holmium, and praseodymium. Recent work in dysprosium has shown lasing in the yellow region at

583 nm [35]. An extensive study on the possibility of dysprosium as a viable material for white light luminescence has also been reported [20].

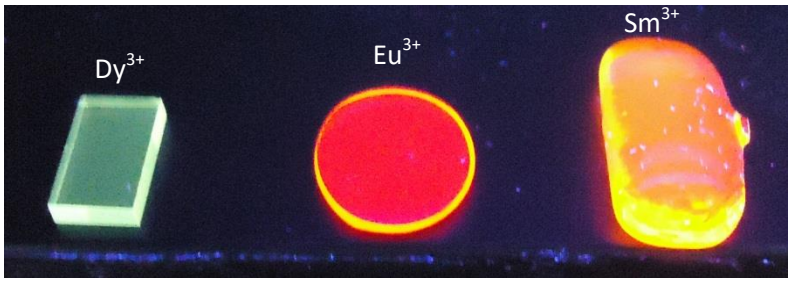

Figure 3. 1: Fluorescence from Dy3+, Eu3+, and Sm3+ doped glasses in the visible range with UV irradiance.

Praseodymium has proved to be quite a versatile material for visible laser applications. Laser operation in praseodymium doped crystals in the green, yellow and red spectral range has recently been reported by [36], [37]. Laser emission in the orange (607 nm) has also been reported by [38] recently. The first visible laser in holmium was reported back in 1965 with a Xe-lamp pumping under cryogenic conditions. Room temperature laser operation was also reported for flash lamp pumped Ho:$YAlO_3$ by Kaminskii et al. [39]. Most of these visible laser reports on these elements have exploited their absorption in the violet-blue range. The success with these elements could be attributed to the availability of GaN based diode lasers operating in the blue range of the spectrum. Figure 3.2 shows the absorption of the rare-earths in the visible range. There has been extensive research on the development of laser sources based on the up-conversion in rare-earth elements as well. It has opened up doors for the realisation of visible lasers with near IR pumping [98], [99], [100]. Figure 3.3 shows the absorption of the rare-earth elements in the near IR spectral region. The IR spectra include the plots up to 2500 nm, as the absorption beyond this range was out of scope of this work.

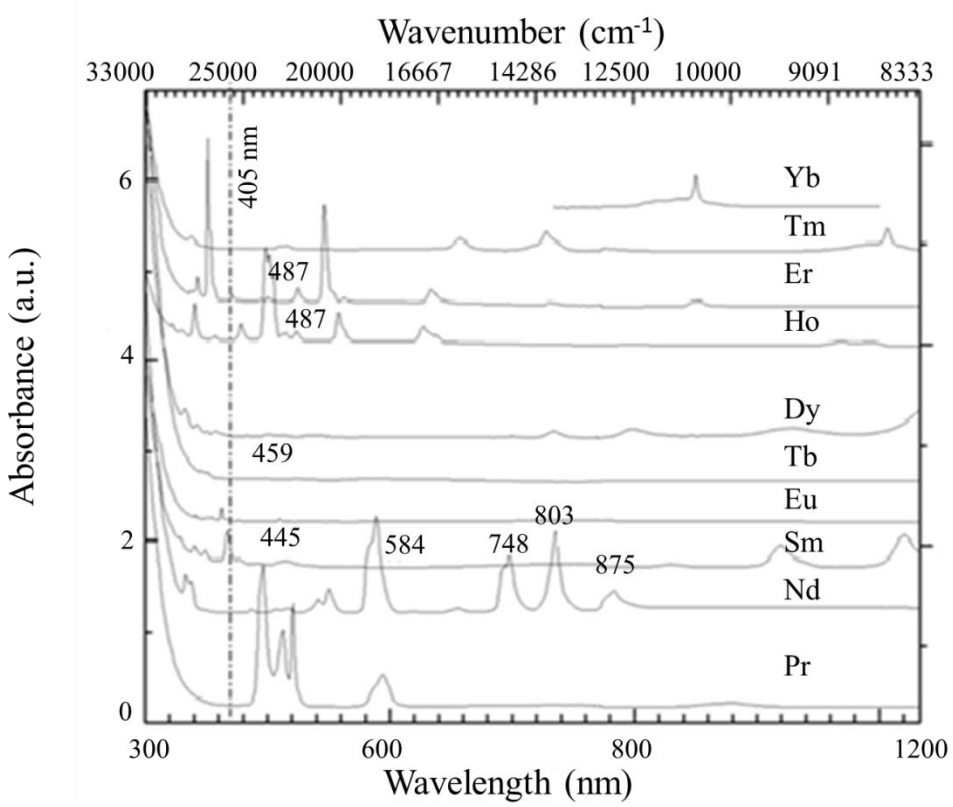

Figure 3.2: UV-NIR absorption spectra of rare earth elements

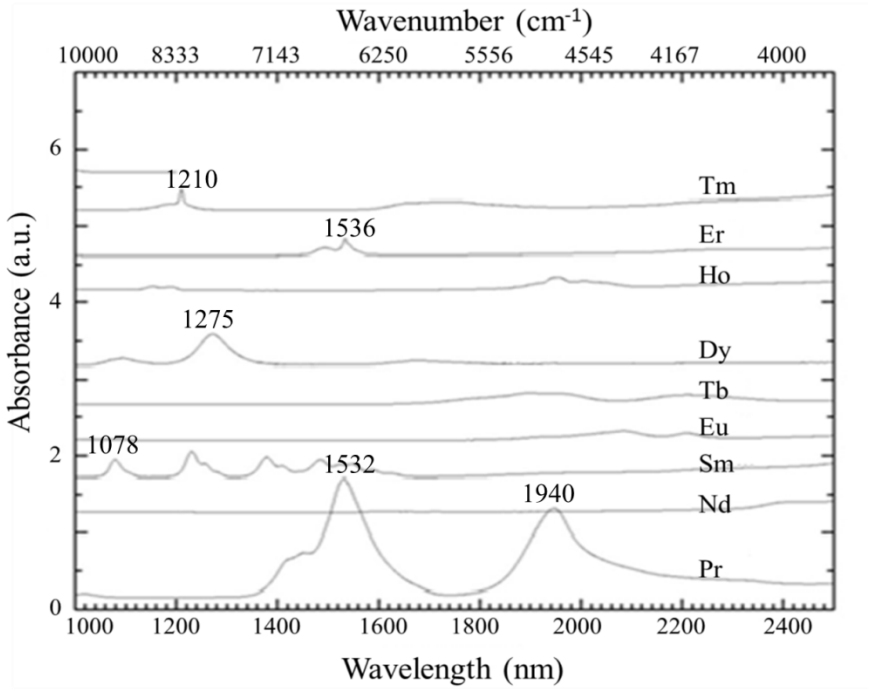

Figure 3.3: IR absorption spectra of rare earth elements

This chapter discusses the viability of samarium as a material for visible laser applications. It includes the experimental work carried out in order to realise a visible laser with samarium ions as the gain medium. It also deals with some of the spectroscopic studies in order to understand the behaviour of these ions with excitation in the violet-blue range.

3.2 Samarium for visible lasers

Samarium has been a promising material for the potential applications into visible lasers operating at multiple wavelengths in the green, yellow and orange range of the spectrum [101], colour displays, solid state lighting, medicine, and spectroscopy. The significant visible emission makes samarium a potential candidate for visible lasers without the need for any nonlinear frequency conversion. Furthermore, visible solid state lasers would facilitate the generation of coherent UV radiation by a rather simple frequency doubling mechanism [102].

Since the first demonstration of lasing action in samarium doped silica glasses operating at 651 nm [57], a lot of interest has been shown in investigating the electronic and optical properties of samarium to optimise a pumping scheme to realise efficient visible lasers. Earlier work on samarium doped bulk glasses have been aimed to identify suitable host materials for achieving laser performance [103], [104], [58], [105], [106], [107]. These works have established that samarium has the highest absorption cross section at 400 nm, but a significantly low emission cross section value could be a deterring factor in realising the lasing action. The relatively larger upper state life time (~ 1 ms) [104] partially compensates for the low emission cross section. Recent work by [101] has used side pumping with 400 nm diode as pump to demonstrate slight line narrowing and amplification in the signal at 600 nm.

3.3 Spectroscopic properties of samarium

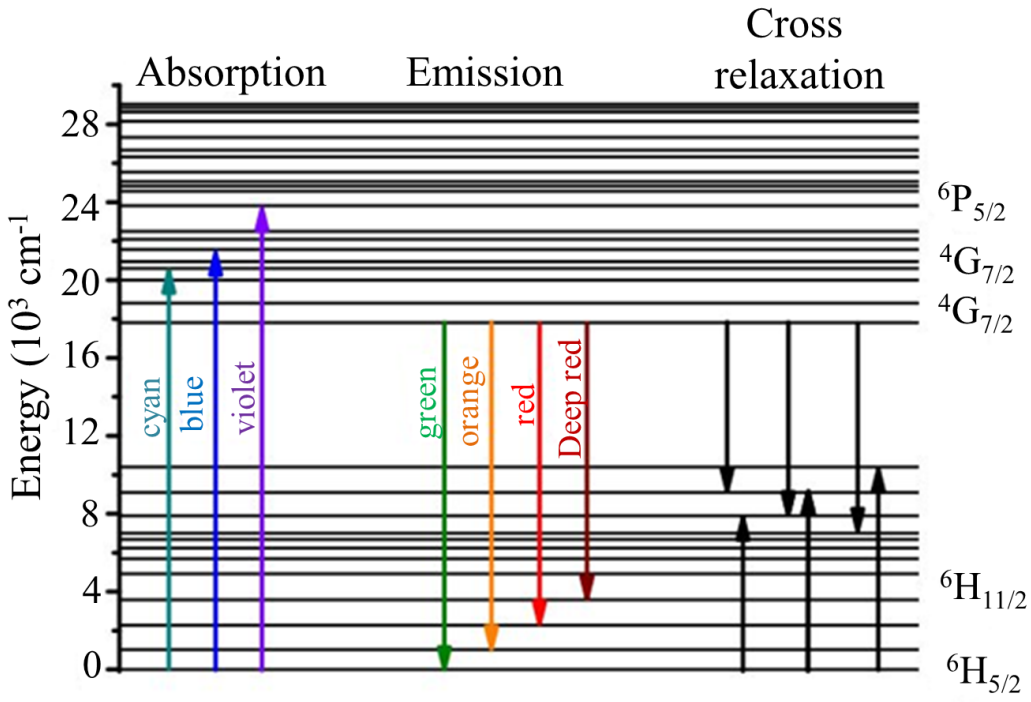

Figure 3.4: Energy level scheme of Sm^{3+} ions [9]

Figure 3.4 shows the energy level diagram of a triply ionised samarium atom. As can be seen from the diagram, it has a large number of closely spaced energy levels which causes different cross relaxation channels. Multi-phonon and cross relaxation processes inhibit the emission of photons which are consequently quite detrimental to laser operation. Phonon relaxations correspond to the collisional decay of an excited energy level, due to the crystalline lattice vibrations or, in other words, to the rapid short range movement of the closely spaced atoms. The excited state is depopulated by the surroundings in the form of phonons. Multi-phonon relaxations between two energy states occur by the simultaneous emission of several phonons that are sufficient to conserve the energy of the transition. Table 3.1 summarise the phonon energies of various hosts. The probability of multi-phonon relaxation may be assessed by using a simple energy gap model [108].

Material	Phonon energy (cm^{-1})
Borate	~ 1400
Phosphate	~ 1100-1200
Silicate	~ 1100
Germanate	~ 900
Tellurite	~ 700
Aluminate	~ 700
Fluorozirconate	~ 500
Sulfide	~ 450

Table 3.1: The maximum phonon energies of various host materials

Cross relaxation leads to fluorescence quenching, i.e. the decrease of fluorescence intensity when the rare-earth concentration is increased. It may occur between ions if they have two pairs of energy levels characterised by the same energy gap. Samarium is stable in both divalent and trivalent state. But it is much more stable in the trivalent state, consequently only a few compounds with Sm^{2+} are known. The luminescence properties of samarium in divalent state are different from the trivalent state. Characteristic Sm^{3+} ($4f^5$) and Sm^{2+} ($4f^6$) transitions can be found in the red part of the visible spectrum (550 – 850 nm). The spectroscopic properties of Sm^{3+} in different host materials have been studied extensively [109], [110], [111]. These works have established that the radiative properties of the samarium dopant depend heavily on the host environment.

The observed emission is due to transitions from the $^4G_{5/2}$ level to the various excited ^6H_J and ^6F_J levels. When Sm^{3+} is excited by blue, violet or ultraviolet light, an intense

orange luminescence is observed. When any of the energy levels above $^4G_{5/2}$ is excited, there is a fast non-radiative relaxation to this emitting level. Consequently, the same luminescence spectrum is obtained regardless of the excitation wavelength (same relative intensities). However, the absolute intensities are dependent on the excitation wavelength. The most intense luminescence is observed by exciting the samples at 400 – 405 nm. This is excitation to the $^6P_{3/2}$ level. The orange luminescence colour is due to the intense $^4G_{5/2} \rightarrow {}^6H_{7/2}$ transition at around 600 nm.

3.4 Experimental details

With the aim to realise multi-wavelength laser operating in the visible range, a wide range of experiments were performed on the samarium ions doped glasses and crystals. The samples were prepared at SV University and the details of glass development have been discussed in the previous chapter. The experiments performed on these samples included absorption and emission studies, laser cavity based experiments, and excited state absorption measurements.

The phosphate glasses produced were tested in order to study the absorption and emission properties. The pump used were 405 nm CW diode lasers and frequency doubled pulsed Ti:Sapphire laser operating at 401 nm. Making use of the ultrafast laser inscription facilities available in the Nonlinear Optics Group at Heriot-Watt University, depressed cladding waveguides were inscribed in the glasses in order to test the guidance at the wavelengths of 405 nm and 632 nm, and to conduct the lasing experiments. Later on, the samples were pumped with frequency doubled CW diodes operating at 480 nm at Hamburg University. The excited state absorption measurements were also carried out. The broadband absorption spectrum of one of the samples (Sm-PKBA; $60.5P_2O_5$-13.5BaO-$14K_2O$-$11Al_2O_3$-$1.0Sm_2O_3$) was measured with Perkin Elmer lambda 950 UV-VIS-NIR spectrometer and is shown in the Figure

3.5 below. The thickness of the sample used for the absorption measurement was 5 mm. As can be seen from the figure, the maximum absorption corresponds to the $^6H_{5/2}$ to the $^6P_{3/2}$ level. The other minor peaks at 415 nm and 440 nm could be attributed to the presence of impurities in the host material. The other major absorption peak was observed to be around 475 nm, corresponding to the transition from $^6H_{5/2}$ to $^4I_{11/2}$ transition. Due to the unavailability of high pump powers at 405 nm, this absorption transition was utilised in the later part of the experiments, when the samarium doped glasses were pumped with a high power diode operating at 479 nm. The details of the experiment are included in section 3.4.3.

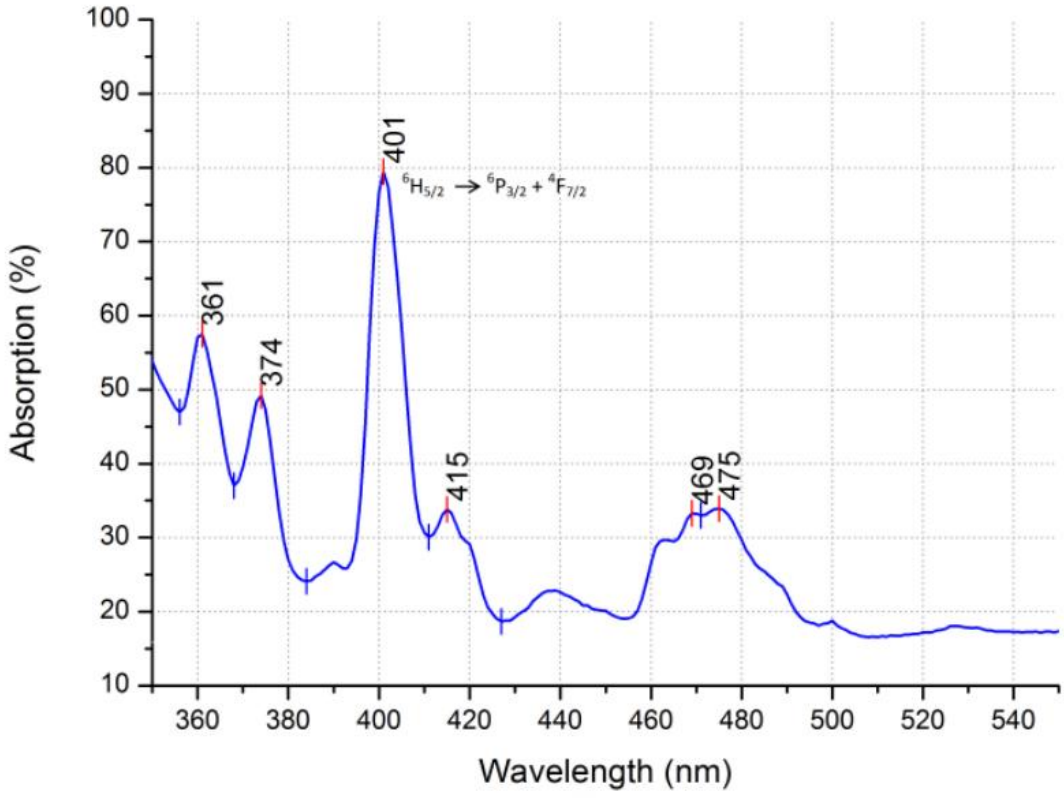

Figure 3.5: Broadband VIS absorption of Sm-PKBA sample

After the absorption measurement was carried out, the glasses were pumped with CW laser diodes operating at 405 nm. The details of the experiment are in the following section.

3.4.1 Pumping at 405 nm

As discussed in the previous section, the maximum absorption in the samarium doped glasses were found out to be centred on 401 nm. With the excitation at around 405 nm, the samarium doped samples exhibit bright reddish-orange emission as shown in Figure 3.8. In order to realise a laser operating in the visible region from this sample, it was pumped at a wavelength around 401 nm. Figure 3.6 below shows the pumping scheme employed with the samarium samples at 405 nm. The samarium doped glasses were simultaneously side pumped with two temperature controlled 405 nm laser diodes and the fluorescence spectrum of the sample was recorded. Cylindrical lenses were used in order to achieve light sheets to ensure the optimum pumped area in the sample. A bright reddish-orange luminescence was observed from the sample under 405 nm excitation. Figure 3.7 shows the emission spectrum for the sample at 405 nm pump. The reddish-orange emission is recorded as sharp peaks at 561 nm, 596 nm, and 643 nm respectively.

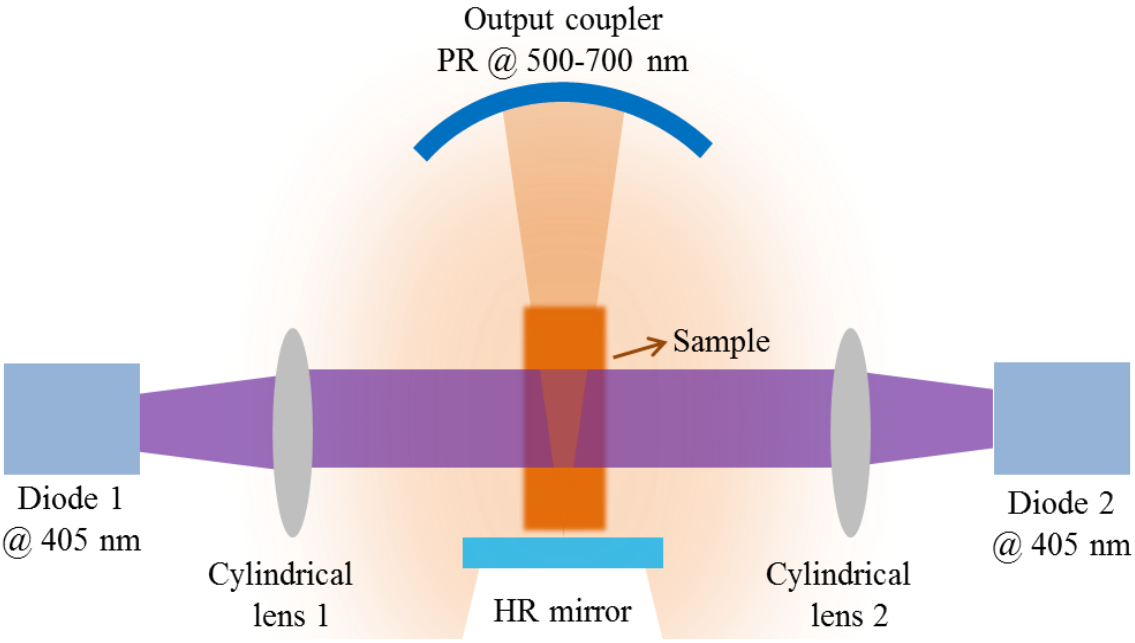

Figure 3.6: Schematic diagram of the side-pumping cavity

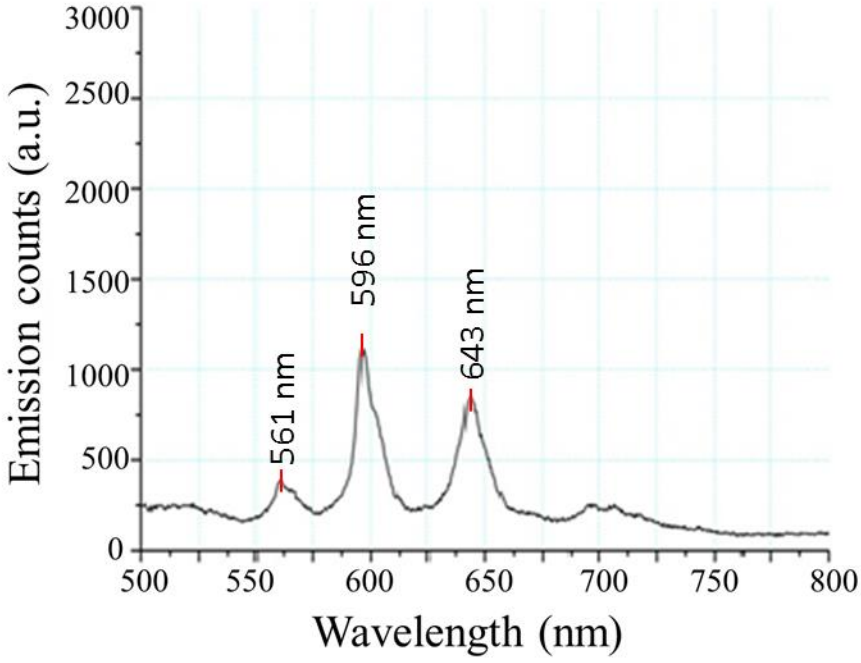

Figure 3.7: Emission spectrum of SM-PKBA sample at 405 nm excitation

Figure 3.7 above shows the emission spectrum of the Sm-PKBA sample with the 405 nm excitation. The figure shows three distinct peaks in the visible range at 561 nm, 596 nm, and 643 nm. The peak in the green is attributed to the transition from the $^4G_{7/2}$ to $^6H_{5/2}$ ground state. The strongest peak lies in the yellow range which corresponds to the $^4G_{5/2} \rightarrow {}^6H_{7/2}$ transition. The transition at 643 nm in the red region occurs due to the transition at $^6H_{9/2}$ level. As can be seen from Figure 3.8 below, the sharp emission lines in the visible range is manifested as a bright orange fluorescence from the samarium doped sample with 405 nm excitation.

Figure 3.8: Bright orange-reddish emission with 405 nm excitation

The sample shows three distinct emission peaks at 561 nm, 596 nm and 643 nm, the emission at 596 nm being the dominant one. The sample was then subjected to side pumping with the 405 nm laser diode with a 10% output coupler and a concave reflecting mirror. Figure 3.9 below shows the emission spectrum of the sample without the output coupler compared to the spectrum with the output coupler.

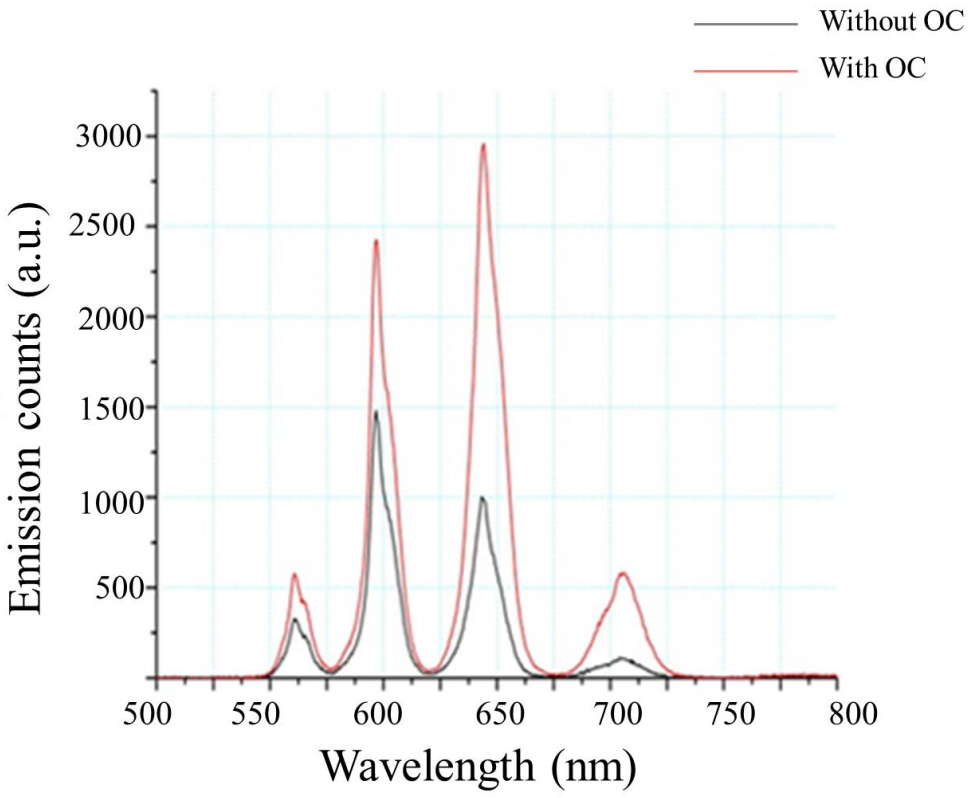

Figure 3.9 Comparison of spectra of Sm-PKBA with and without the output coupler.

The spectrum in Figure 3.9 shows an apparent amplification in the spectrum when subjected to a resonator cavity. As there was no line narrowing observed with the increased signal with the inclusion of the output coupler, it could not be conclusively attributed to an amplification in the signal. The increase in signal could be subject to the alignment of the spectrometer with the incoming beam. The maximum pump power was about 750 mW and no lasing action could be observed with this scheme. Further, some modelling work was carried out using the "Photonics Simulation Software for Teaching (Psst!)" software, made available for free by University of St. Andrews. The software package is a powerful tool for exploring the theory and practice of laser amplifiers, laser oscillators, and different optical cavities for students. It was inferred using this software package, that with higher pump power of the order of around 6W and lower output coupling ratio of < 1%, lasing action could possibly be realised.

3.4.2 Waveguide inscription in glasses

Ultrafast laser inscription has turned out to be a major tool for the fabrication of novel photonic devices. It relies on the permanent modification of refractive index of a transparent substrate material by focussing ultrafast laser pulses on them. Light absorption occurs via nonlinear excitation mechanisms, facilitated by the high irradiances of the focused ultrashort pulses. This is followed by the transfer of the absorbed energy to the surrounding lattice resulting in permanent structural modifications. We have utilised this technique to inscribe waveguides in the samarium doped phosphate glasses. The waveguides inscribed were Type 2 modifications, where the incident irradiance causes a negative change in the refractive index of the material.

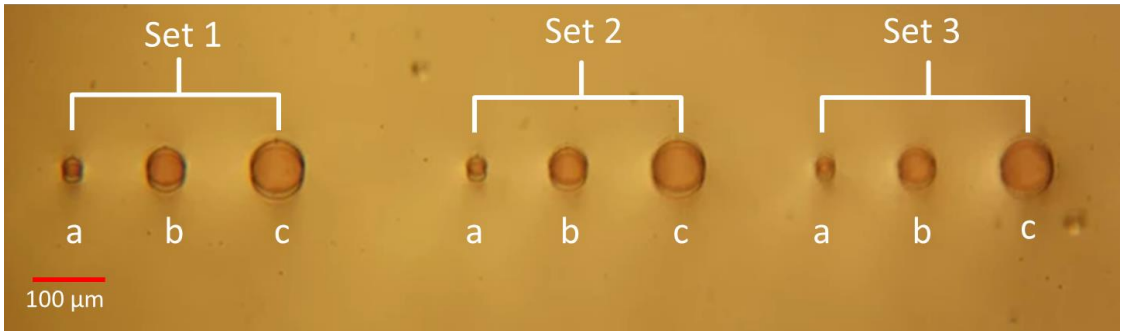

Figure 3.10: Type 2 waveguides inscribed with ULI technique

Figure 3.10 above shows the microscopic image of the cross section of the buried waveguides inscribed with ULI technique in the samarium doped glasses. The waveguides were inscribed in three different sets with different inscription power and sizes. Each set was written with different powers of 160 mW, 180 mW, and 200 mW. The waveguides in each set were of the size of 25 µm, 50 µm, and 70 µm. These sizes were chosen in order to optimise the waveguide sizes for optimum propagation without significant coupling and scattering losses.

The parameters of the waveguides have been summarised in the able below:

	Set 1 (160 mW)		Set 2 (180 mW)		Set 3(200 mW)	
(a) 25 μm	(b) 50 μm	(c) 70 μm	(a) 25 μm	(b) 50 μm	(c) 70 μm	(a) 25 μm	(b) 50 μm	(c) 70 μm

Table 3.2: Summary of ultrafast laser inscribed waveguides in samarium doped phosphate glass

The waveguides were inscribed with the aim to realise waveguide based lasers in the glasses. With better confinement in the waveguides, it was expected that the threshold for lasing could be lowered in the waveguide configuration. Figure 3.11 (a) and (b) show the mode images of the waveguides at 405 nm and 632 nm. The waveguides were found to be multimode at both the wavelengths.

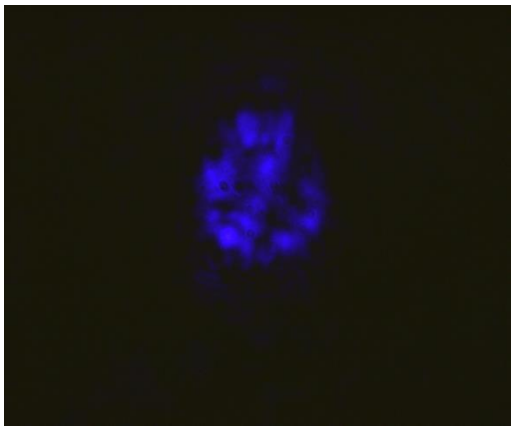

Figure 3.11 (a): Mode image of the waveguide at 405 nm

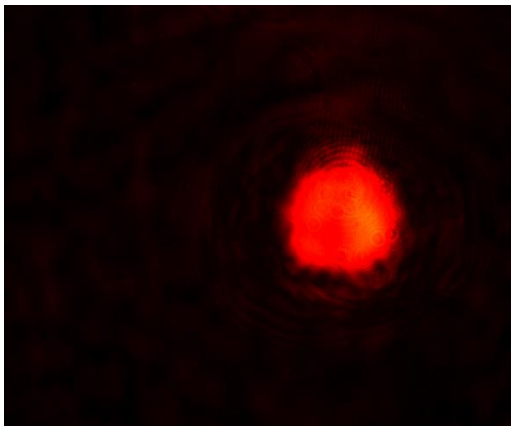

Figure 3.11 (b): Mode image of the waveguide at 632 nm

All the waveguides were found to be multimode at both the wavelengths. In order to achieve single mode propagation, the size of the waveguides were further reduced to around 10 μm, but the scattering losses were found out to be too high for the lights to propagate in the them. The observed scattering losses in the larger waveguides were also found out to be very high, which proved to be detrimental in the realisation of waveguide lasers.

3.4.3 Pumping at 479 nm

As discussed in the earlier sections, the unavailability of a high power pump source at 401 nm makes it difficult to achieve lasing action in the material. In order to realise a visible laser from the sample, it was important to look for alternative pumping scheme. Trivalent samarium ions absorb strongly at around 479 nm, as shown in Figure 3.5. High power laser sources operating at 480 nm are quite readily available in the market, and in the later stage of the work, the samples were pumped with a 479 nm optically pumped solid state laser. All the experiments with the 479 nm pump were performed by me at Hamburg University. The experiments were primarily focussed on pumping the samarium doped phosphate glasses in order to realise a visible laser. The first aim of the experiment was to set up a laser cavity with 479 nm pump diode. The pump source was an optically pumped solid state CW laser diode operating at 478.9 nm with the maximum output of 5W. Later on, spectroscopic studies involving excited state absorption measurements were carried out as well. The details of these experiments are explained in the following sections.

3.4.3 (a) Laser based experiments

Two different cavity configurations, hemispherical and concentric were set up one after another. Figure 3.12 and 3.13 show the schematic diagrams of the experimental setup.

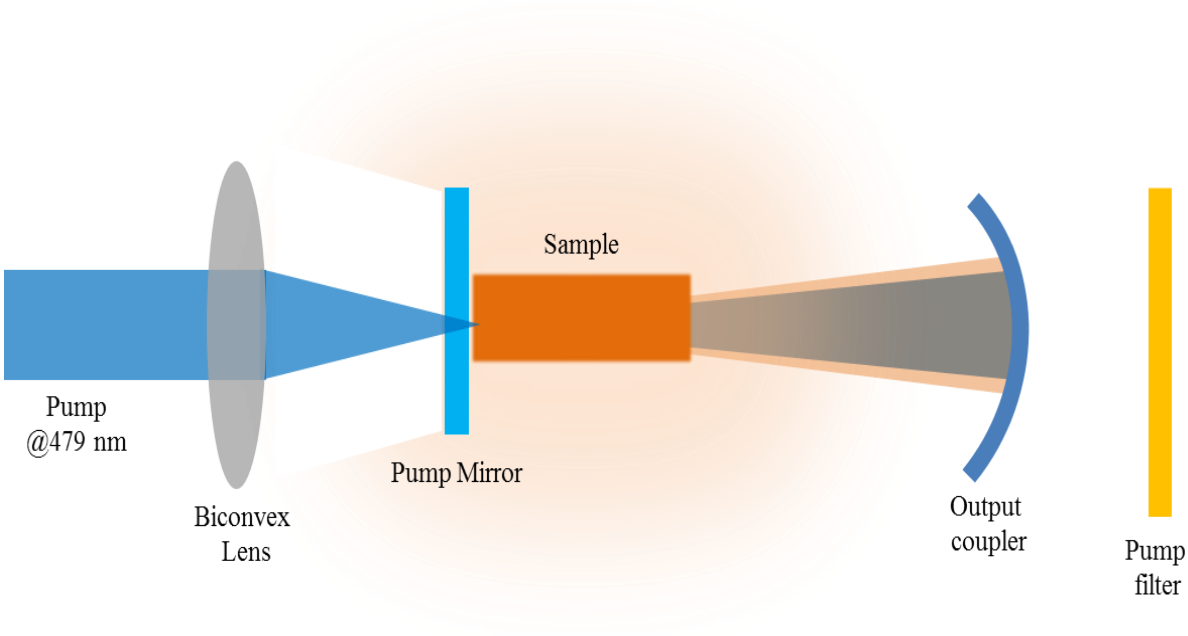

Figure 3.12: Hemispherical laser cavity setup

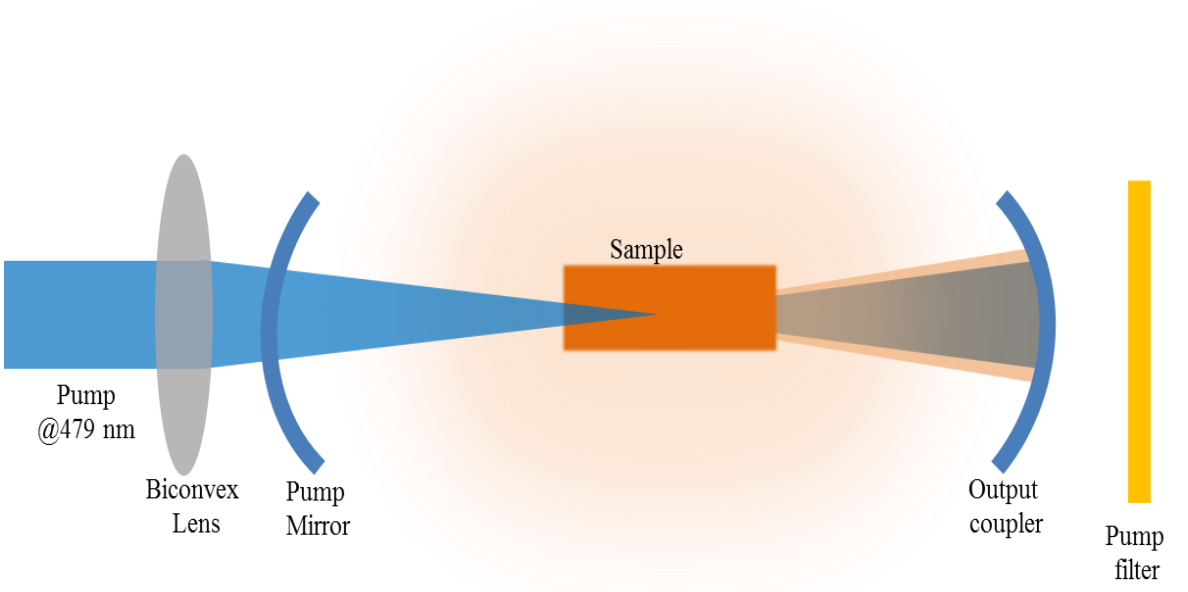

Figure 3.13: Concentric laser cavity setup

The laser setups shown in Figures 3.12 and 3.13 are the hemispherical and concentric resonator cavities designed to realise the laser with the samarium sample. The focal lengths of the lenses, mirrors, and the length of the cavity were determined using the stability condition of laser cavities, which is:

$$0 \leq \ (1 - \frac{L}{R_1})(1 - \frac{L}{R_2}) \leq 1$$

Where L is the length of the cavity, R_1 is the radius of curvature of the pump mirror, and R_2 is the radius of curvature of the output coupler.

The focal length of the focussing lens was chosen to be 100 mm. In the hemispherical cavity, the pump mirror was a flat mirror, transparent at 479 nm and highly reflecting at 596 nm. In case of the concentric cavity, the flat mirror was replaced by a curved mirror with appropriate adjustments in the relative distances between the sample and the mirror using the microblocks the mirrors were mounted on. In both the configurations, a curved output coupler was used. The output couplers used had reflectivities of 99.8% and 99.3%. A pump filter was used to filter out the pump signal going to the spectrometer.

Strong orange fluorescence was observed from the sample even at low pump powers. Pump absorption was measured and the absorption was found out to be around 50% at 479 nm. Output couplers were used for 600 nm, 640 nm and 710 nm. No fluorescence spots were obtained with the hemispherical cavity. However, with the concentric cavity, fluorescence spots were observed without using any collimating optics after the output coupler in the red and deep red region as shown in Figure 3.14 (a) and (b) respectively. However, no laser action was observed up to the maximum pump power of 5W. The sample used in this experiment was the PKBA-Sm phosphate glass, which had femstosecond laser induced damage from the earlier experiments. The frequency

doubled Ti:Saphire femtosecond laser was used to pump the glasses at 401 nm in order to achieve the required high pump energy. No laser operation was achieved with femtosecond laser pumping as well, except it created damaged regions within the sample as shown in Figure 3.15.

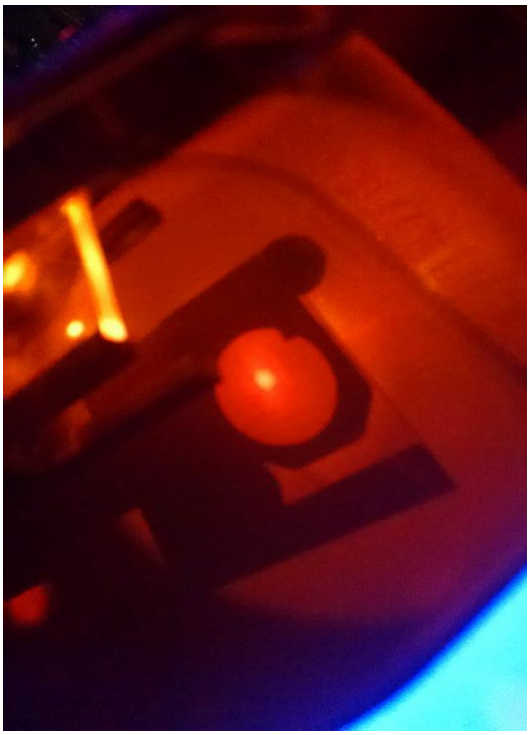

Figure 3.14 (a): Fluorescence spot at 600 nm

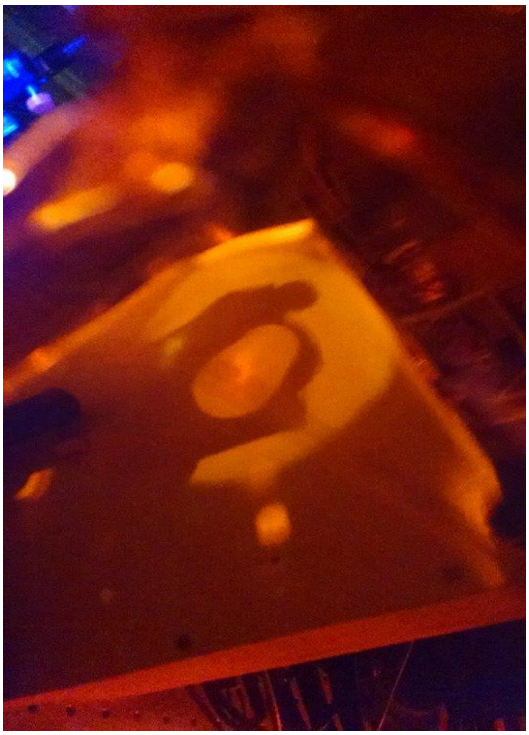

Figure 3.14 (b): Fluorescence spot at 710 nm

Figure 3.15 shows the damage occurred due to the femtosecond laser pumping of the glass. The red region is the damaged area and it could indicate the formation of colour centres in the glass due to the high energy laser pulses. In order to estimate the effect of the damaged region on the optical properties of the glass, absorption experiments were performed on the damaged and undamaged samples. The details of the absorption measurements are explained in the following section.

3.4.3 (b) Absorption Measurements on Samarium Glasses

Broadband absorption measurements were carried out on two of the samples namely PKSA-Sm 1.0 and PKBA-Sm (Table 2.1). The PKBA sample had been used earlier at

Heriot-Watt University and was laser damaged (red spots) by the femto-second laser pumping as shown in Figure 3.15 below. This red damage region could be attributed to the formation of colour centres in the glass with the femtosecond irradiation.

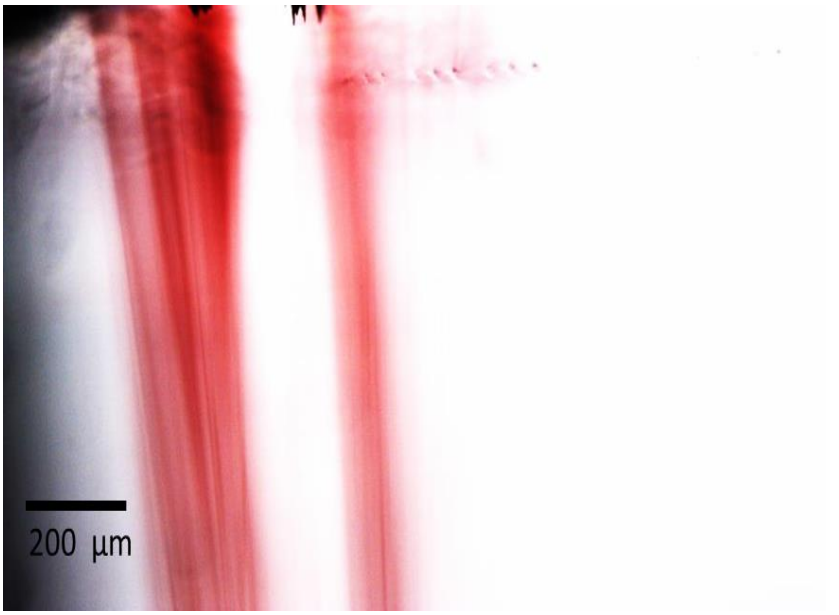

Figure 3.15: Top view of the femto-second laser damaged PKBA sample

The femtosecond pumping of the phosphate glasses was carried out in order to achieve high pump power at 405 nm. The pumping was achieved by frequency doubling an 800 nm Ti:Saphire based regenerative amplifier operating at 1 kHz repetition rate. The irradiation of the phosphate glass with femtosecond beam caused the formation of plasma inside it which led to a cascade of physical processes resulting in the permanent local modifications of the solid state structure. With sufficient energy, the substrate undergoes localized softening and melting and shock waves form during heating, dissipating energy away from the heated volume. The remaining energy is eventually lost through thermal diffusion. Since the heated volume is typically of the order of several μm^3, the subsequent cooling is rapid, of the order of 1 µs or so. Rapid cooling means that structural changes that occur during heating become 'frozen in' which can result in a host of structural modifications including the formation of colour centres. Colour centres are defects within the bond structure of a material. They can

manifest as atoms with incomplete octets (holes), electrons ‘stuck’ in excited states (excitons), missing atoms (vacancies), impurities (substitutions) or a combination of these. Colour centres are localized points in the material where the bond structure has been altered. The formation of colour centres therefore changes the molar refractivity of a material, independent of density change. In phosphate glasses, with KHz repetition rate irradiances, phosphorous–oxygen hole centres (POHCs) and PO_3- ions form as a result of P–O bonds being broken during the modification process, and the subsequent removal of POHCs give rise to the increased proportion of P-tetrahedra bonded to a single bridging oxygen [112]. This material modification in terms of the bond structure can manifest as a change in the absorption of the damaged region.

For the PKBA sample, light was transmitted through the fs laser damaged red area to see its effect on the absorption. It was observed from the absorption spectrum that the damaged region showed a considerable amount of absorption in the broadband region (500-650 nm), which might be deterring for the lasing action. The PKSA (new sample) did not show any such absorption in that region.

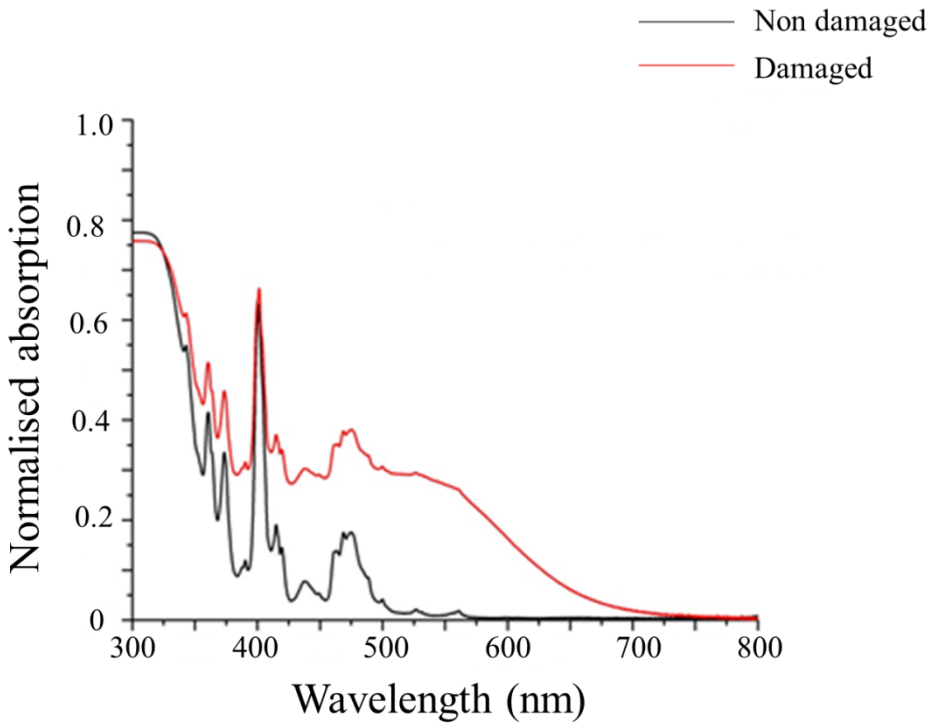

Figure 3.16: Comparison of absorption of the damaged and non-damaged portions of the same sample (PKBA-Sm)

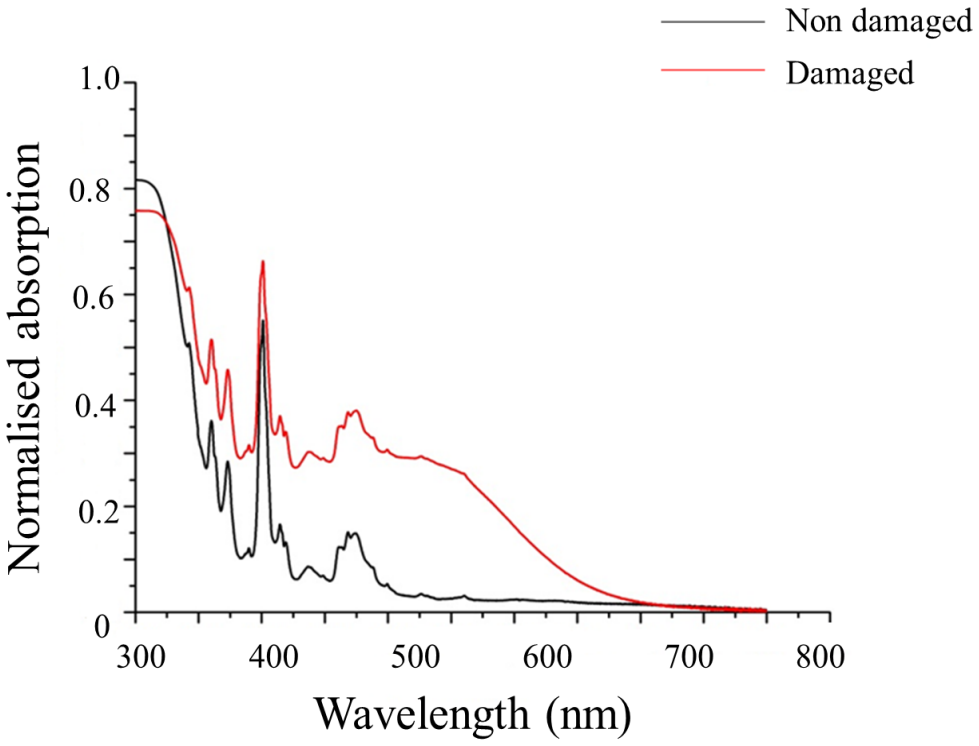

Figure 3.17: Comparison of absorption of the PKBA and PKSA samples

Further, laser experiments were performed on the PKSA glasses. The samples showed bright luminescence in the orange-reddish region and fluorescence spots were obtained without any collimating optics after the output coupler. These results indicated an encouraging trend but no lasing action could be achieved even at the maximum available pump power of 5W. Further investigations were required to investigate into the cause of the lack of lasing oscillations. In order to determine the deterring causes for lasing, excited state measurements were carried out, the details of which are included in the following section.

3.4.3 (c) Excited state absorption measurements

The population of the upper laser level sometimes could lead not only to amplification by stimulated emission, but also to absorption processes for the pump or laser radiation where laser ions are excited to a higher-lying energy level.

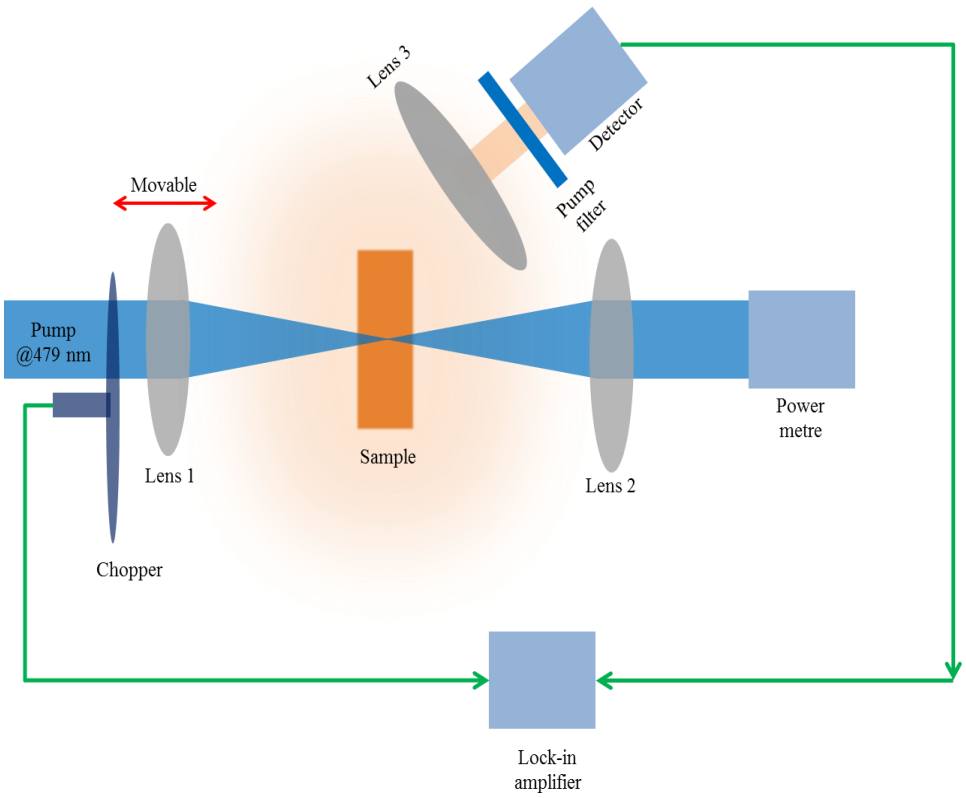

Figure 3.18: Schematic diagram for the ESA measurement setup

This is known as Excited State Absorption (ESA) and has been proven to be a deterring factor in achieving lasing action from a solid state gain [113-115].

An Experiment was performed to measure the excited state absorption in the samarium sample. The focussing lens was translated through the path of the pump beam and the focal point was passed through the sample. The change in the transmitted pump intensity was measured using a power metre. The change in the fluorescence intensity was also simultaneously recorded with a detector and lock-in amplifier. The focal length of the focussing lens was 30 mm. The experiment was repeated for different pump powers of 0.25W, 0.5W, 1W, 2W, and 4W at 479 nm. The variation in the fluorescence signal with the distance of the focussing lens was then plotted. The experiment was repeated with a different sample with double the molar concentration of the samarium ions.

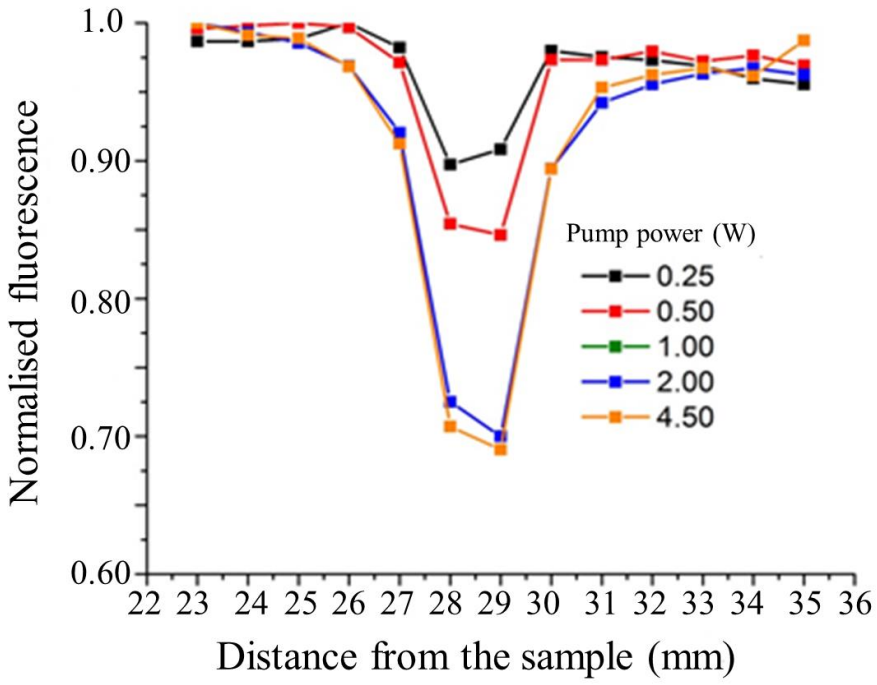

Figure 3.19: Variation of fluorescence with the distance of focussing lens from the sample (PAKNZ-Sm1.0)

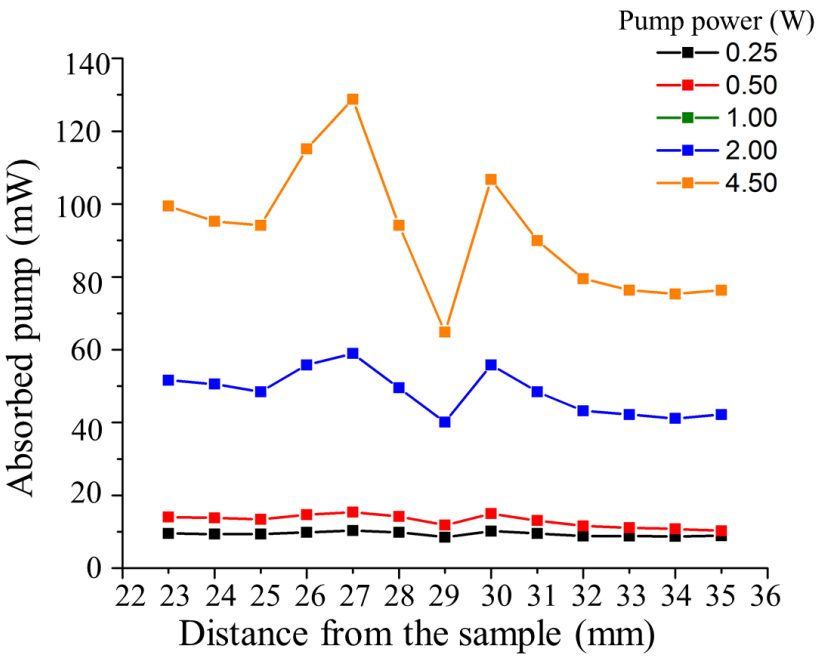

Figure 3.20: Absorbed pump vs Distance of lens from the same sample

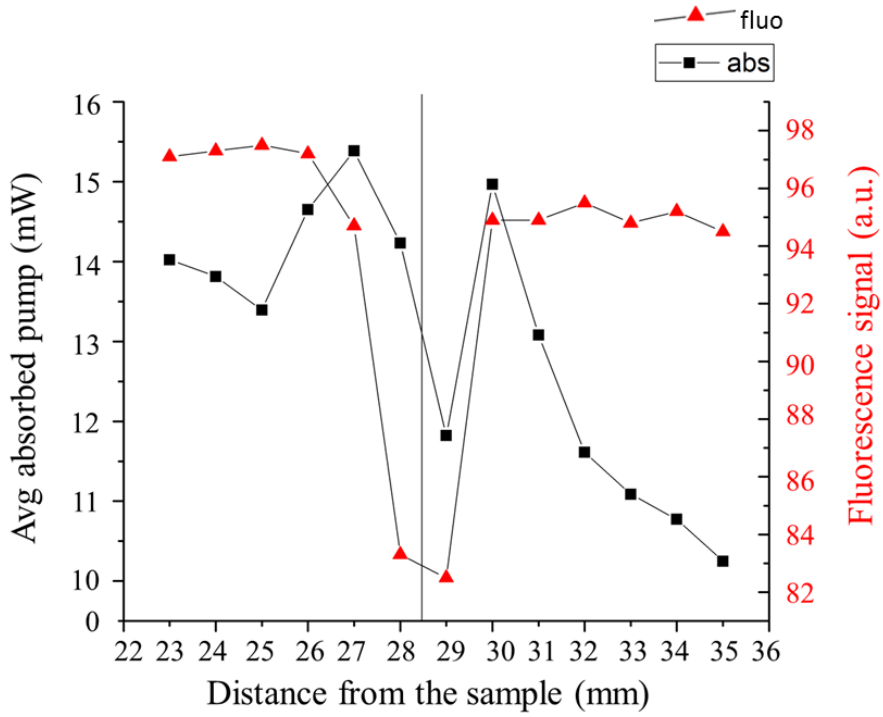

Figure 3.21: Average absorbed pump comparison with fluorescence

As can be seen from Figure 3.19, there was a significant dip observed in the fluorescence signal as the focal point of the lens was in the sample. This trend was consistent at all the pump powers.

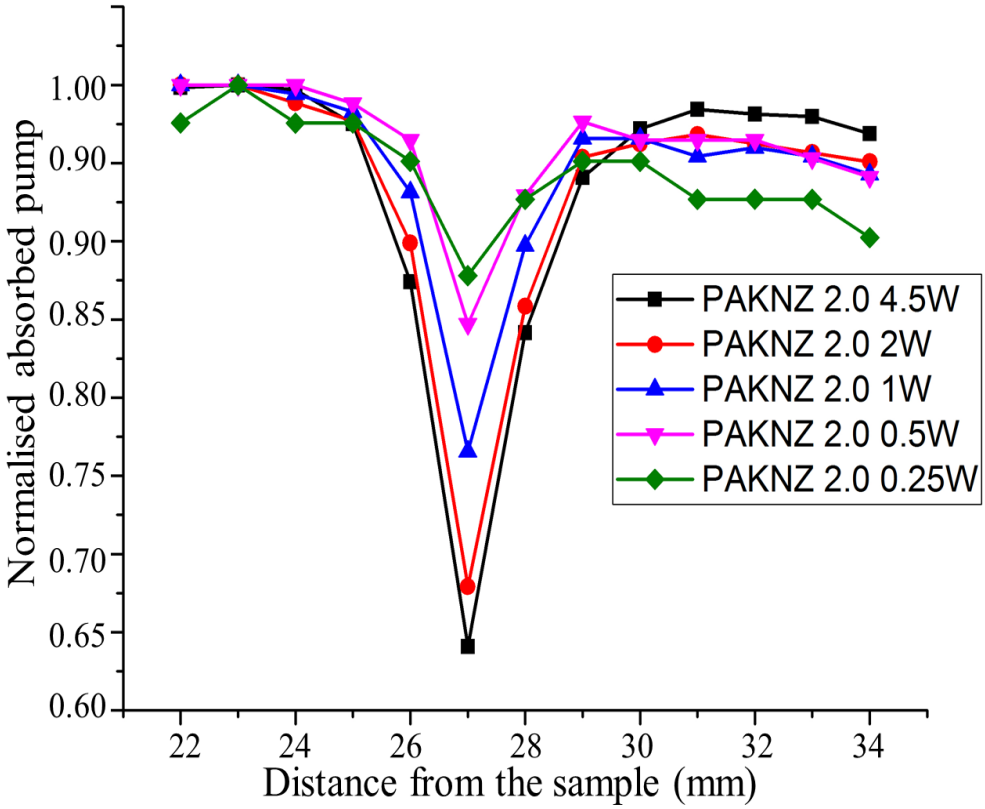

Figure 3.22: ESA measurement in PAKNZ-Sm2.0

The ESA measurements were carried out with another sample PAKNZ-Sm2.0 with double the ion concentration and similar trends were observed for that sample as well.

A careful comparison of Figures 3.19, 3.20, 3.21, and 3.22 indicates a disagreement in the expected excited state absorption phenomenon in the samples. To represent an excited state absorption at the signal wavelengths, the fluorescence should show a consistent dip in the sample with the pump focal spot in the sample. The samples show this trend consistently, with a decrease in the fluorescence up to 30%. But Figure 3.20

and 3.21 also indicate a decrease in the absorbed pump power at the focal point, which could be viewed as a contradictory phenomenon for ESA. Figure 3.21 shows a comparison between the fluorescence and the absorbed pump power at the focal point, with both the plots showing similar dips. The fluorescence shows a dip of about 13%, while the absorbed pump power shows a decrease by about 25% as the pump focal spot passes through the sample. This trend was incongruous with the expected presence of excited state absorption and it could be attributed to the existence of a secondary factor as well. It was suspected that this additional factor causing the decrease in absorbed pump power and hence the decrease in fluorescence could be bleaching effects in the sample.

3.5 Summary

Trivalent samarium ions have been studied in particular as they offer unique luminescence properties in terms of high fluorescence in the orange-reddish range of the spectrum. The spectroscopic characteristics of the ions have been discussed briefly in order to understand its optical properties. The spectroscopic studies have established that the radiative properties are highly dependent on the host materials. In the current work, extensive studies into samarium ions doped glasses have been carried out in order to realise a visible laser. Based on the current knowledge of the radiative properties of samarium ions in different environments, phosphate glasses were chosen as the host material. All the glasses with slightly different compositions were prepared by melt quenching technique at Sri Venkateswara University, India. The glasses were initially pumped with temperature controlled laser diodes operating at 405 nm. The resonator cavity configuration used was the side pumping cavity. Slight amplification in the signal was observed with the side pumping, but laser action could not be

realised. It was inferred that with higher pump absorption, laser operation could be achieved.

Type 2 waveguides were inscribed in the glasses using the technique of ultrafast laser inscription in order to check the propagation at lower wavelengths. The waveguides showed a lot of propagation losses making a waveguide laser in these glasses not viable.

A detailed study into the laser characteristics and factors affecting the realisation of the laser action in the samples has also been performed. The later stage of the work was carried out at Hamburg University. It was primarily focussed on using an optically pumped frequency doubled diode laser operating at 479 nm. No lasing action could be achieved with the pump at 479 nm with the maximum available pump power of 5W. The work was furthered with experiments including investigations into the factors which could be detrimental for laser action in the samples. We have performed the excited state absorption measurements and observed that the fluorescence from the samples showed a significant decrease in intensity as the focal point of the focussing lens was translated through the sample. This indicated the presence of ESA in the samples. However, the absorbed pump also showed a similar trend which could indicate the presence of another factor such as bleaching effects. In conclusion, lasing action in the bulk glass samples doped with samarium has not been achieved. The lack of laser action in the glasses could be attributed to the very low emission cross section of the trivalent samarium ions and studies have suggested that with higher pump powers at 401 nm, lasing action could be achieved. The other reasons against the laser action could be the presence of the combination of excited state absorption and bleaching effects in the material.

The lack of understanding of the deterring causes for lasing action in samarium doped phosphate glasses open up opportunities for some detailed investigations into the behaviour of the glasses at high pump powers. In order to understand this better, a much detailed ESA measurement experiment is required. Novel methods of pumping to utilise the maximum pump power available at 401 nm and 479 nm need to be investigated, which also opens up research opportunities for the development of high power pump sources.

Chapter 4

MULTICORE OPTICAL FIBRES FOR MULTI-WAVELENGTH LASERS

4.1Introduction

The last few decades have witnessed an enormous progress in optical fibre technology, especially in fibre based lasers and amplifiers. A lot of research has been invested into incorporating speciality fibre design in order to upgrade the data carrying capacity in optical communication and to realise novel fibre laser designs. Passive and active optical networks are the backbone of modern day communication. The ever growing data traffic has resulted in an exponential growth in the demand for capacity in the network [116]. Therefore, in order to realise a practical optical network, a low cost and high density fibre cables are required. The development of fibres containing multiple cores appears to be the most obvious approach. Multicore fibres (MCF) offer a unique solution to overcome the limitations on fibre density implementing space division multiplexing (SDM) and was first reported back in 1979 [117] and hence are considered to be the best candidate for the next generation of telecommunication networks [118]. They are also proposed for sensing applications [119], in which they enable building, e.g., shape sensors [120] or multi-parameter sensors [121].

The convergence of the enabling technologies including improvements in the fabrication methods of conventional and speciality fibres have made SDM a viable strategy. It can be achieved either by incorporating multiple cores in the same fibre or increasing the number of modes in each core. Considering the example of an optical network with a fibre with ten cores, each supporting ten modes, the data transmission capacity could be increased by a two orders of magnitude.

Incorporating the multicore geometry with active amplifier design could effectively and efficiently amplify all the spatial channels. Different forms of rare-earth doped SDM including the multicore fibre design have been experimentally demonstrated [122], [123].

Multicore fibre lasers are as well of great importance when it comes to high power single mode operations. Multicore fibres with different rare-earth dopants in each core are of interest in order to develop fibre lasers with a common pump to work as multi-band lasers. Previous efforts in Tellurite glass fibres have been able to achieve amplified spontaneous emission (ASE) in the visible, infrared and mid-infrared regions with 980 nm pumping [124]. With the changes in the design parameters and dopants, one can expect to achieve a multiple wavelength laser with a common pump from an MCF. Multicore fibre amplifiers doped with Erbium are suitable for amplifying space division multiplexed signals. Recent works on 7 core Er^{3+} fibre amplifiers and numerical simulations [125] have shown that the optimization of fibre design could lead to a significant improvement of the amplifier performance in terms of gain and power conversion efficiency.

This chapter includes the details of the experiments carried out on multicore fibres in order to realise multi-wavelength fibre laser. The details of fibre fabrication have been discussed in Chapter 2. Experimental details on the characterisation experiments carried on the fibres along with the lasing experiments have been included in this chapter. The characterisation work included lifetime measurements, loss measurements, and modal characterisation on different fibres. Lasing experiments were also performed on the fibres the results of which are discussed in details in the following sections.

4.2 Theoretical background

When it comes to fibre optics, there has been a lot of research dedicated to the understanding of the behaviour of electromagnetic fields inside the optical fibre. The guiding properties of optical fibres have been studied extensively either by electromagnetic theory [126], or by geometrical optics theory [127], or both [128]. This section briefly summarises the theoretical background associated with light propagation in conventional optical fibres. The section also discusses the electrodynamics of light propagation in multicore optical fibres.

4.2.1 Light propagation in single core waveguides

Electromagnetic field travels through an optical fibre in the form of what is known as ‘modes’. Each mode travels along the axis of the core of the optical fibre with a distinct propagation constant and group velocity, maintaining its transverse and spatial distribution. When the core diameter is small, only a single mode is permitted and the fibre is said to be single mode. Fibres with large core diameters are multimode. The analysis of the electromagnetic propagation in optical fibres presented here is based on step index fibres, which is a dielectric waveguide specified by its core and cladding refractive indices n_1 and n_2, and the radii a and b.

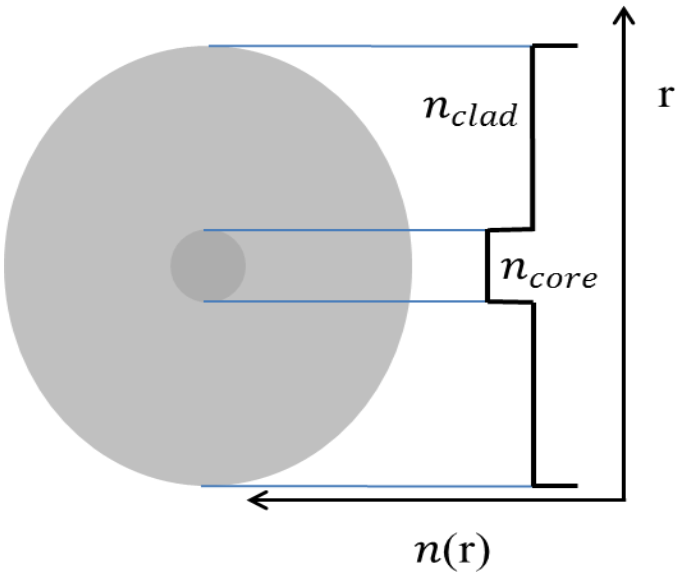

Figure 4. 1: Schematic representation of a step index fibre

The refractive indices of the core and the cladding vary only slightly, so that the fractional refractive change

$$\Delta = \frac{n_1 - n_2}{n_1} \tag{1}$$

is small ($\Delta \ll 1$).

Considering the ray optics geometry, an optical fibre can only accept light at an angle less than the acceptance angle. This acceptance angle can be calculated using Snell's law at the air-core interface and is given by:

$$\theta_a = Sin^{-1} NA \tag{2}$$

Where, NA is the numerical aperture of the fibre given by:

$$NA = (n_1^2 - n_2^2)^{1/2} \tag{3}$$

The wave optics interpretation shines some more light on the propagation of electromagnetic field inside an optical fibre. If we consider a monochromatic light

propagating in a step index fibre, one needs to determine the electric and magnetic fields of guided waves that satisfy Maxwell's equations, with the boundary conditions imposed by the cylindrical dielectric core and cladding. The certain solutions of these equations are called "modes" and they are characterised by distinct propagation constant, field distribution in the transverse field, and independent polarisation states.

In order to determine the spatial distribution of the field, let us consider the Helmholtz equation, which is given by:

$$\nabla^2 U + n^2 k_o^2 U = 0 \tag{4}$$

Where, n = n_1 in the core and n = n_2 in the cladding, and $k_o = {}^{2\pi}/_{\lambda_o}$

The Helmholtz equation in the cylindrical coordinate is given by:

$$\frac{\partial^2 U}{\partial r^2} + \frac{1}{r}\frac{\partial U}{\partial r} + \frac{1}{r^2}\frac{\partial^2 U}{\partial \phi^2} + \frac{\partial^2 U}{\partial z^2} + n^2 k_o^2 U = 0 \tag{5}$$

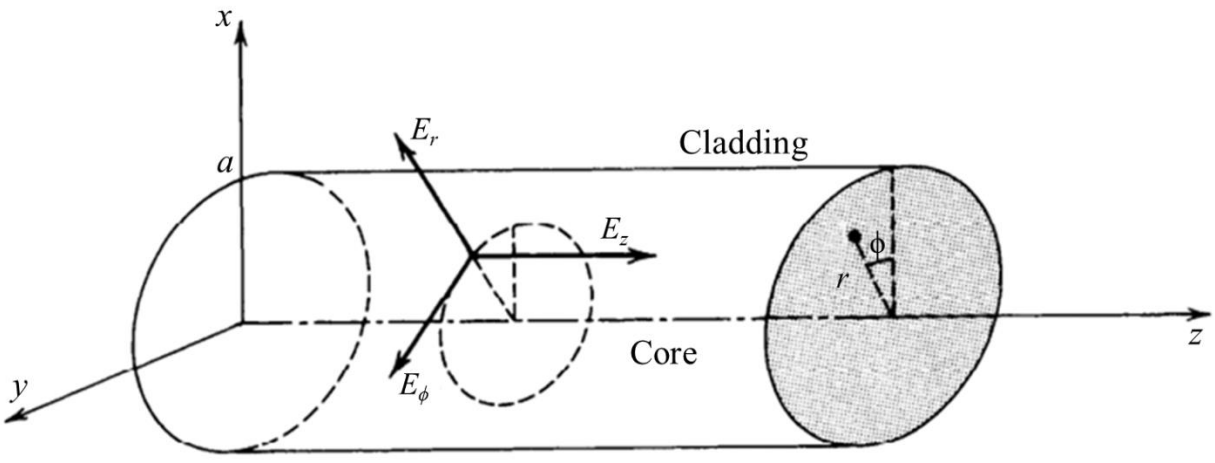

Figure 4. 2: Cylindrical coordinate system [129]

where, $U = U(r, \phi, z)$ represents any of the Cartesian components of the electric or magnetic fields or the axial components E_z and H_z in cylindrical coordinates.

If we consider the waves travelling in the z direction with a propagation constant β, the z dependence of U is of the form $e^{-j\beta z}$. Since U must be a periodic function of the angle ϕ with period 2π, we assume that the dependence on ϕ is harmonic, e^{-jlz}, where l is an integer. Substituting,

$$U = U(r, \phi, z) = u(r)e^{-jl\phi}.e^{-j\beta z} \tag{6}$$

where, $l = 0, \pm 1, \pm 2, ..$

into eq 5 we get:

$$\frac{\partial^2 u}{\partial r^2} + \frac{1}{r}\frac{\partial u}{\partial r} + \left(n^2 k_o^2 - \beta^2 - \frac{l^2}{r^2}\right)u = 0 \tag{7}$$

Now, the wave is guided if the propagation constant is smaller than the wavenumber in the core, i.e. $\beta < n_1 k_0$ and greater than the wavenumber in the cladding, i.e. $\beta > n_2 k_0$. It is therefore convenient to define

$$k_T^2 = n_1^2 k_o^2 - \beta^2 \tag{8}$$

and

$$\gamma^2 = \beta^2 - n_2^2 k_o^2 \tag{9}$$

so that for guided waves, k_T^2 and γ^2 are positive and k_T and γ are real. Equation 2 can then be written in the core and cladding separately as:

$$\frac{d^2 u}{dr^2} + \frac{1}{r}\frac{\partial u}{\partial r} + \left(k_T^2 - \frac{l^2}{r^2}\right)u = 0, \qquad \text{r < a (core)} \tag{10}$$

$$\frac{d^2 u}{dr^2} + \frac{1}{r}\frac{\partial u}{\partial r} - \left(\gamma^2 + \frac{l^2}{r^2}\right)u = 0, \qquad \text{r > a (cladding)} \tag{11}$$

Equations 10 and 11 are the well-known differential equations whose solutions are the family of Bessel functions. Excluding functions that approach ∞ at r = 0 in the core or at r → ∞ in the cladding, we obtain the bounded solutions:

$$u(r) \propto \begin{cases} J_l(k_T r), & r < a \\ K_l(\gamma r), & r > a \end{cases} \tag{12}$$

Where $J_l(x)$ is the Bessel function of the first kind and order l, and $K_l(x)$ is the modified Bessel function of the second kind and order l. The function $J_l(x)$ oscillates like the sine or cosine functions but with decaying amplitude. In the limit $x \gg 1$,

$$J_l(x) \approx \left(\frac{2}{\pi x}\right)^{1/2} cos\left[x - \left(l + \frac{1}{2}\right)\frac{\pi}{2}\right], \qquad x \gg 1 \tag{13}$$

In the same limit, $K_l(x)$ decays with increasing x at an exponential rate,

$$K_l(x) \approx \left(\frac{\pi}{2x}\right)^{1/2} \left(1 + \frac{4l^2-1}{8x}\right) \exp(-x), \qquad x \gg 1 \tag{14}$$

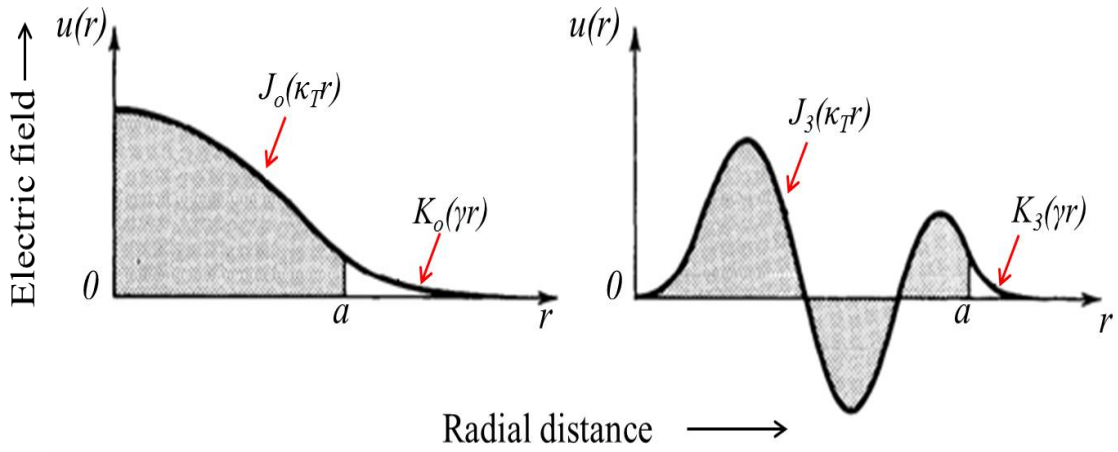

Figure 4. 3: Plot of the radial distribution *u(r)* given by equations 13 and 14 for (a) l = 0, and (b) l = 3. The shaded areas represent the fibre core and the unshaded areas represent the cladding [129]

The parameters k_T and γ determine the rate of change of u(r) in the core and in the cladding, respectively. A large value of k_T means faster oscillation of the radial distribution in the core. A large value of γ means faster decay and smaller penetration of the wave into the cladding.

The sum of the squares of k_T and γ is a constant,

$$k_T^2 + \gamma^2 = (n_1^2 - n_2^2)k_o^2 = NA^2.k_o^2 \quad (15)$$

so that as k_T increases, γ decreases and the field penetrates deeper into the cladding. As k_T exceeds NA.k_o, γ becomes imaginary and the wave ceases to be bound to the core.

From equation 15,

$$k_T^2 + \gamma^2 = (NA.k_o)^2 \quad (16)$$

Or,

$$k_T^2 + \gamma^2 = V^2 \quad (17)$$

Where, $$V = (NA.k_o) = 2\pi \frac{a}{\lambda_o} NA \quad (18)$$

is called the V parameter and governs the number of modes propagating in the fibre. For single mode step index fibres, there is a cut off frequency of V = 2.4048 corresponding to the shortest wavelength where only single mode propagation is supported by the fibre.

Most of the optical fibres are weakly guiding, i.e. $n_1 \approx n_2$ *or* $\Delta \ll 1$, so that the guided rays are paraxial. The longitudinal components of the electric and magnetic fields are much weaker than the transverse components and the guided modes are approximately transverse electromagnetic (TEM). The linear polarisation in the x and y direction then form the orthogonal polarisation states. The linearly polarised (*l*,*m*) mode is usually denoted as LP_{lm} mode. The two polarisations of mode (*l*,*m*) travel with the same propagation constant and have the same spatial distribution.

4.2.2 Light propagation in multicore waveguides

Multicore fibres incorporate two or more cores in a single fibre. The number of cores and their arrangements in the fibre depend heavily on its applications. Numbers of cores ranging from 3 [130] to 120 [131] have been reported.

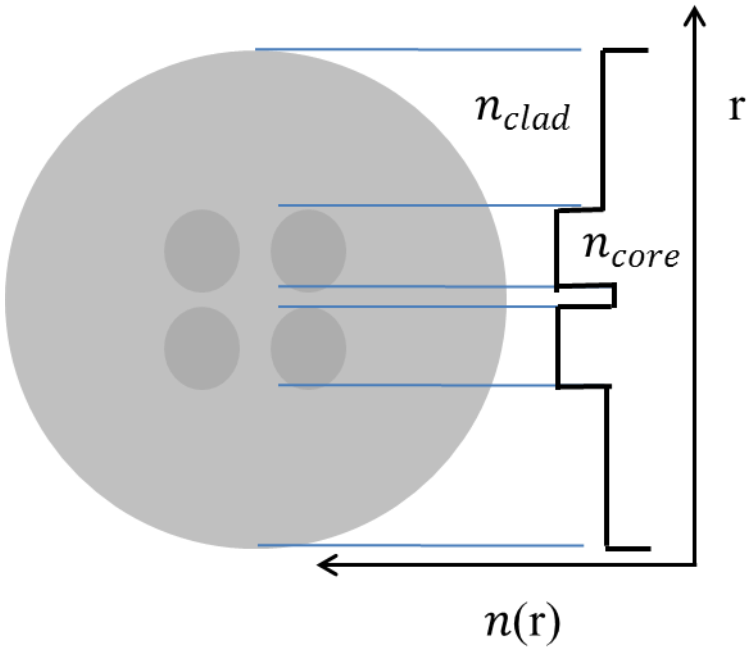

Figure 4. 4: Representation of the cross-sectional view of a four-core fibre

The propagation of electromagnetic field inside a multicore fibre has been studied and described on the basis of coupled-mode theory [132] and coupled power theory [133]. These theories describe the coupling properties of multiple-core structures. The studied carried out by [16] was based on a dual core fibre by using the point matching of boundary conditions [134, 135] to estimate the total coupled-mode fields of multicore fibres.

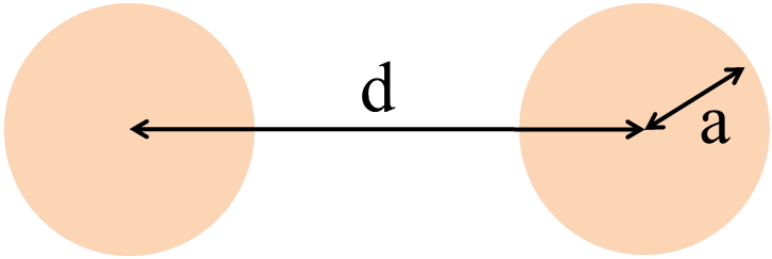

Figure 4. 5: Dual core geometry to study coupling properties

If we consider a simple dual-core geometry as shown in the figure above, with β_o being the propagation constant for both the cores, the coupled mode equation can be written as:

$$-j\beta \begin{bmatrix} A_1 \\ A_2 \end{bmatrix} = -j \begin{bmatrix} \beta_o & C(d) \\ C(d) & \beta_o \end{bmatrix} \begin{bmatrix} A_1 \\ A_2 \end{bmatrix} \tag{19}$$

Where, A_i is the amplitude of the transverse electric field of the i^{th} core (i = 1, 2), $C(d)$ is the coupling coefficient between the cores whose separation is d, and β is the propagation constant of the coupled mode.

Equation 19 can be solved as shown below:

$$\begin{bmatrix} A_1 \\ A_2 \end{bmatrix} = \begin{bmatrix} 1 \\ \pm 1 \end{bmatrix} \tag{20}$$

$$\beta = \beta^{\pm}(d) = \beta_o \pm C(d) \tag{21}$$

The propagation constants $\beta^{+}(d)$ and $\beta^{-}(d)$ can also be calculated by point matching method and the coupling coefficient $C(d)$ can be derived from these propagation constants as:

$$C(d) = \frac{(\beta^{+}(d) - \beta^{-}(d)}{2} = \frac{\Delta\beta(d)}{2} \tag{22}$$

Since the orientation of the transverse electric field vectors is not always parallel in these structures, we must take into account the angle θ made by these vectors as shown in figure below.

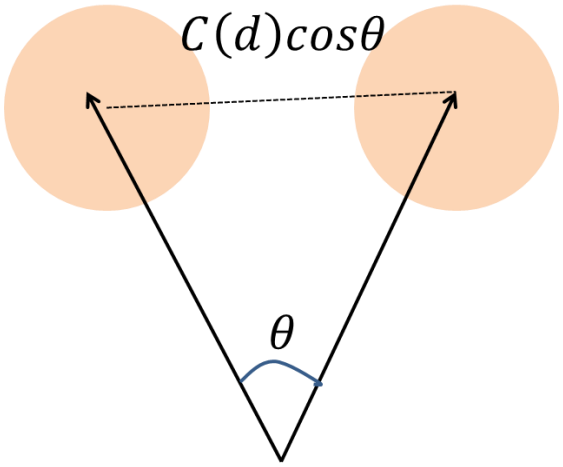

Figure 4. 6: Orientation of the transverse electric field vectors at an angle θ

Therefore, the field coupling coefficient $C(d, \theta)$ between these vectors can be defined here as

$$C(d,\theta) = C(d).cos\theta = \frac{\Delta\beta(d)}{2} cos\theta \tag{23}$$

For most of the applications of multicore fibres listed in section 4.1, it is important that the light propagation in different cores of the fibres is independent of each other, with minimum crosstalk. Cross talk in MCF greatly minimises the signal carrying capacity in the fibres. The most intuitive way of reducing the crosstalk between the cores is to increase the separation between them. There have been numerous other configurations which have been suggested and studied in order to reduce the crosstalk. Hexagonal packing of the cores has been established as the most efficient way of arranging the multiple cores inside the fibre. It has been reported that for practical limits of crosstalk of < 50 dB.km^{-1}, step index MCF's should have a core-to-core distance of at least 45 µm to allow a low crosstalk transmission with a large effective area, A_{eff}, and single

mode operation [136]. The same study showed that for trench assisted MCF (TA-MCF) the core-to-core distance can be lowered to 35 μm. Trench assisted MCF's are MCF's with a lower refractive index around the core in the cladding region of the fibre. The trench around the cores reduces the crosstalk between the cores by supressing the electric field distribution in each core due to the refractive index difference. The use of heterogeneous cores has been reported to be quite effective in suppressing the crosstalk among the cores as well [137]. The MCF contains identical and non-identical single mode cores arranged so that the crosstalk between adjacent cores becomes small. The power transferred between non-identical cores is lower than between identical cores allowing the cores to be positioned closer together.

4.3 Experimental details

4.3.1 Lifetime measurements

Measurement of the lifetimes of the ionic states is important when it comes to laser gain materials. The knowledge of the upper state lifetimes of a potential gain medium helps in deducing the transition probabilities and oscillator strengths which determine the potential lasing applications of that medium. The upper-state lifetime of a gain material can be measured by populating the upper laser level with a short laser pulse and monitoring the decay of the fluorescence. Lifetime measurements were carried out on different types of fibres doped with rare-earth elements. The main objective of this experiment was to study the effects of different co-dopants and hosts on the lifetime of the rare-earth materials such as Er^{3+}, Yb^{3+} and Tm^{3+}

Fig 4.7 shows the experimental set up for lifetime measurement. A function generator modulated the diode driver of a 980 nm laser diode at the frequency of 5-20 Hz. The available rare-earth doped fibres were pumped with the pulsed laser diode and the emission and decay characteristics were recorded.

The fibres under test were:

1. Purely Yb^{3+} doped fibre

2. Er^{3+}-Yb^{3+}-Tm^{3+} co-doped fibre (EYT-1)

3. Er^{3+}-Yb^{3+} co-doped fibre with phosphorous aluminium host (NIM EY-1)

4. Er^{3+}-Yb^{3+} co-doped fibre with phosphorous zirconium host (NIM EY-4)

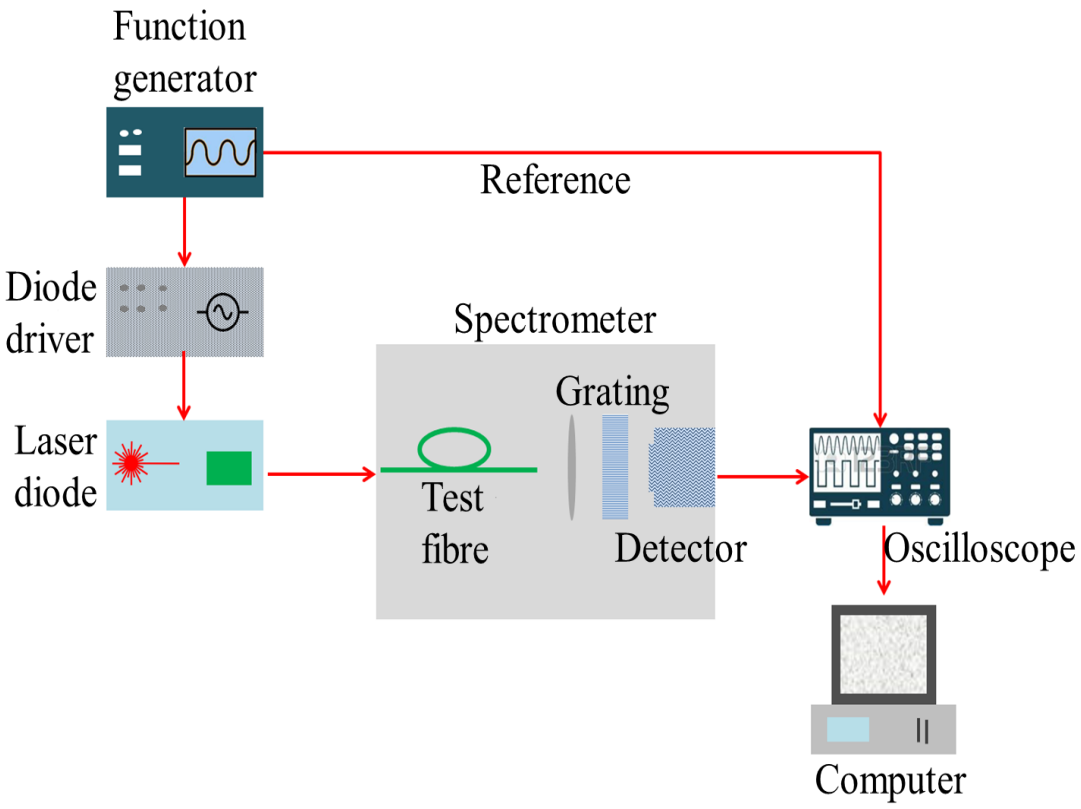

Figure 4. 7: Schematic diagram of the lifetime measurement set up

Table 4.1 below shows a comparative list of the lifetimes measured for the four types of fibres used.

Fibre	Lifetime (τ) (ms)	Standard deviation(χ^2)
Purely Yb^{3+} doped fibre	0.76	5.1
EYT-1	Er^{3+} : 8.08 Yb^{3+} : 0.58	Er^{3+} : 0.95 Yb^{3+} : 1.3
NIM EY-1	Er^{3+} : 10.28 Yb^{3+} : 1.19	Er^{3+} : 3.7 Yb^{3+} : 4.259
NIM EY-4	Er^{3+} : 10.41 Yb^{3+} : 0.97	Er^{3+} : 1.56 Yb^{3+} : 1.41

Table 4. 1: Comparison of lifetime values for different fibres

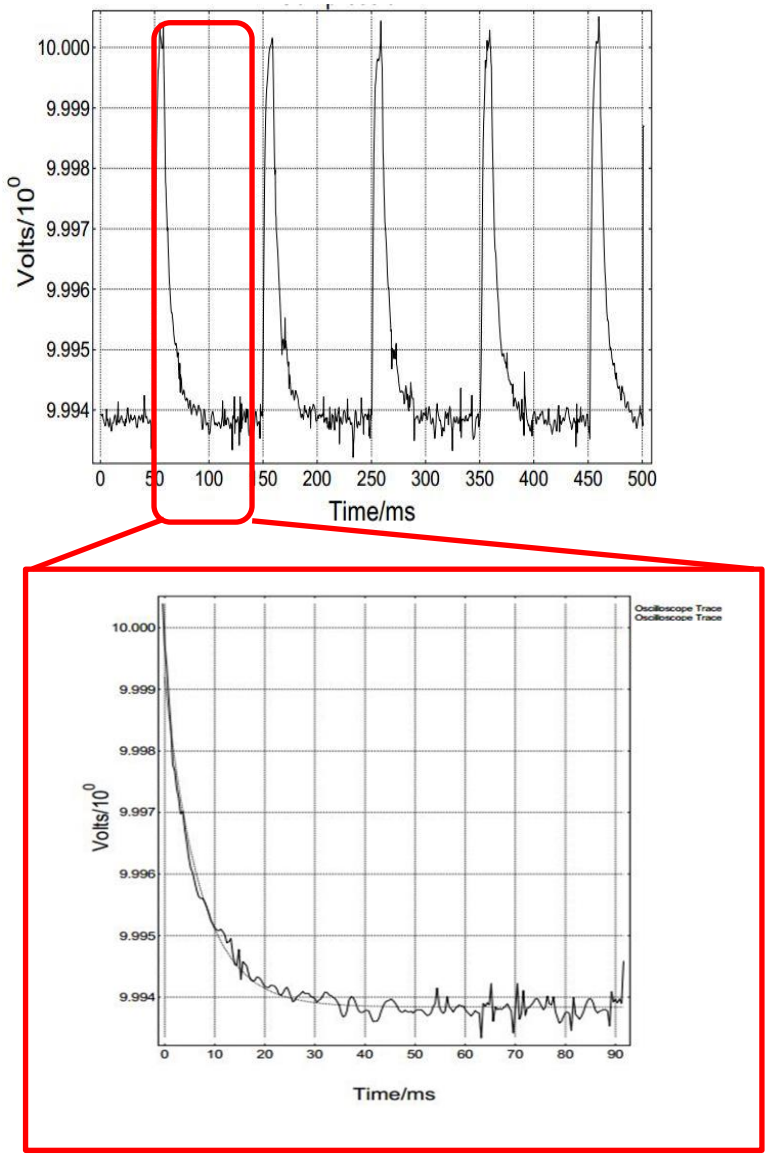

Figure 4. 8: Fluorescence decay curve and exponential fit (in inset) for EYT fibre

Fig 4.8 shows the oscilloscope plot of the decay in EYT fibre. The inset image shows the curve of the fluorescence decay. The decay lifetime is calculated by doing an exponential fit into the decay curve. The standard deviation value χ as shown in Table 1 demonstrates the accuracy of the measurement and its desirable value is around 0. The standard deviation is the difference of the measured lifetime of the measured curve as shown in Fifure 4.8 and the mean of the lifetimes of all the curves recorded.

4.3.2 Loss measurements

Optical losses in an optical fibre refer to the loss of optical power with propagation as a result of absorption, scattering, bending, and other loss mechanisms. Measuring the attenuation caused by these different factors is a crucial element of a fibre optic device realisation process. For the demonstration of fibre lasers, it is quite essential to know the absorption peaks of the active gain material doped in the fibre core. The spectral distribution of power coming out of the fibre end gives an insight into these absorption regions. Unwanted losses such as those arising because of the presence of $OH^{(-)}$ ions could be detected through the output spectrum. In communication applications, it is desirable to know the attenuation occurring in terms of loss per unit length. It is required to perform proper power budgeting.

The cutback method [6] is a widely used technique for measuring the losses in an optical fibre. Light from a Quartz halogen lamp as a white light source is coupled into the test fibre of a relatively large length and the spectral variation of the output power (P1) is first measured. This method then requires the fibre to be cut back to a much shorter length and the output power (P2) be measured, without disturbing the input launch conditions.

The attenuation at any wavelength λ is then given by:

$$\alpha(\lambda) = \frac{10}{L} log \frac{P_1}{P_2}\ dB/Km$$

Where, L is the length of the fibre cut in kilometres.

Details of procedure:

A 100 W quartz halogen source with aspheric lens controlled by constant current supply at 8.5 A was used as the broadband source.

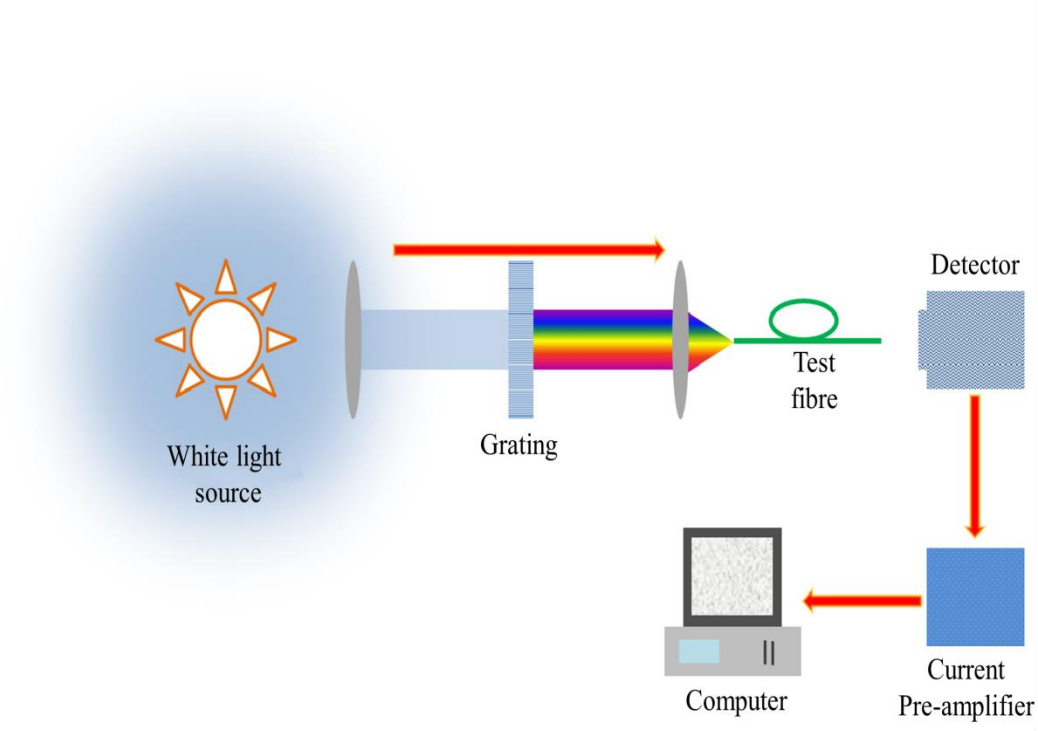

Figure 4. 9: Schematic diagram for the loss measurement set up

The launch optics included a manually adjusted precision x-y-z positioner. The test fibre, which was a single core fibre made with the same rare-earth doped preform as the MCFs, was held in a bare fibre chuck capable of holding fibres with diameters from a few microns to 250 μm. A 2 mm diameter InGaAs photodiode housing with adapter for fibre chuck was used along with a silicon detector as well to record the spectral power variations from the visible to the near IR region. White light was

passed through the monochromator (Benthem, TMc 300) before being launched into one end of the fibre under test. The grating shown represents the monochromator, which separates the white light into individual wavelengths. The light emerging from the other end of the fibre was collected by the photo detector diodes one by one and the resulting signal was amplified by a lock-in-amplifier. The fibre at the detector end was then taken out and a short length is selected, cleaved and reinserted in the detector assembly. The spectral power variation was recorded in both the cases. The loss measurement studies were carried on the following fibres:

a. Er^{3+}-Yb^{3+}-Tm^{3+} co-doped fibre (EYT-1)

b. Tm^{3+}-Yb^{3+} co-doped fibre (HTY-1)

c. Er^{3+}-Yb^{3+} co-doped fibre with phosphorous aluminium host (NIM EY-1)

d. Four core Yb^{3+} doped fibre (MC Yb-2)

e. Six core Er^{3+}-Yb^{3+}-Tm^{3+} co-doped fibre (MC EYT-2)

f. Multicore Er^{3+}-Yb^{3+} and Tm^{3+}-Yb^{3+} (MC ET-4)

The loss curves for two of the fibres are shown in Fig 4.10.

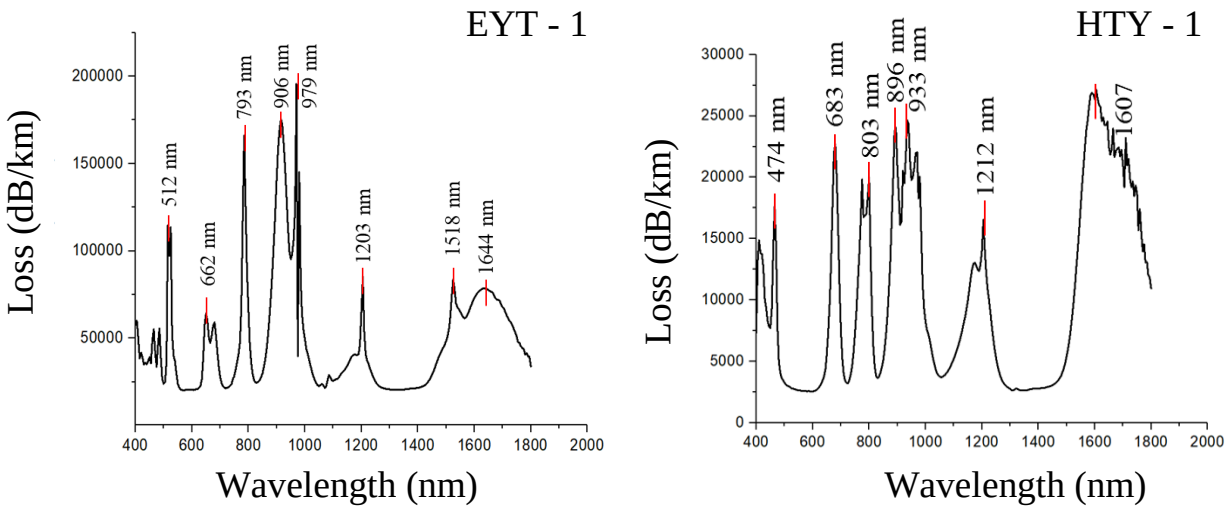

(a) (b)

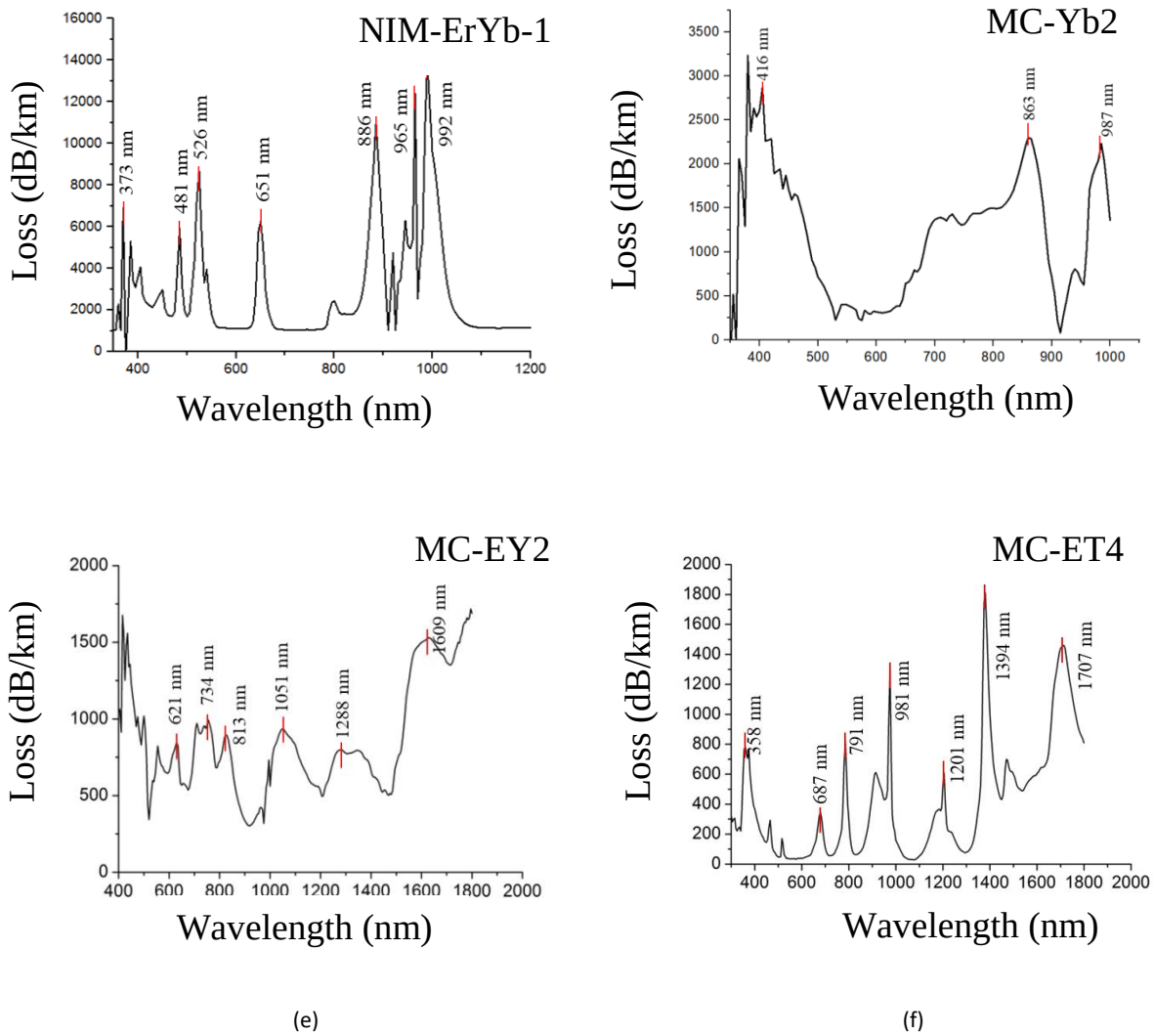

(e) (f)

Figure 4. 10: Loss curves for (a) EYT-1; (b) HTY-1; (c) NIM ErYb-1; (d) MC-Yb2; (e) EYT-2; (f) MC-ET4

Fig 4.10 (a) to (f) shows the spectral power distribution of all the fibres tested for attenuation. The distinct sharp peaks at 980 nm in the spectra denote the pump absorption due to the presence of Yb3+ ions in all the fibres. The OH^- absorption peaks appears in Fig 4.10 (f) at 1400 nm. The absorption peaks due to Er^{3+} ions can also be observed in Fig 4.10 (a), (c) and (f) at 1550 nm. The peaks at shorter wavelengths in the visible region mostly account to the scattering losses in the fibre.

4.4 Six core MCF

The six core fibre, with each core doped with erbium was fabricated from the composite preform. The fibre was fabricated and characterised with the aim to realise a multicore amplifier. All the cores were studied for their modal and propagation properties. All of the cores were pumped at the pump and signal wavelengths in order to check for their modal behaviour.

Figure 4.11 shows the far-field mode images of the six individual cores at the pump wavelength of 980 nm.

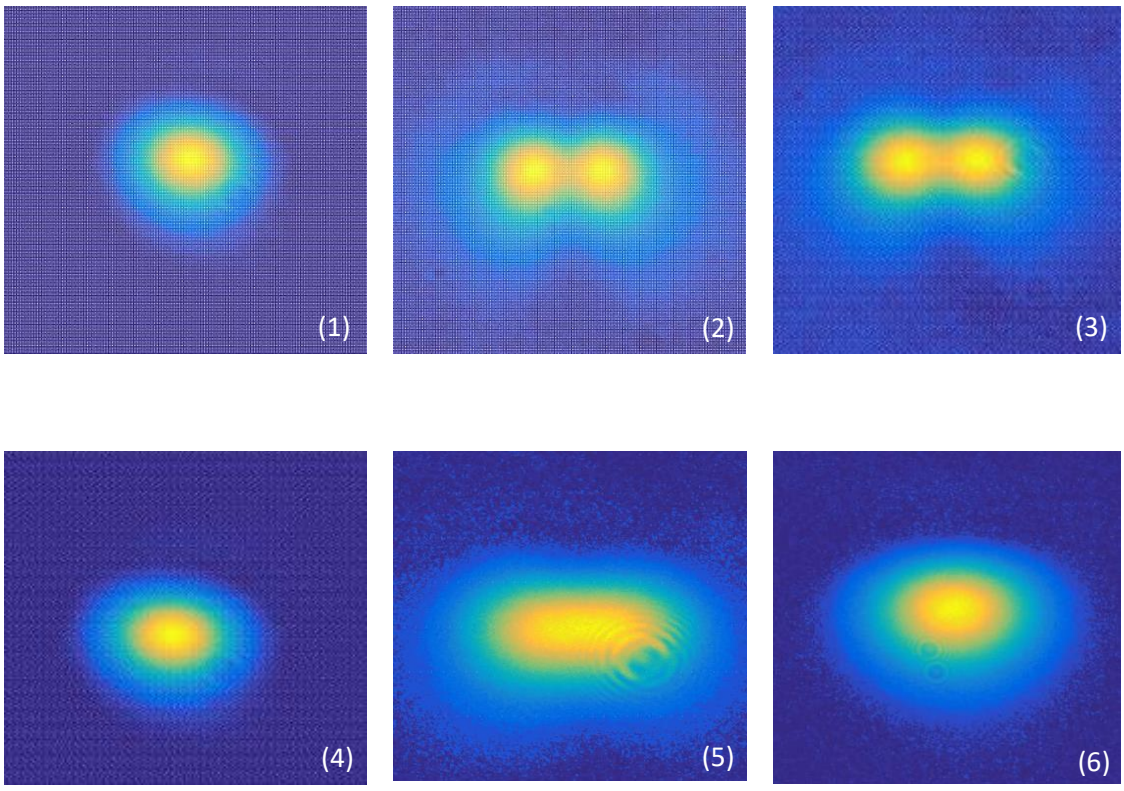

Figure 4. 11: Mode images of the six cores of the erbium doped MCF

As can be seen from Figure 4.11, three out of the six erbium doped cores were multimode at the pump wavelength of 976 nm. The multimode behaviour of three of the cores could be attributed to the difference in their core sizes. The core diameters

were measured with the help of the USAF 1952 resolution test targets and the results are summarise below in Table 4.2.

Core	**Diameter (µm)**
Core 1	4.42
Core 2	5.51
Core 3	5.49
Core 4	4.36
Core 5	5.30
Core 6	4.39

Table 4. 2: Core sizes of the six cores of the erbium doped MCF

As can be seen from the table above, cores 2, 3, and 5 have the diameters > 5.3 µm, as compared to the other three cores, which is in the range of 4.35 to 4.42 µm. These differences in the core diameters occur due to the imperfect fibre drawing conditions, such as non-uniform hole sizes in the passive preform, different fibre drawing speeds for different cores, and non-uniformity in the rare-earth doped preforms.

Loss measurements were carried out on the fibre with the same process as explained in section 4.3.2.

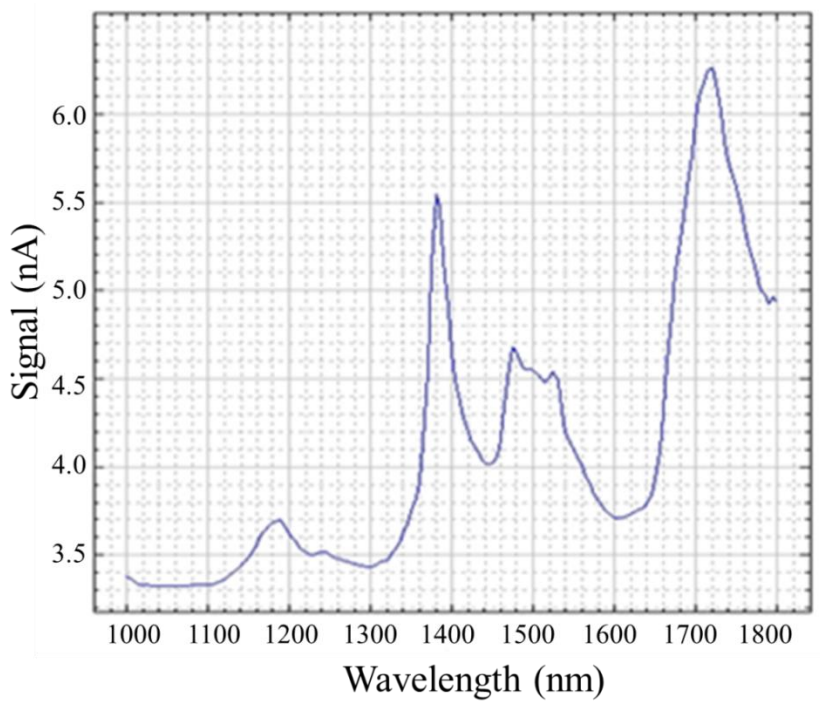

Figure 4. 12: Collective Loss curve for the six core MCF when cladding pumped (Provided by CGCRI)

The peak around 1400 nm could be attributed to the absorption from the $OH^{(-)}$. The absorption peaks due to Er^{3+} ions can also be observed in Fig 4.10 (a), (c) and (f) at 1550 nm. The loss was measured for the entire fibre, as the light was launched through the cladding, rather than the individual cores.

4.4.1 Gain measurement

Most of the research and progress in optical communication has been based on increasing the data carrying capacity of optical fibres in order to avert the bandwidth crunch. Researchers have been able to optimise multiplexing in time, wavelength, phase, and polarisation to the extent where commercial systems now utilise all four dimensions to send more information through a single fibre. However, multiplexing in the spatial dimension in a single fibre has remained comparatively untapped. Multicore active fibres provide a great alternative to realise space division multiplexing (SDM). The six core erbium doped fibre discussed above has been tested

for the SDM applications and the results have been discussed below. The individual cores have been subjected to gain measurement studies.

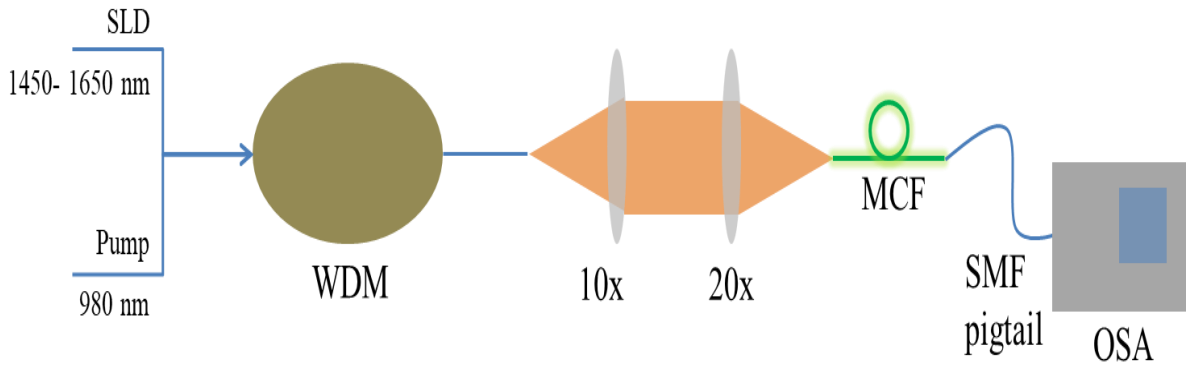

Figure 4. 13: Schematic diagram for the gain measurement setup

Figure above shows the schematic diagram of the setup used for the gain measurement. The individual cores were pumped with a laser diode operating at 980 nm through a wavelength division multiplexer (WDM). The WDM allows the simultaneous injection of the pump and signal into the multicore fibre (MCF). The signal source was a superluminescence diode (SLD) generating a broadband spectrum of light in the range of 1450 nm to 1650 nm and the pump was a laser diode operating at 980 nm. The light out of the WDM is collimated and coupled into the MCF. A singlemode fibre (SMF) is coupled to the individual cores of the MCF by maximising the light coming out of it with a camera. After the SMF was appropriately coupled, an optical spectrum analyser (OSA) was used to measure the spectrum from the cores. In the presence of the pump, we expect to achieve amplification in the signal at around 1550 nm.

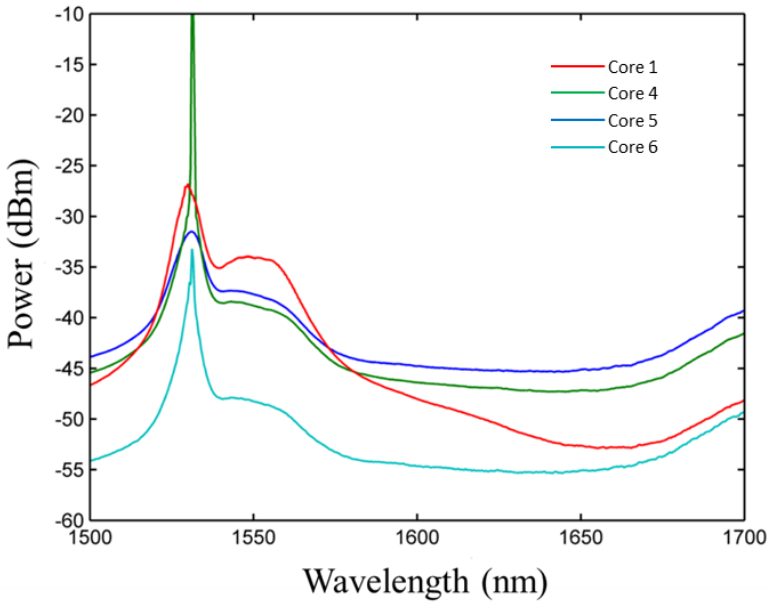

Figure 4. 14: Emission spectrum from the four cores with pumping at 980 nm

Figure 4.14 above shows the emission spectrum of the four single mode cores out of the six cores pumped at 980 nm. Gain measurements were performed on these cores. All the four cores show the typical erbium emission spectrum with the 980 pump with a spike and shoulder around 1550 nm. Figure 4.15 below shows the spectra of the SLD source through the four cores under examination. It was recorded in order to perform a comparative study of the amplification in the signal after the pump is launched through these cores.

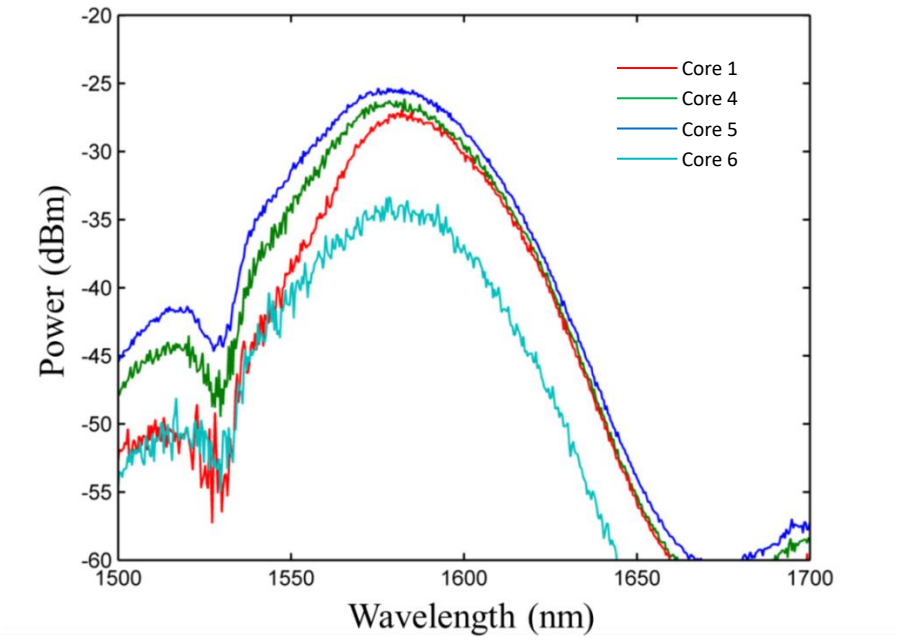

Figure 4. 15: Spectrum of the SLD source through four cores

Figure 4.16 below shows the spectra of the signal and pump combined in the range of 1500 nm to 1700 nm. As can be seen from comparing Figure 4.15 and Figure 4.16, all four cores show a considerable gain in the wavelength range of 1500 nm to 1600 nm.

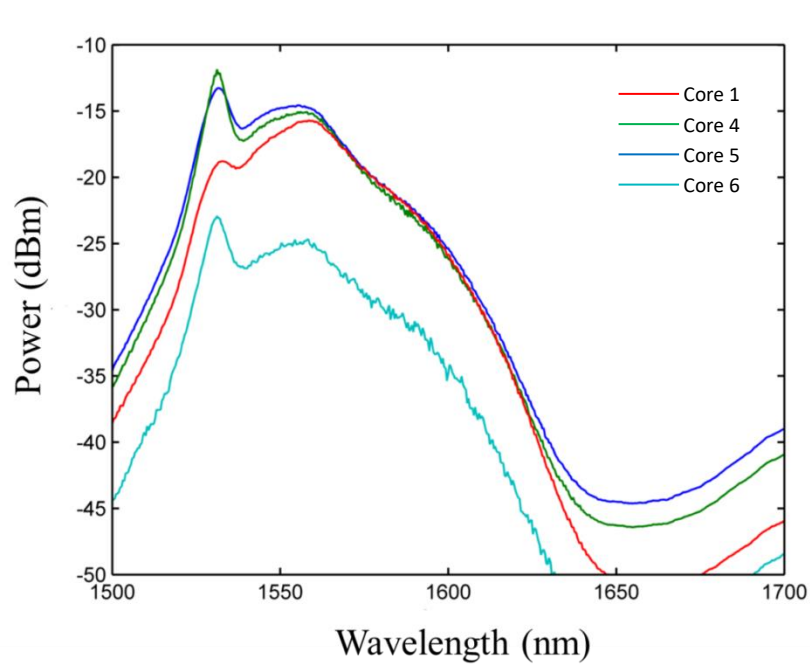

Figure 4. 16: Combined pump and signal spectra through the four cores

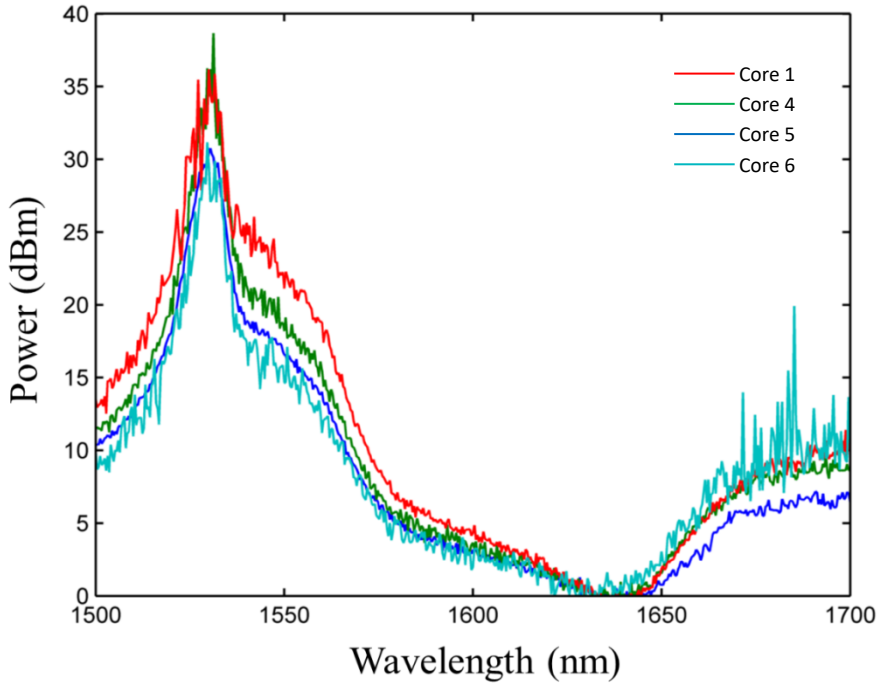

Figure 4. 17: Gain spectra of the four cores

Figure 4.17 above shows the net gain spectrum in the four cores in the wavelength range of 1500 nm to 1600 nm, which is the difference of the spectra in Figure 4.16 and Figure 4.15. As can be seen from the figure, all the four cores showed considerable gains in this wavelength range, with the gain being 30 dB to 38 dB per metre around 1530 nm. All the four cores showed demonstrated similar gain curves consistently. These results indicate that the erbium doped multicore fibre could be used for active multiplexer applications where the amplification and multiplexing could be carried out in the same fibre, resulting in the simplification of the design and cost reduction.

4.4.2 Laser based experiments

One of the other applications of a multimode active fibre could be to produce laser operation in all the cores and then beam combine them in order to produce a supermode output. This could facilitate in the power scaling of the commercial fibre

laser systems. With this application in aim, all the cores of the six core fibre were examined for laser operation. Only one of the six cores in the erbium doped fibre (EDF) showed lasing with Fresnel reflection from the facets of the fibre.

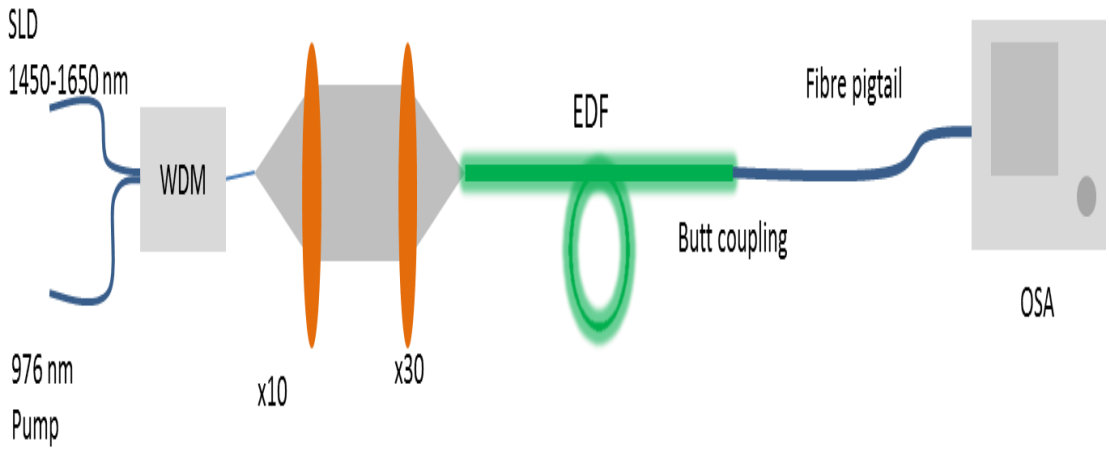

Figure 4. 18: Schematic diagram of the Fresnel reflection cavity

Figure 4.18 above shows the schematic diagram of the Fresnel reflection cavity used for laser experiment with the fibre. As can be seen from the figure, the output light was collected with a multimode fibre pigtail and coupled into the OSA. Lasing was observed at a threshold of around 220 mW of pump power. Lasing lines around 1530 nm were observed with the input pump power of more than 220 mW as shown in Figure 4.19. A ring cavity was then formed with the EDF and the same core was pumped with 976 nm laser.

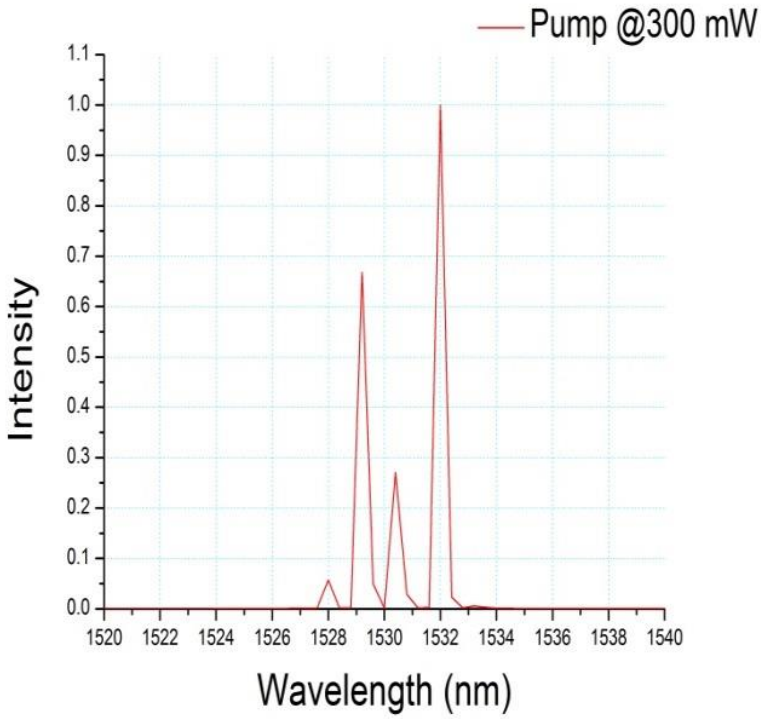

Figure 4. 19: Spectrum of the laser emission from Fresnel reflection cavity

Figure 4.20 below shows the schematic diagram of the ring cavity employed. A fibre output coupler with 30% output coupling was used. An isolator was used to ensure unidirectional light propagation. An isolator was used to avoid the back reflections of the laser into the laser diode. It was observed that lasing was achieved at a considerably low threshold of around 65 mW, which was considerably lower than the threshold with the Fresnel reflection cavity, as expected.

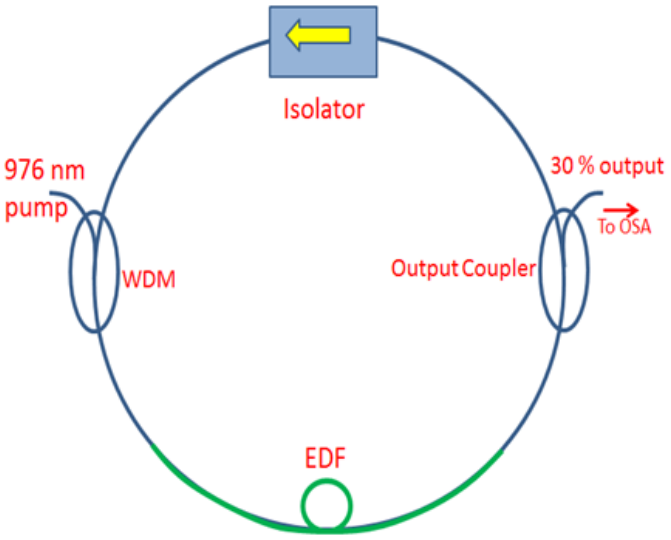

Figure 4. 20: Schematic diagram of the ring cavity

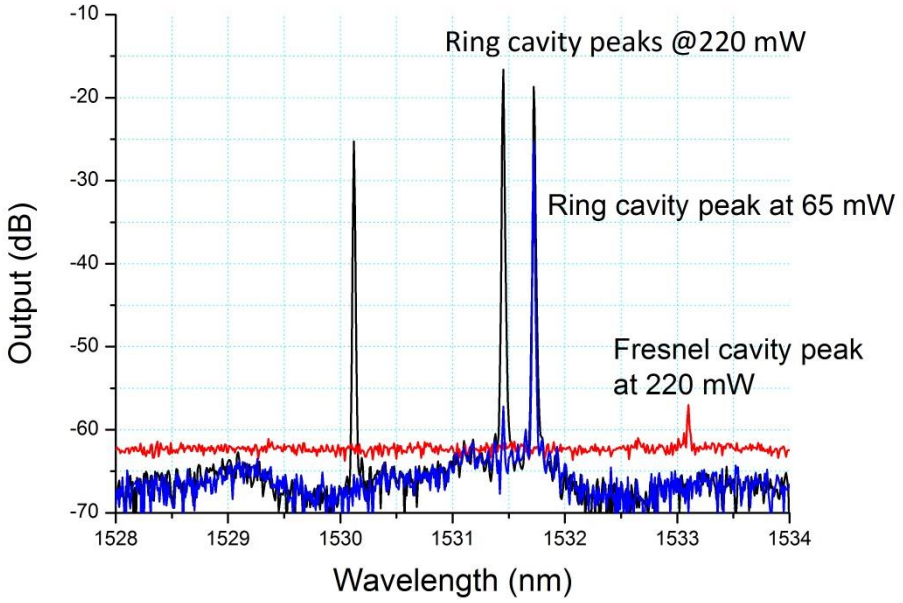

Figure 4. 21 Laser spectrum comparison of ring cavity and Fresnel reflection lasing

Fig 4.21 above shows a comparison between the ring cavity and the Fresnel cavity lasing. Ring cavity was observed to cause a significant decrease in lasing threshold from 220 mW to 65 mW. The blue curve shows the lasing with ring cavity at 65 mW. The black peaks are the laser peaks at 220 mW, same as the threshold for Fresnel

cavity for comparison. The other cores did not show laser action even with the incorporation of ring cavity.

4.5 Two core MCF

Lasers operating at multiple wavelengths have been of great interest with the focus being mainly on erbium doped gain media for applications into dense wavelength division multiplexing (DWDM) in telecommunications. Multi-wavelength lasers have also found applications in sensing [138] and optical instrumentations. Realizing a stable multi-wavelength operation from erbium doped fibres has proved to be difficult because erbium ion saturates mostly at room temperature. Different techniques have been suggested and reported in order to achieve a stable multi-wavelength operation around 1550 nm within the span of a few nanometres [139, 140]. Over the past decade, the generation of stable multi-wavelength source has been quite well established. Unfortunately, considering the extensive research that has gone into it, the span of the wavelengths generated has been rather limited and centred around 1550 nm region. Surprisingly, there has been very little research on generating a multi-wavelength source spanning beyond few nanometres. Such laser sources could have a multitude of applications in multi-element sensing, two colour pump probe experiments, and sum and difference frequency generation. It could also revolutionize the field of Differential Absorption Lidar (DIAL) systems by miniaturizing them to highly portable scales.

Given the great developments in the fabrication technology of speciality optical fibres, it is about time that multicore fibres go beyond the telecommunication and sensing realm of applications and enter the multi-wavelength laser domain. Multicore fibres with different rare-earth dopants in each core are of interest in order to develop gain fibre with a single pump to operate as multi-band lasers. Previous efforts in Tellurite

glass fibres have been able to achieve amplified spontaneous emission (ASE) in the visible, infrared and mid-infrared regions with 980 nm pumping [124]. The multicore configuration, allows the optimization of design parameters and dopants, as a result one can expect to achieve a multiple wavelength laser with a common pump from it. Multi-rare-earth doped multicore fibres could pave ways to generate multi-wavelength sources beyond the telecommunication range. This would help realize stable and compact multi-wavelength laser sources for myriad applications.

In the current work, the two core fibre was fabricated with the aim to demonstrate dual wavelength lasing with simultaneous pumping. The fibre was manufactured by the same process as described in chapter 2. The two cores were doped with ytterbium and erbium-ytterbium respectively. The erbium core was co-doped with ytterbium in order to facilitate the energy transfer at the pump wavelength. The objective with this fibre was to demonstrate simultaneous laser operation at the wavelengths of 1 µm and 1.5 µm from the ytterbium and erbium doped cores, respectively.

The fibre parameters are summarised in the table below.

Fiber parameters	Values
Core sizes	5.52 and 5.24 micron
NA with respect to each core	0.20
Distance between two cores	45.16 micron
Doping levels of Yb for one core	Yb_2O_3: 4.9 wt%
Doping levels of Er & Yb for second core	Er_2O_3: 0.457 wt%, Yb_2O_3: 5.1 wt%
Fiber coating material	Low RI resin

Table 4. 3: Parameters of the two core fibre

The figure 4.22 below shows the microscopic image of the cross section of the two core fibre.

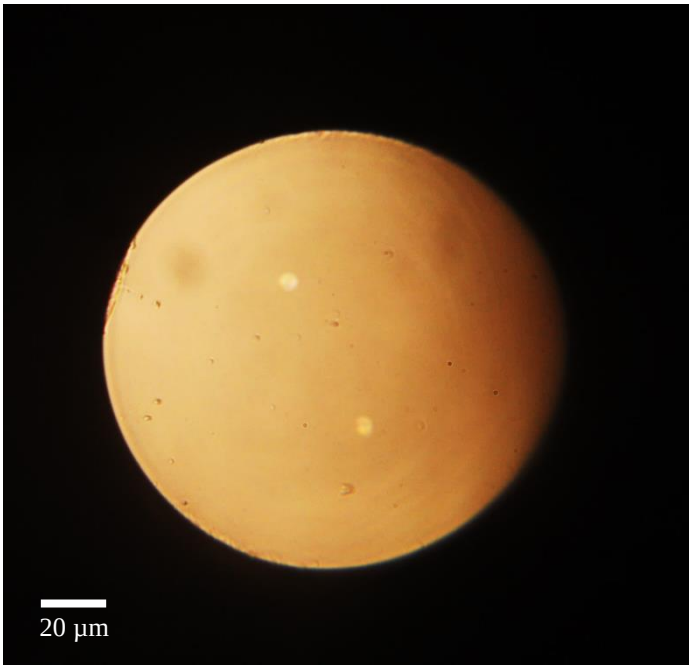

Figure 4. 22: Microscopic image of the two core fibre facet

The modal and propagation properties of the fibre were studied in order to determine its suitability for the laser experiments.

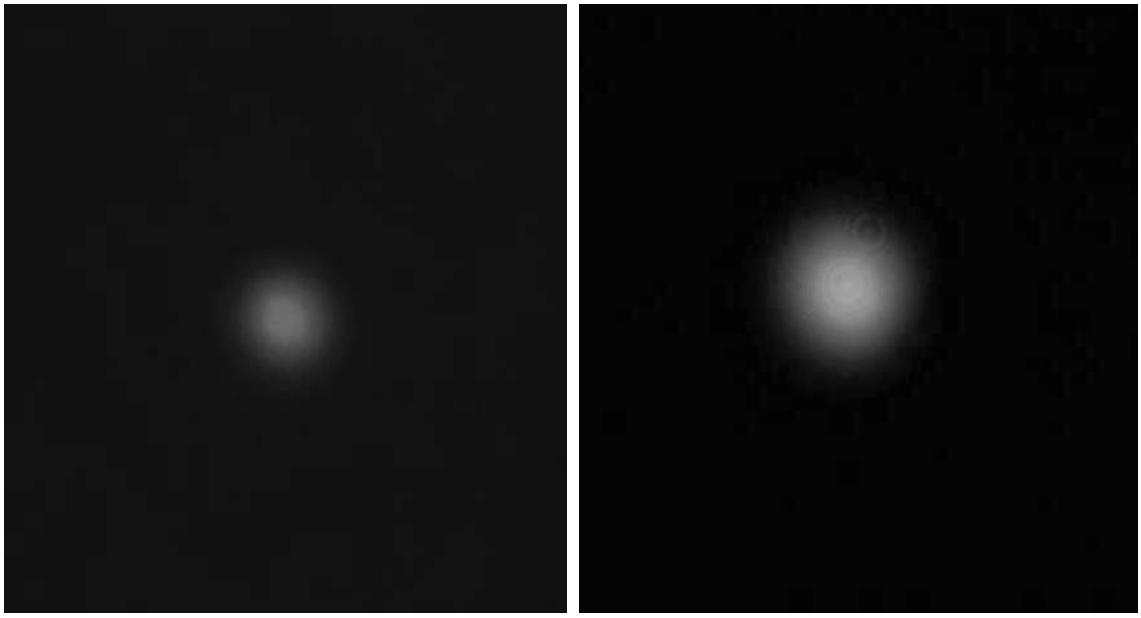

Figure 4. 23: Mode images of (a) Er-Yb core; (b) Yb core

Figure 4.23 above show the far field mode images of the two cores recorded with a silicon camera at the pump wavelength. As can be seen from the figure, both cores were found to be single-mode.

Loss measurements were carried out on the fibre with the process described in section 4.3.3. The fibre was cladding pumped with the broadband source and the spectrum was recorded.

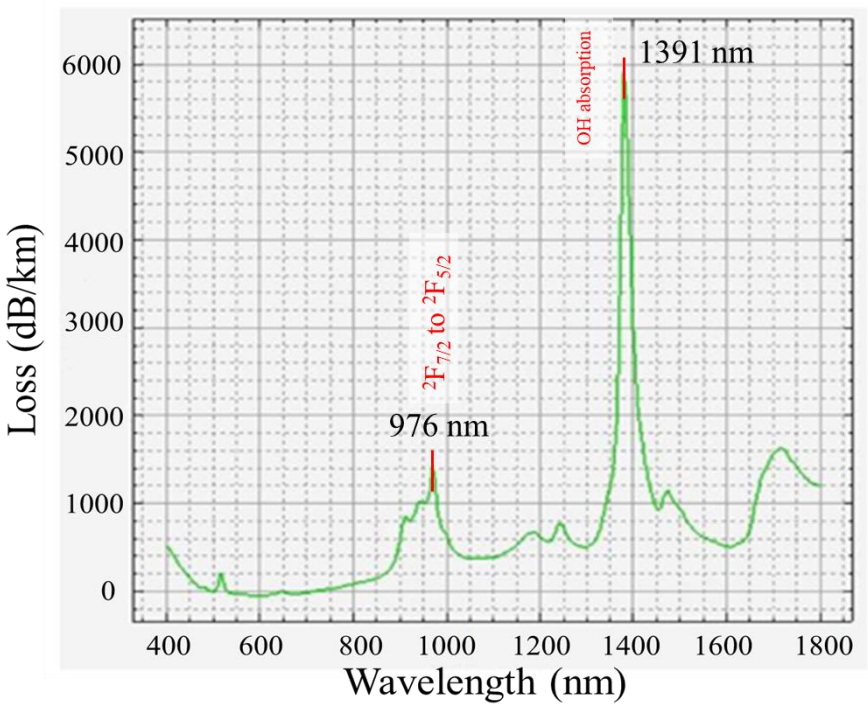

Figure 4. 24: Collective loss spectrum for the two core fibre when cladding pumped (Provided by CGCRI)

The plot above shows the absorption spectrum for the two core fibre. It was measured again by a cut back technique as discussed in section 4.3.2. The plot indicates a loss of less than zero around 600 nm, which could be because of the error in background substraction. Due to the unavailability of raw data (as this plot was provided by CGCRI with the fibre), it could not be corrected. In this case, rather than measuring the losses in individual cores, the loss was measured for the collective fibre. Light was launched into the cladding of the fibre and the output was recorded. Therefore, the

spectrum shown in the figure above represents the loss for the entire fibre, rather than the individual cores. One of the interesting features of this plot is the complete absence of the absorption peak at around 1550 nm, which is characteristic of the erbium spectrum, which has been shown in Figure 3.3. The potential cause of the lack of this peak could be the improper interaction of the cladding light with the erbium core. The lack of absorption in the erbium core thus manifests itself as the absence of the absorption peak in the spectrum. The peak at around 980 nm could be attributed to the absorption by the Yb ions. The absorption spectra shown in Figure 3.2 also shows the peak at around 980 nm, which is the characteristic absorption in ytterbium ions for the $^2F_{7/2}$ to $^2F_{5/2}$ transition. The OH- absorption manifests itself as the huge absorption peak at around 1400 nm.

4.5.1 Laser experiments

The two core fibre was cladding pumped with a 7 W temperature controlled fibre coupled laser diode operating at 976 nm. In the cladding pumping method, the pump is launched into the cladding of the fibre, rather than the individual cores. The epoxy resin coating has a lower refractive index than the cladding and thus acts as a second cladding to the fibre. This forces the light to be contained within the cladding rather than escaping out of it. Cladding pumping has been employed to ensure optimum coupling of the pump with both the cores simultaneously. The length of the fibre used for this experiment was optimized to 4 meters for optimum pump absorption. The input pump fibre was butt coupled to the two core fibre (TCF) and the output signal was collected and collimated from its other end. As the pump power was ramped up, laser action was observed from both the cores with Fresnel reflections from the cleaved fibre facets, which acted as 4% reflective mirrors. The output signal was filtered for the residual pump and split into two for spectral and modal

characterization. Figure 4.25 below shows a schematic representation of the experimental setup.

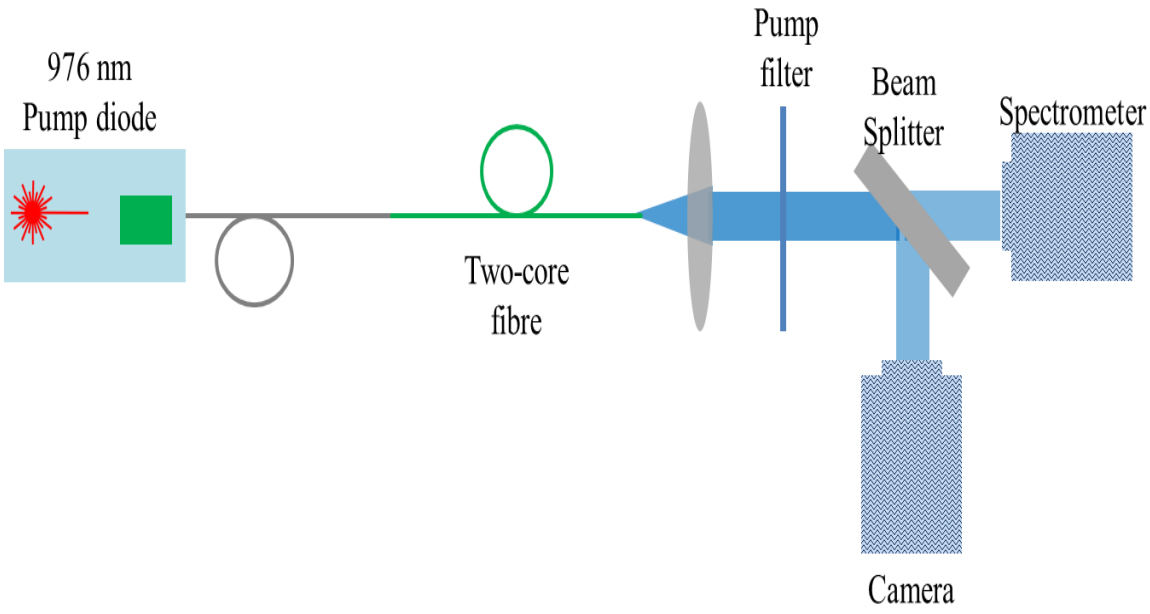

Figure 4. 25: Schematic diagram of the Fresnel reflection cavity with the two core fibre

Both of the cores showed simultaneous lasing action at around 1061 nm and 1536 nm respectively with cladding pumping. Figure 4.26 shows the signal spectrum from the TCF, with lasing peaks at 1061 nm and 1536 nm. The FWHM at 1061 nm was measured to be 0.12 nm and that at 1536 nm was 0.51 nm.

The performance from both the cores were relatively comparable with maximum output powers from the Er/Yb core and Yb core to be 34 mW and 22 mW, respectively. The absorbed power v/s output power characteristic was measured from both the cores individually. This was done by using band pass filters for the signal wavelengths and pump filters in order to strictly measure the power at one particular wavelength at a time. The absorbed vs output power for both the cores was plotted as shown in the Figure 4.28 below. The thresholds for the Er-Yb core and the Yb core were measured to be 0.8 W and 1.3 W, respectively.

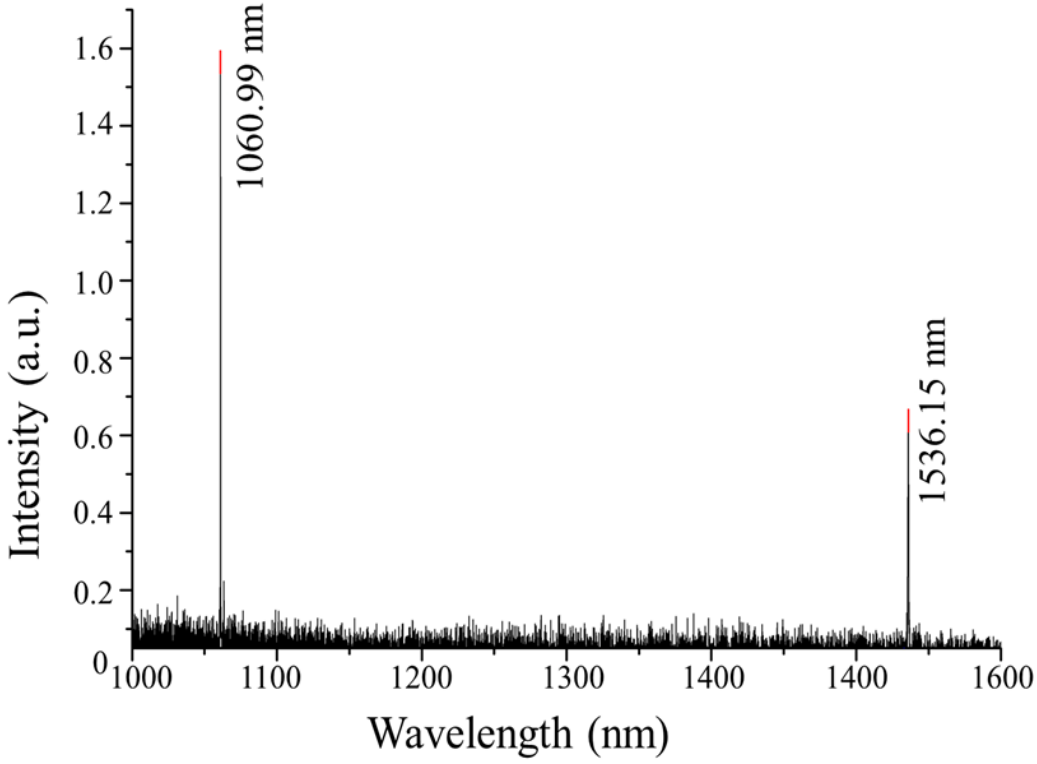

Figure 4. 26: Laser spectrum of the two core fibre showing laser spikes at 1536 nm and 1060 nm

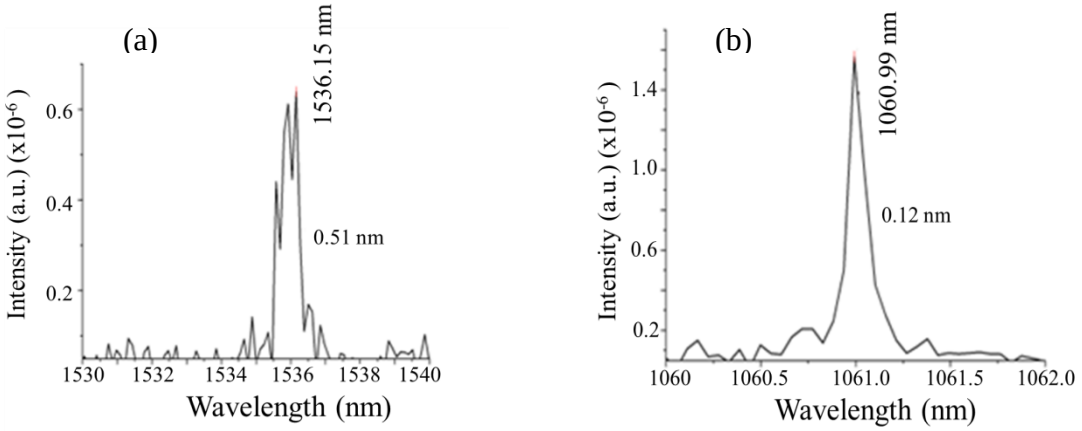

Figure 4. 26: Zoomed in spectra of the lasing peaks at (a) 1536 nm and (b) 1060 nm

As can be seen from Figure 4.28 below, both of the cores showed a linear input power v/s output power relationship.

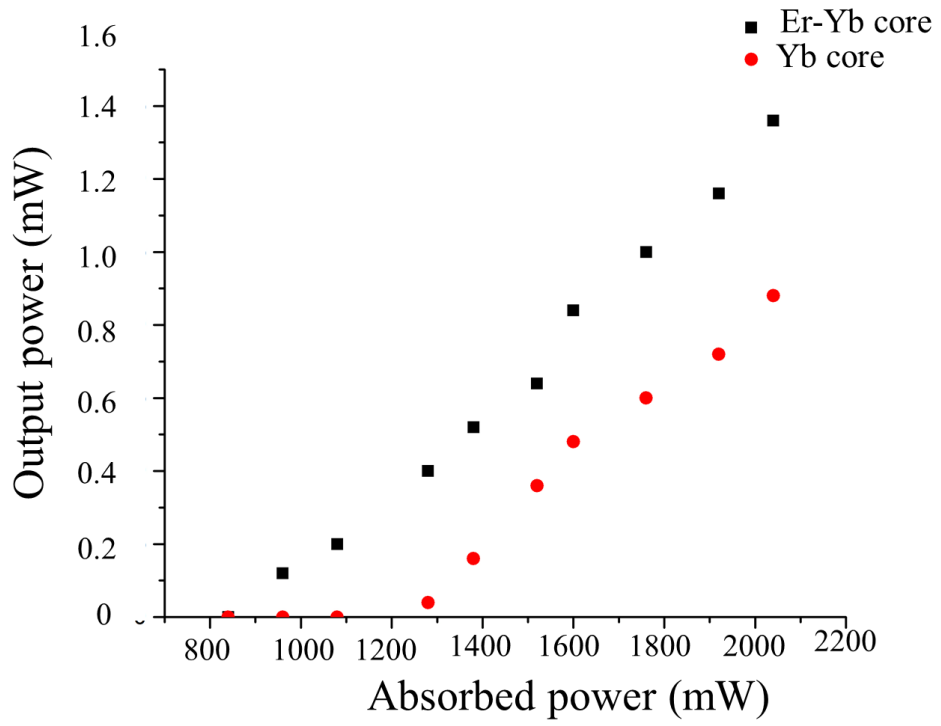

Figure 4. 27: Absorbed power vs output power characteristics for both cores with maximum output powers of 34 mW and 22 mW from the Er-Yb and Yb cores respectively

The low slope efficiency (<1) for both the cores could be attributed to the considerably low reflectivity off the fibre facets. This could be significantly improved by the use of higher reflectivity mirrors. The laser characteristics of both the cores have been evaluated against the absorbed power by the cores. In order to calculate the absorbed power by each core, the absorbed power across the entire fibre was divided by two, assuming similar absorption from both the cores, and losses due to coupling and Fresnel's reflections were also compensated for. The energy dissipated through upconversion in both the cores has been ignored while calculating the absorbed power. Therefore, the thresholds for the Er-Yb and Yb cores, which was found out to be 0.8

W and 1.3W of absorbed power, respectively, gives the upper limit for the threshold values.

The far field images of the modes were captured and both the cores were found to be single mode at the respective wavelengths. Figure 4.29 shows the simultaneous lasing modes after the pump filter recorded after collimating the output with a low magnification lens. The spatial profiles of the two cores were recorded to be near Gaussian. The modes from both the cores were spatially separated as seen in Figure 4.30 and lasing independent of each other. There was no emission at 1 μm observed from the Er-Yb doped fiber, establishing that the concentration ratio for the ytterbium to erbium in that core was perfect for the energy transfer, without leaving any residual emission from the ytterbium ions.

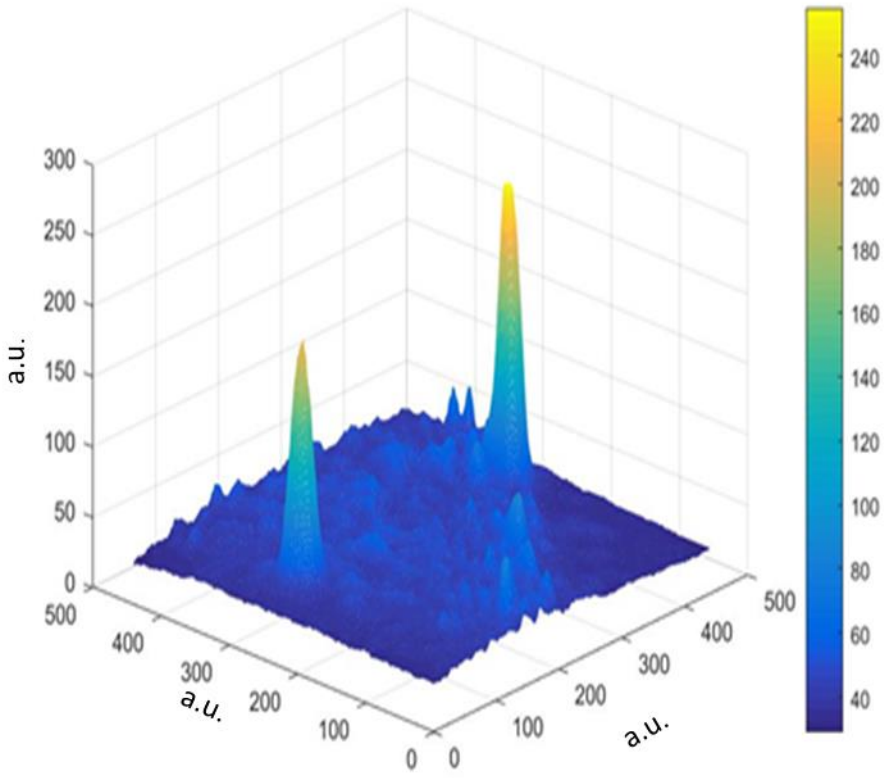

Figure 4. 28: Simultaneous dual lasing modes from the two core fibre

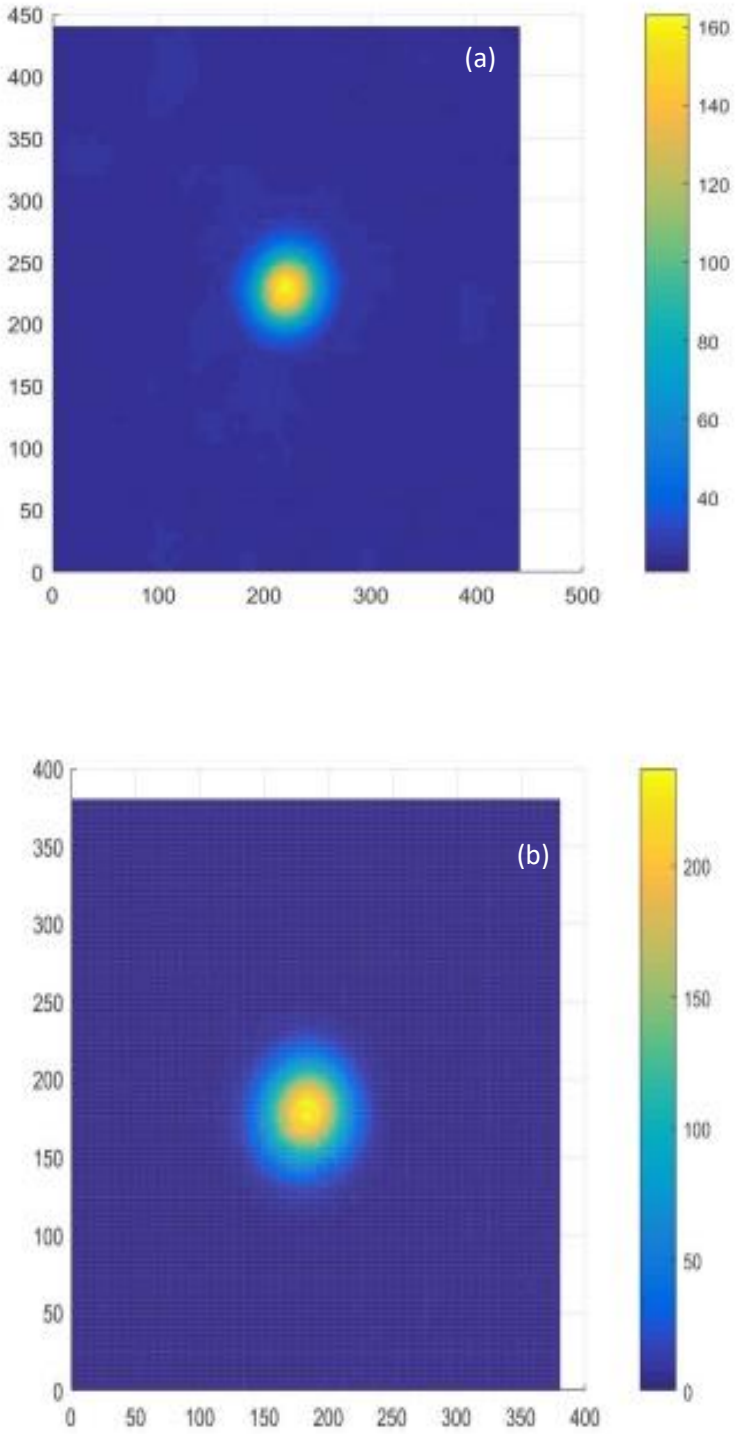

Figure 4. 30: Laser modes at (a) 1060 nm and (b) 1536 nm

Such an operation of a dual wavelength fibre laser presented here is the first of its kind, demonstrating two laser peaks at distinct wavelengths of 1 μm and 1.5 μm in this geometry. In terms of performance, the dual core fibre presented here has a long way

to go with the scopes to scale the output powers up to the current state of the art fibre lasers, utilising its cladding pumping geometry which is essential for power scaling applications. The current state of the art fibre lasers have been demonstrated with the maximum power of the range of 10kW [141] with the slope efficiencies reaching the quantum defects and it is only expected to be going higher with new innovations in the fibre design. The work presented here, however, is a novel idea of realising multi-wavelength lasers and still is in its infancy stage. In its current form, it represents a new generation of fibres which could mature into a compact source of multi-wavelength lasers, with huge potentials for power scaling. As described in section 4.5, this dual wavelength fibre laser could stand out in terms of serving myriad of applications such a dual wavelength LIDAR systems and multi-element sensing, which currently need a rather complex and bulky setups. The performance of this first of its kind dual wavelength fibre laser can be improved by implementing further design improvements. The current performance of this system has been limited by the very low reflectivity off the output facet, which serves as a ~4% reflective output coupler at the silica-air interface. This issue can be immediately addressed by incorporating high reflectivity output couplers. Fibre Bragg gratings (FBG) are the most viable and widely used output couplers used in fibre lasers and it could be implemented in this case as well. The FBGs for this application would need to be custom made in a multimode fibre with diameter relatively close to the two core fibre, with gratings inscribed for peak reflectivities at 1536 nm and 1030 nm. This would create a highly compact, all-fibre based monolithic resonator cavity with expected improved slope efficiency. In order to power scale the system to the state of the art fibre lasers, further improvements in the pumping mechanism would be inevitable. One way to achieve it would be by incorporating a n x 1 splitter scheme, where n fibre coupled diodes could be coupled into the active fibre for increasing the pump power.

The fibre design in terms of core configuration could be further altered in order to achieve the most optimum pump to core interaction for maximum efficiency.

4.6 Summary

This chapter discussed the theoretical and experimental details on the multicore fibre work. Light propagation in multicore fibres has been discussed in details with emphasis on the two core fibre design. Characterisation work on various multicore fibres have been carried out including loss measurements and lifetime measurements.

The two different types of fibres studied in details were the six core erbium doped fibre and the ytterbium and erbium-ytterbium doped two core fibre. The six core fibre was studied for gain measurements with the aim to develop an active multiplexer which combines amplification and multiplexer applications. The cores showed gains up to 30-40 dB in the wavelength range 1500 nm to 1600 nm. One out of six cores also showed lasing with Fresnel reflection and ring cavity configuration.

The two core fibre was developed with the aim to demonstrate dual wavelength lasing operating at 1 µm and 1.5 µm. Both the cores showed simultaneous lasing with a common pump of 976 nm, operating at 1060 nm and 1536 nm with Fresnel reflection. The slope efficiency was considerably low which could be expected for Fresnel reflection cavity lasing. Further improvement in the performance is expected with the incorporation of a ring cavity and fibre Bragg gratings.

Chapter 5

YTTERBIUM DOPED BISMUTHATE GLASSES FOR ULTRAFST LASERS

5.1 Introduction

Ultrafast Laser Inscription (ULI) technique has established itself as a versatile tool for the development of waveguide lasers and has paved the way for the miniaturisation of solid-state lasers. One of the most important factors which has made ULI technique such a success is its flexibility to work with almost any transparent material with the same laser. With suitable optimisation of the laser parameters, the ULI technique has proved to be a great tool for inscribing waveguides in different hosts for the applications in active devices such as waveguide lasers and amplifiers [81], and passive devices such as splitters and photonic lanterns [142]. Some of the other important host materials which have been recognised as host materials are phosphate glasses [81] that have been doped with rare-earth ions and fluoro-germanate ZBLAN glasses [143, 144]. Silica based rare-earth doped materials have also been studied for ULI based applications, but have not gained a lot of popularity for their certain limitations. They are known to have limited amplifier bandwidth and high level of rare-earth doping concentrations also is difficult to achieve with them. In order to overcome these limitations, few options have been explored. For example, telluride glasses for applications in broadband amplifiers and L-band amplifiers have been studied [145, 146]. Fluoride glass has been studied for thulium-doped fibres to improve power conversion efficiency at the S-band [147], because it has small phonon energy and prevents phonon relaxation into the intermediate energy level of Tm^{3+}. Phosphate glasses have also been studied for erbium doped fibres[148] and waveguides.

One of the other material which has emerged as a host material for ULI based waveguide inscription are the bismuthate (Bi_2O_3) based glasses. These glasses have shown to have wide and flat gain spectrum and high Er-solubility. An erbium doped waveguide amplifier with the peak internal gain per unit length of 2.3 dB cm^{-1} at 1533 nm was demonstrated by [149]. The substrate was further optimised to demonstrate an ultrafast waveguide laser operating at 1560 nm, with pulse-width of around 320 fs from a carbon nano-tube (CNT) mode-locked cavity [150]. Other than erbium, bismuthate glasses have also been studied for ytterbium dopants. Ytterbium doped bismuthate glasses had been developed earlier by Asahi Glass Company and a fibre laser action was demonstrated with a slope efficiency of 36% [10]. Some of the unique spectroscopic properties of Yb-doped bismuthate glass which make the yb-doped bismuthate glasses a great candidate for ULI based applications are the absence of detrimental defect zones in the system and the high Yb solubility; further supported by the success in fibre laser development.

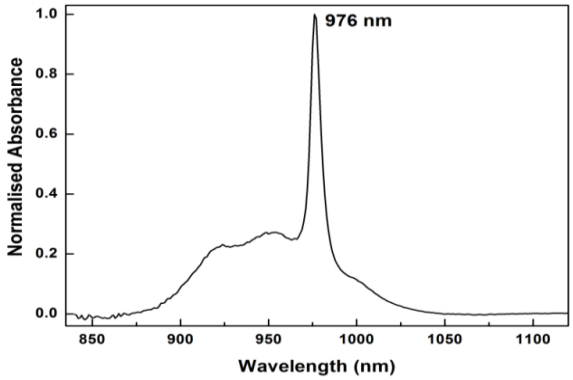

Figure 5. 1: Absorption spectrum of Yb doped bismuthate glass, with the peak absorption at 976 nm[5]

The glasses used in the experiments were prepared by Asahi Glass Company in Japan. The figure below shows the absorption spectrum for the Yb doped bismuthate glass

measured by Shimadzu UV-3100 spectrometer. The absorption band around 976 nm arises from the electronic transition from $^2F_{7/2}$ to $^2F_{5/2}$ in Yb^{3+} ions.

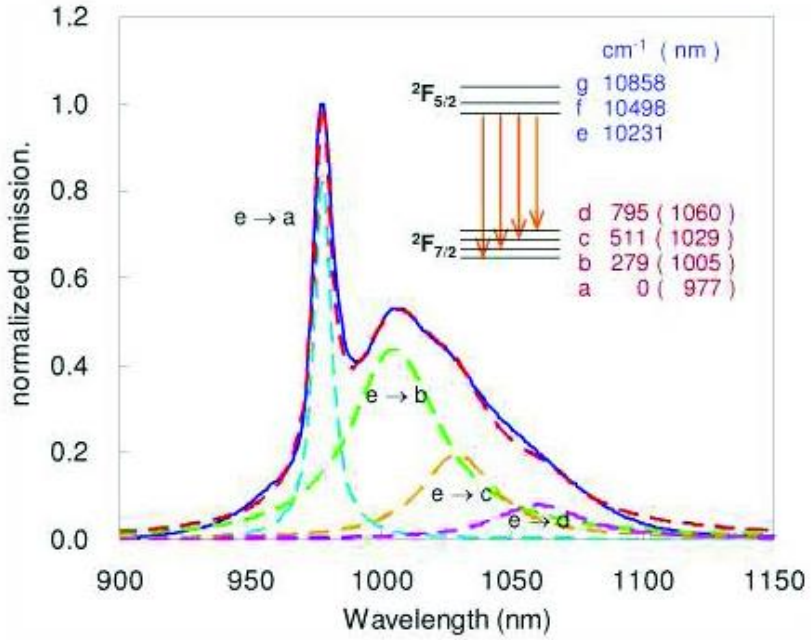

Figure 5. 2: Emission spectrum of Yb^{3+} doped Bi_2O_3-based glass pumped at 976 nm [10]

Figure 5.2 above shows the normalised emission spectrum for the Yb doped bismuthate glass. The energy levels of Yb^{3+} are shown in the figure's inset. The four Stark levels in $^2F_{7/2}$ are labelled a-d, and three Stark levels in $^2F_{5/2}$ are labelled e-g. The narrow line at 976 nm is attributed to the transition labelled a to e. The transitions a to f and a to g are also observed, with centre wavelengths of 953 nm and 921 nm, respectively.

5.2 Waveguide fabrication

As discussed in section 2.5, waveguides are fabricated in the substrates by focussing a beam of an ultrafast laser beam into the substrate and translating it in the predefined direction, depending on the desired shape of the waveguide. The waveguide

fabrication process needs to be well controlled and precise in order to achieve the reproducibility of the waveguide performance.

In order to achieve the best performance from the waveguides, it is important to optimise the inscription parameters. This optimisation process is carried out to identify the suitable parameters such as irradiation of the laser beam, translation speed of the sample, and number of scans required. These parameters determine the size and shape of the waveguides, which eventually define their guidance properties. A wide parameter scan is performed on the substrate to achieve an optimal window. The inscription laser used was a master-oscillator power-amplifier fibre (MOPA) laser supplied by IMRA. The laser emits pulses of ~350 fs duration centred at the wavelength of 1047 nm. The waveguides were written at a depth of 200-300 μm in the sample. A transverse writing configuration was employed for the inscription, where the sample was translated through the laser focus in a direction perpendicular to the incident laser beam. The waveguide asymmetry inherent to this writing geometry was corrected by using the well-established multiscan technique [151]. The details of the inscription set up have been discussed in section 2.5.2. The parameter scan included the variation in inscription laser power, scan speeds, and number of scans, keeping the pulse repetition rate at 1 MHz, pulse duration at 350 fs, and the laser polarisation at circular.

After the inscription process, the first step towards characterising the waveguides was to observe the waveguide cross-sections under a white light microscope working in transmission mode. This simple analysis provides an estimate of the physical dimensions of the waveguides and also the type of laser induced modification. Usually, the positive change in the refractive index is identified as a bright spot under the microscope, as the positive modification acts as the guiding region for the light.

The laser induced material damage manifests as dark, non-guiding regions. Figure 5.3 shows the cross-sectional view of the two waveguides inscribed at two different powers. The tear-drop shape in Figure 5.3 (a), consisting of a central elongated region flanked by an outer ring, is very characteristic of the waveguides inscribed at high repetition rates. This change in waveguide cross-section can be attributed to thermal accumulation effects typical at these repetition rates. At 5 MHz, the time interval between subsequent pulses falling on the substrate becomes much lesser than the thermal diffusion time of ~ 1 μs, resulting in an accumulation of heat at the focus. Following laser exposure, the accumulated heat gets transferred to the surrounding, extending the laser-heated region far beyond the focal volume. The central elongated region can be attributed to the high temperatures accompanying pulse absorption, and the surrounding ring due to thermal diffusion that occurs at an erratic rate due to the incomplete cooling between pulses. The effect of pulse repetition rates on the modification has been studied in details by Rose Mary [5]. The effect of the pulse repetition rate is not apparent in Figure 5.3 (b), as this waveguide was inscribed at a much lower power.

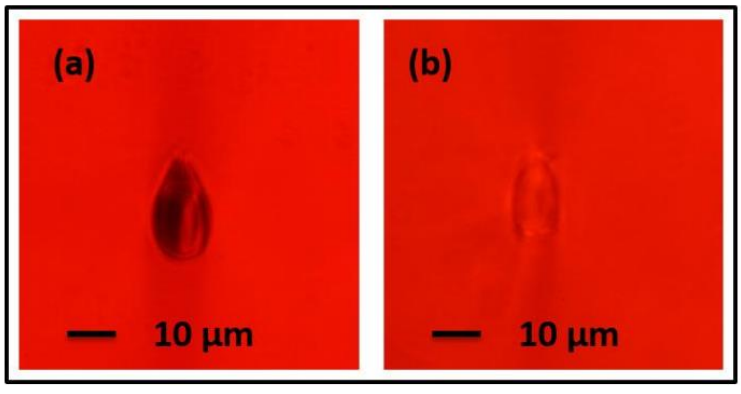

Figure 5. 3: Cross-sectional view of wavguides with (a) damaged none guiding core and (b) guiding Type I waveguide[5]

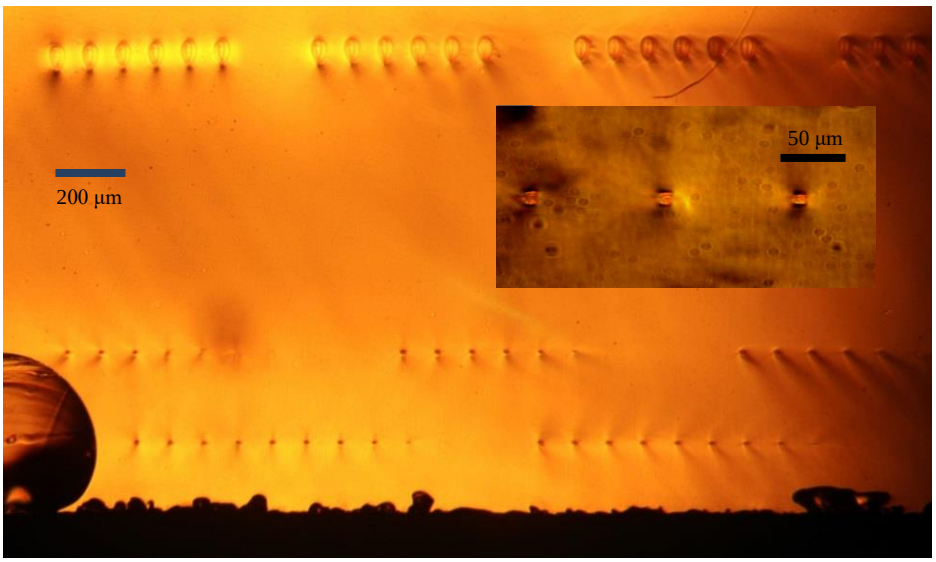

Figure 5. 4: Microscopic image of the cross section of the sample facet with waveguides inscribed with different parameters

Figure 5.4 above shows the cross-sectional microscopic view of the Yb-doped glass used for parameter scan. Multiple waveguides were inscribed with different parameters at different depths of 200 microns and 500 microns in the sample. The waveguides were then studied for their propagation properties by pumping them with the 976 nm laser. The mode images of the waveguides have been show in Figure 5.5. The waveguides were imaged in order to determine the best waveguides for the desired laser operation.

The table below summarises the list of parameters that were scanned for the optimisation of the desired waveguide properties. The aim was to achieve low-loss, single mode waveguides with the aim to fabricate a CW modelocked waveguide laser.

Parameter	**Range**
Number of scans	12, 14, 16, 18
Scan speeds (mm/sec)	3, 4, 5
Inscription laser power (mW)	33, 35, 37
Rep rate	1 MHz
Pulse duration	350 fs
Polarisation	Circular

Table 5. 1: Waveguide inscription parameters

In order to check the modal nature of the waveguides, pump wavelength at 976 nm was launched into all the waveguides and the guided modes were imaged. From the mode images shown below in Figure 5.4, it is evident that the waveguides inscribed at 33 mW and with the scan numbers 12 and 14 seemed to be single mode at the pump wavelength. Figure 5.4 below shows the mode images of the first forty waveguides. It can be seen that waveguides 1 to 10 are single mode, except waveguide number 6. Waveguide 6 is multimode possibly because of a scan overlap occurred during the inscription process. With the increase in power and number of scans, the waveguides start to exhibit multimode behaviour, as is evident from the pictures of waveguide 13 and so on.

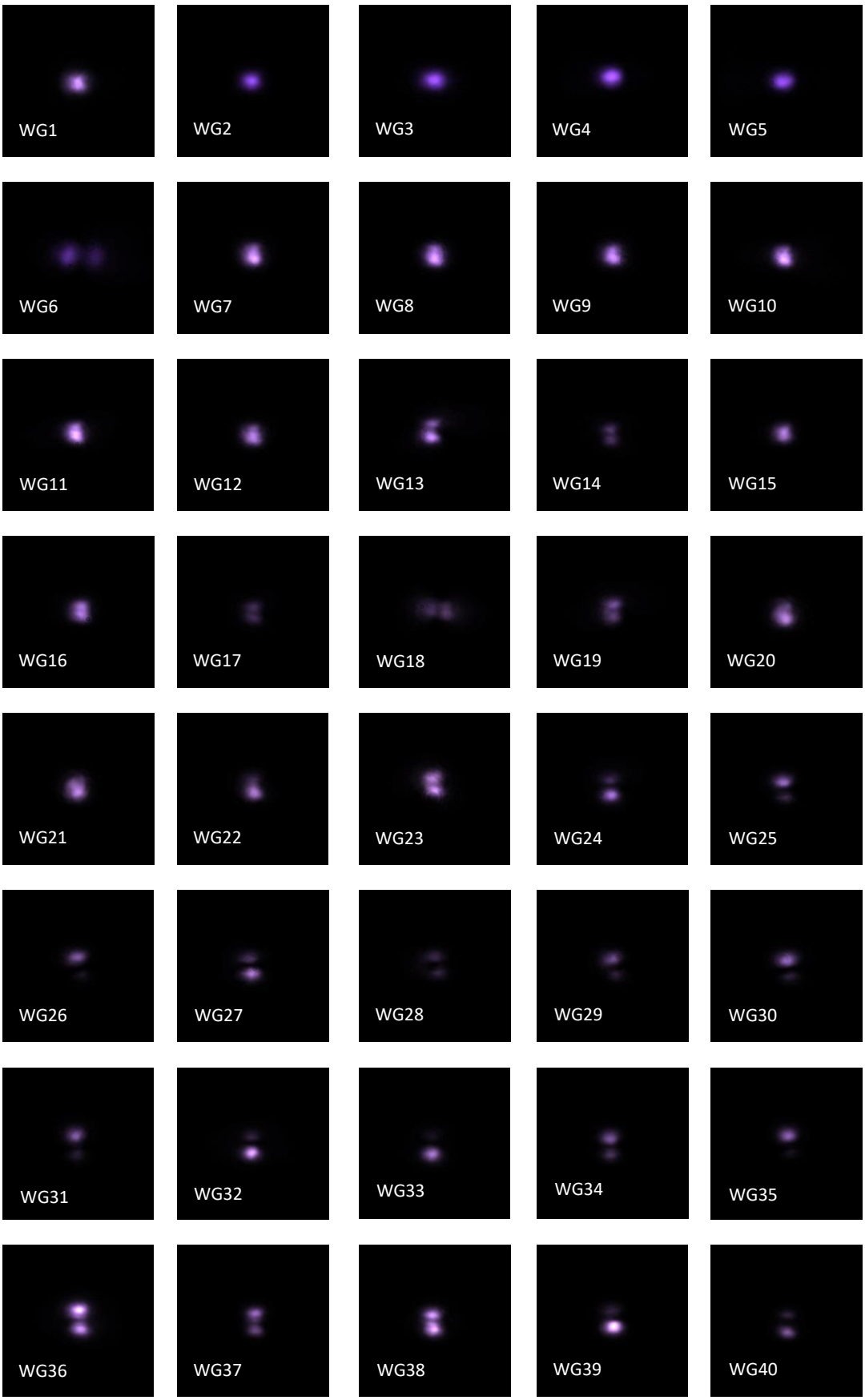

Figure 5. 5: Mode images of waveguides inscribed for parameter scan

5.3 Yb:bismuthate waveguide CW laser

The biggest motivation behind designing a waveguide based laser is to realise a compact and miniaturised monolithic laser system. The narrow confinement of the light in the waveguide, and the polished perpendicular facets allow a relatively simple cavity design, with the pump mirrors and output couplers sandwiching the waveguide containing substrate. CW laser action has been demonstrated earlier by [152] with this cavity design.

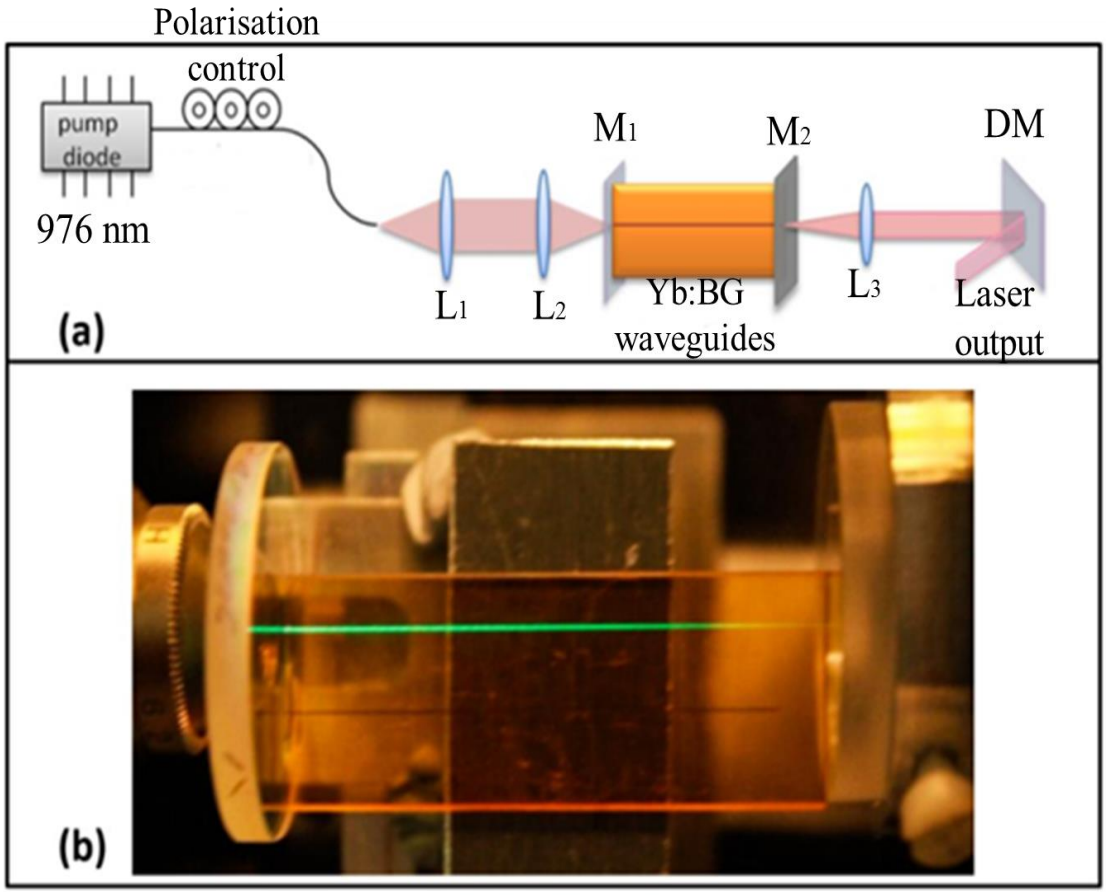

Figure 5. 6: (a) Schematic of the laser cavity to achieve laser operation at 1030 nm. M1: Pump mirror, M2: Output coupler, DM: dichroic mirror to separate the pump and laser signal, L1, L2 and L3 : lenses. (b) Photograph of the linear integrated cavity. Green upconversion at the pump wavelength can be observed along the waveguide length [5].

This was the first ever demonstration of a waveguide laser in Yb doped bismuthate glass and it achieved slope efficiency as high as 81%, which is close to the quantum

defect limited value. The maximum output power achieved was 163 mW for an output coupling of 30% with the corresponding slope efficiency of 79%.

5.4 Yb:bismuthate waveguide ultrafast laser

The relatively simple design of the waveguide lasers have influenced and encouraged the development of compact ultrafast lasers. ULI based ultrafast lasers offer increasing levels of integration with ever decreasing footprints in comparison to their optical fibre counterparts. These compact ultrafast lasers can be used for the realisation of stable frequency combs with applications in optical clocks and metrology [153]. Other than that, they have immense applications in optical communications [154], optical sampling [155], nonlinear microscopy [156], and high-precision spectroscopy [157]. These applications require ultrafast laser sources with pulse repetition rates of many GHz, with the properties such as power scalability at low noise performance, mass producibility, and low cost. A lot of research has gone into developing sources that could meet these requirements over the last decade. The semiconductor ridge-waveguide lasers [158] and vertical external cavity surface emitting semiconductor lasers (VECSELs) [159] were developed with high pulse repetition rate operation. Modelocking, however, involves faster gain dynamics and therefore these devices suffer from a high timing jitter up to the picosecond level [160]. This could be overcome by the active modelocking semiconductor lasers [161], but it results in longer pulse durations and complicated setups due to the requirements of external electronic control. Multi-GHz pulses have been achieved with harmonic modelocking in fibres [162], solid state lasers [163], and semiconductors [164]. Stability is a major issue with these ultrafast laser sources because of the presence of multiple pulses in the cavity and is a lot less stable than fundamental modelocking. Due to engineering difficulties it can be challenging to achieve a laser with a fundamental pulse repetition

rate greater than 1 GHz with a standard bulk cavity solid state laser system because the fundamental pulse repetition frequency (PRF) is directly linked to the optical cavity length [165]. Ultrafast laser inscribed waveguides have proven to be a great way to miniaturise the cavity lengths to a few millimetres, facilitating the realisation of multi-GHz repetition rate lasers.

Ultrafast waveguide lasers have been demonstrated with a range of host materials doped with a range of rare-earth ions. Erbium doped bismuthate glass waveguide lasers have been demonstrated by [150] with a pulse duration of 320 fs. A repetition rate of 11.5 GHz has been demonstrated by [166] in Nd:YAG operating at 1064 nm.

Graphene along with carbon nano-tubes (CNT) have emerged as promising candidates for the development of passively Q-switched [167] and modelocked lasers [168-171]. A monolithic ultrafast waveguide laser system was demonstrated by [43] in the Yb-doped bismuthate glass operating at 1.5 GHz repetition rate at 1039 nm wavelength. A graphene film based saturable absorber was used to achieve a passive Q-switched laser. Semiconductor saturable absorber mirrors (SESAMs) have also been used as an effective tool for passive modelocking over the years. They allow for very simple, self-starting passive modelocking of ultrafast solid-state lasers. They have triggered an unprecedented improvement in pulse widths, average power, and repetition rates in these lasers. It has allowed for many new practical application and commercialization of these lasers, increasing their use not only in R&D environments but also in medical, industrial, metrology and communications applications. Multiple reports of passive modelocking of waveguide lasers using SESAMs have come out over the decade [172-176].

5.5 Experimental Setup

The experimental setup for the modelocking experiment primarily consisted of two polarisation maintaining fibre coupled 975 nm diode lasers, which were combined using polarisation multiplexing, collimating and focussing optics, ULI inscribed waveguide sample and SESAM. The schematic of the setup is shown below in Figure 5.7.

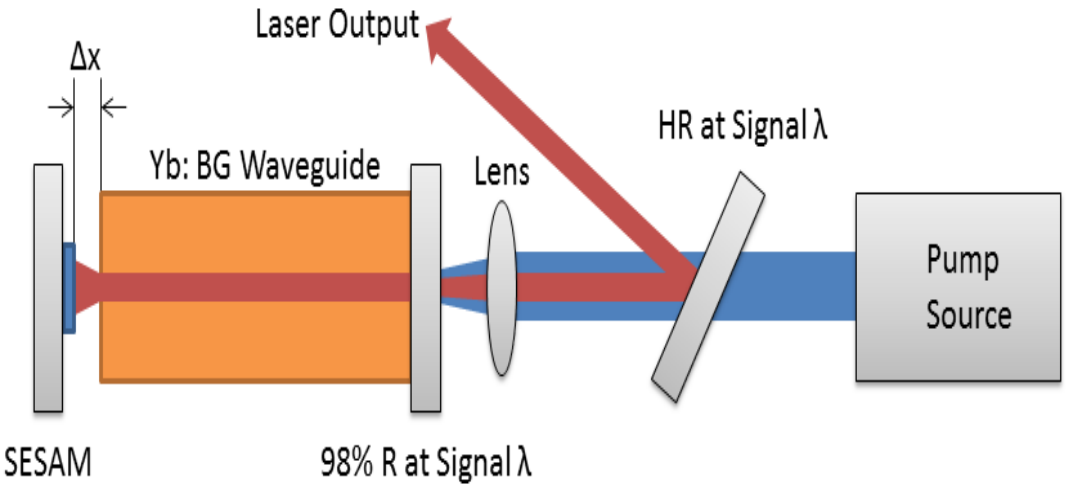

Figure 5.7: Schematic of laser cavity design used in the demonstration of CW modelocking in Yb:BG

An 11 mm AR coated lens was used to couple the pump light into the end facet of the waveguide. This lens also collimated the laser output. A 98 % reflective mirror was used as the output coupler which was butt-coupled to the sample end facet with index-matching fluid to reduce Fresnel reflections. The SESAM (Batop GmbH) used in this work had an initial reflection of 99.3% at 1050 nm, a modulation depth of 0.4 %, saturation fleuence of 90 $\mu J/cm^2$ and a relaxation time of 0.5 ps. The SESAM was mounted on a translation stage with manual adjustment and a piezo electric stage to allow fine control of the air gap Δx. The diagnostic tools included an autocorrelator, an ultrafast photodetector, a radio frequency spectrum analyser, and a power meter.

On initial alignment the system demonstrated Q-switched modelocking but with very fine adjustment of Δx with the piezoelectric motion controller CW modelocking was observed with a pump power of 800 mW. CW modelocking was confirmed by the RF spectrum shown in Figure 5.8 below.

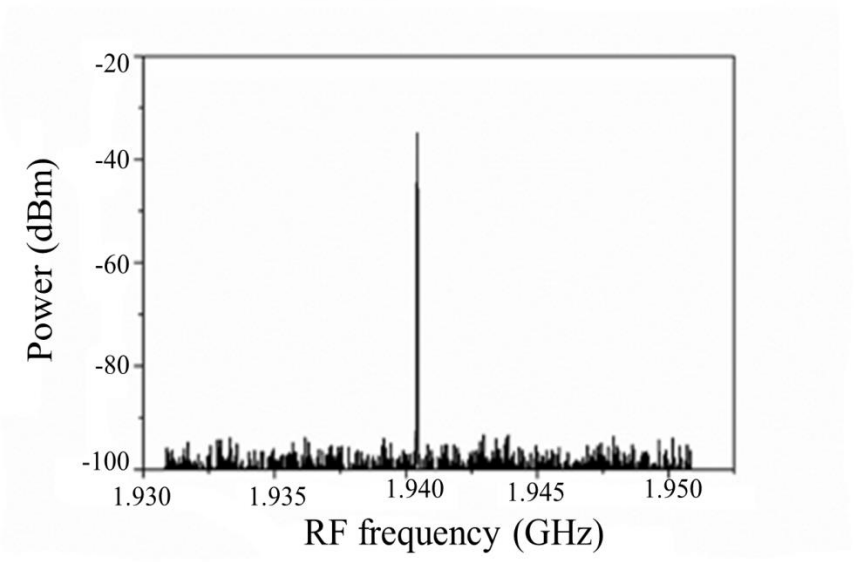

Figure 5. 8: Radio Frequency spectrum of Yb:BG in CW modelocked operation with 800 mW of pump light incident on the end facet of the waveguide

From the RF spectrum, the laser was found to have a PRF of 1.94 GHz which is in good agreement with the cavity length. The average output power of the laser was measured to be 60 mW with an incident pump power of 800 mW.

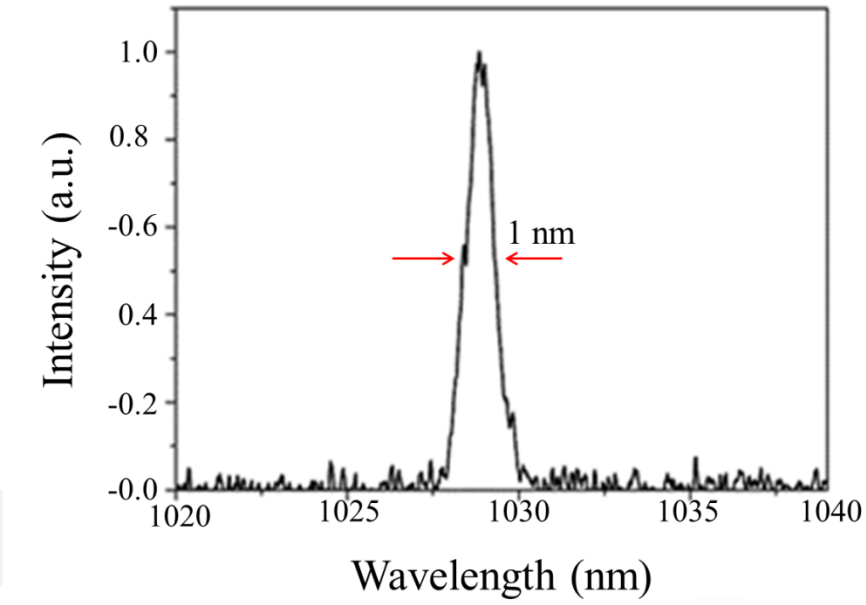

Figure 5. 9: Spectra of CW modelocked Yb:BG laser operating under 800 mW of pump excitation. The spectra was centered at 1029 nm with a FWHM of 1 nm.

The wavelength spectrum of the laser was measured using an OSA with a resolution of 0.1 nm. The spectrum of the laser during CW modelocked operation is shown in Figure 5.9. The laser emission was centred at 1029 nm with a FWHM of 1 nm. From the FWHM of 1 nm we infer that the pulse duration was 1.1 ps, assuming a $sech^2$ transform-limited pulse.

This work uses the work carried out by [174] in which they have demonstrated a fundamentally modelocked femtosecond laser in Yb:IOG-1 with a pulse repetition rate of 15.2 GHz by manipulating the air gap between the waveguide output facet and the SESAM. They have reported that the group velocity dispersion (GVD) can be controlled by accurately changing the length of the air gap, as shown in Figure 5.7. This can be attributed to a soliton formation mechanism in the cavity, i.e. when the pulse phase shift due to self-phase modulation (SPM) in the gain medium is compensated by negative group velocity dispersion (GVD). The required negative

GVD in this experiment originates from the micron-scale gaps between the SESAM and uncoated surfaces of the waveguide structure. This leads to the formation of equivalent Gires-Tournois interferometer (GTI) structures [177] that provide a sufficient amount of negative GVD suitable to support a soliton mode-locking regime, as was previously shown in the case of a bulk laser system [178].

5.6 Summary

This chapter discussed the demonstration of a CW modelocked Yb doped bismuthate glass waveguide laser employing a quasi-monolithic cavity configuration. The ultrashort pulses were generated with a compact cavity incorporating a SESAM with the output coupler. The laser operated in Q-switched mode-locking regime, but with further tuning of the cavity, CW modelocking was achieved. The air gap between the sample facet and the SESAM was tuned to achieve a fundamentally modelocked laser with pulse width of around 1.1 ps operating at 1.94 GHz.

Chapter 6

CONCLUSIONS AND FUTURE WORK

6.1 Conclusion

Rare-earth elements have been well established as a versatile candidate for photonic applications. They have been investigated for decades and have been incorporated in a myriad ways for moving the photonics revolution ahead.

The work presented in this thesis focuses on the application of rare-earth doped elements for the realisation of novel photonic devices. The research work encompasses different areas of photonics including fibre optics, solid state lasers, and ultrafast laser inscription incorporating rare-earth elements. The rare-earth elements have been used in specialty optical fibres to create the next generation of fibre-optic devices with applications in multi-wavelength lasers. Ultrafast modelocked lasers have been realised with the rare-earth doped waveguide lasers. Studies on rare-earth doped glasses have also been carried out with applications in the realisation of multi-wavelength visible lasers.

Chapter 2 discusses in detail the materials and techniques used for the research work. It describes the details of the materials used and their preparation methods. Rare-earth elements have been introduced and their properties have been discussed. Samarium phosphate glasses have been prepared via melt-quenching technique for applications into visible lasers. Multicore fibres have been fabricated by the MCVD process. The details of the steps involved have been presented and dual core fibres with Er-Yb and Yb doped cores have been successfully fabricated. With the aim to miniaturise the ultrafast laser sources, ULI technique has been introduced and discussed which has been used to fabricate channel waveguides in glass substrates to demonstrate compact

ultrafast lasers. Yb doped bismuthate glasses have been used to fabricate buried waveguides in them to realise compact ultrafast lasers operating at 1 micron.

Chapter 3 presents the research on trivalent samarium ions for the applications in visible lasers. The spectroscopic characteristics of the ions have been discussed briefly in order to understand its optical properties. The glasses were pumped with temperature controlled laser diodes operating at 405 nm and 479 nm. Slight amplification in the signal was observed with the side pumping, but laser action could not be realised. It was inferred that with higher pump absorption, laser operation could be achieved. Excited state absorption (ESA) studies were carried out at 479 nm and its presence was detected. The ESA was accompanied with bleaching effects, which were inferred to be the deterring factors for lasing action in the samples.

Chapter 4 details the work carried out on multicore fibres for the realisation of multi-wavelength lasers. A brief theoretical background of multicore fibres has been presented. Multicore fibres have been characterised for modal and propagation properties. The fibres have been characterised and finally the design of a two-core fibre with Er/Yb and Yb doped cores has been demonstrated to emit dual-wavelength operation at 1536 nm and 1061 nm simultaneously with common pumping. This multi-wavelength operation has applications in multi-element sensing and LIDAR systems.

Chapter 5 discusses the CW modelocked Yb doped waveguide laser with a quasi-monolithic cavity. The modelocking has been achieved with a SESAM as a saturable mirror. A repetition rate of 1.94 GHz was achieved with the cavity with a pulse woth of around 1.1 ps operating at 1 micron wavelength.

6.2 Future work

The rare-earth elements always have proved to be the go-to materials for the next generation photonic applications. The work presented in this thesis has demonstrated that these elements are quite versatile and can be used in quite different ways. The work on samarium doped glasses has shown promising results and given a deeper insight into the deterring factors against the realisation of lasing action. In order to achieve a laser operation in the visible range, the future work would involve a deeper study into changing the optical properties of the material. It would incorporate tailored changes in the concentrations of the ions and further tuning of the host materials in order to red-shift the peak absorption of the material from the violet range to the blue range. This would facilitate the higher pump power for the realisation of laser operation, owing to the availability of high power laser diodes operating at blue wavelengths.

The multicore fibre work has given promising results with multi-wavelength laser operation realised just with a Fresnel reflection based cavity. There is a lot of scope to improve the performance of this system, first of which being the incorporating of a fibre Bragg grating (FBG) based cavity. The slope efficiency of the cavity is expected to increase many fold with lower output coupling through the FBG. The work on the two core fibre could be furthered by introducing more cores and hence, different dopants in the fibre in order to increase the span of the wavelength range. Elements like thulium and holmium can be introduced in the same fibre to extend the wavelength range up to 2 micron from the same fibre. Future work with the multicore fibre would also incorporate ULI by fabricating fan-out devices in order to incorporate a quasi-monolithic cavity configuration.

The work on the modelocked waveguide laser has promising applications and has the potential to be improved. Single mode waveguides inscribed in the substrate could result in a much more stable modelocked system. The future of this work would be to realise a compact and completely monolithic laser system with the waveguides, operating in multi-GHz repetition rate regime. This could be achieved by incorporating the saturable absorber and resonator cavity elements with the substrate.

REFERENCES

1. Voncken, J.H.L., *The Rare Earth Elements: An Introduction*. 2016: Springer International Publishing.
2. www.fiberlabs-inc.com/technology/, Fiber Labs Inc.
3. Kenyon, A.J., *Recent developments in rare-earth doped materials for optoelectronics.* Progress in Quantum Electronics, 2002. **26**(4–5): p. 225-284.
4. Halder, A., *Theoretical and experimental studies of optical and multifunctional lasing properties of rare-earth, semi-metal and noble-metal doped specialty optical fibers in nano-engineered glass hosts* in *Fiber Optics and Photonics Division*. 2015, CSIR-CGCRI: Kolkata.
5. Mary, R., *Compact Near-Infrared 3-Dimensional Channel Waveguide Lasers*, in *IPaQS*. 2014, Heriot Watt University.
6. Psaila, N.D., et al., *Er:Yb-doped oxyfluoride silicate glass waveguide amplifier fabricated using femtosecond laser inscription.* Applied Physics Letters, 2007. **90**(13): p. 131102.
7. Torchia, G.A., et al., *Highly efficient laser action in femtosecond-written Nd:yttrium aluminum garnet ceramic waveguides.* Applied Physics Letters, 2008. **92**(11): p. 111103.
8. Lancaster, A., et al., *Mid-infrared laser emission from Fe:ZnSe cladding waveguides.* Applied Physics Letters, 2015. **107**(3): p. 031108.
9. Marzahl, D.-T., et al., *Spectroscopy and laser operation of Sm^{3+}-doped lithium lutetium tetrafluoride ($LiLuF_4$) and strontium hexaaluminate ($SrAl_{12}O_{19}$).* Optics Express, 2015. **23**(16): p. 21118-21127.
10. Ohara, S. and Y. Kuroiwa, *Highly ytterbium-doped bismuth-oxide-based fiber.* Optics Express, 2009. **17**(16): p. 14104-14108.
11. Maxwell, J.C. and J.J. Thompson, *A Treatise on Electricity and Magnetism*. 1904: Clarendon.
12. Einstein, A., *Zur Quantentheorie der Strahlung.* Physikalische Zeitschrift, 1917. **18**: p. 121-128.
13. Maiman, T.H., *Stimulated Optical Radiation in Ruby.* Nature, 1960. **187**(4736): p. 493-494.

14. Javan, A., W.R. Bennett, and D.R. Herriott, *Population Inversion and Continuous Optical Maser Oscillation in a Gas Discharge Containing a He-Ne Mixture.* Physical Review Letters, 1961. **6**(3): p. 106-110.
15. Pavesi, L., et al., *Optical gain in silicon nanocrystals.* Nature, 2000. **408**(6811): p. 440-444.
16. Pereira, L.F.R., *Organic Light Emitting Diodes: The Use of Rare Earth and Transition Metals*. 2012: Pan Stanford Publishing.
17. Poole, S., et al., *Fabrication and characterization of low-loss optical fibers containing rare-earth ions.* Journal of Lightwave Technology, 1986. **4**(7): p. 870-876.
18. Vienne, G.G., et al., *Fabrication and Characterization of $Yb3^{+}$: Er^{3+} Phosphosilicate Fibers for Lasers.* Journal of Lightwave Technology, 1998. **16**(11): p. 1990.
19. Fermann, M.E., et al., *Efficient operation of an Yb-sensitised Er fibre laser at 1.56 μm.* Electronics Letters, 1988. **24**(18): p. 1135-1136.
20. Vijaya, N., K. Upendra Kumar, and C.K. Jayasankar, *$Dy^{(3+)}$-doped zinc fluorophosphate glasses for white luminescence applications.* Spectrochim Acta A Mol Biomol Spectrosc, 2013. **113**: p. 145-53.
21. Bonomi, C. *Rare Earth Elements: perhaps not everyone knows that ….* December 7, 2015; Available from: http://etn.redmud.org/rare-earth-elements/.
22. Dieke, G.H. and H.M. Crosswhite, *The Spectra of the Doubly and Triply Ionized Rare Earths.* Applied Optics, 1963. **2**(7): p. 675-686.
23. Snitzer, E., *Optical Maser Action of Nd^{+3} in a Barium Crown Glass.* Physical Review Letters, 1961. **7**(12): p. 444-446.
24. Geusic, J.E., H.M. Marcos, and L.G.V. Uitert, *Laser Oscillations In Nd-Doped Yttrium Aluminum, Yttrium Gallium And Gadolinium Garnets.* Applied Physics Letters, 1964. **4**(10): p. 182-184.
25. Noyori, K.S., et al., *The characteristics of experimental laser coagulations of the retina.* Archives of Ophthalmology, 1964. **72**(2): p. 254-263.
26. Minton, J.P., M. Zelen, and A.S. Ketcham, *Experimental Results From Exposure Of Cloudman S-91 Melanoma In The Cdba/2f1 Hybrid Mouse To Neodymium Or Ruby Laser Radiation.* Annals of the New York Academy of Sciences, 1965. **122**(2): p. 758-766.
27. Hanna, D.C., et al., *Continuous-wave oscillation of a monomode ytterbium-doped fibre laser.* Electronics Letters, 1988. **24**(17): p. 1111-1113.

28. Lacovara, P., et al., *Room-temperature diode-pumped Yb:YAG laser*. Optics Letters, 1991. **16**(14): p. 1089-1091.
29. DeLoach, L.D., et al., *Evaluation of absorption and emission properties of Yb^{3+} doped crystals for laser applications.* IEEE Journal of Quantum Electronics, 1993. **29**(4): p. 1179-1191.
30. Myslinski, P., D. Nguyen, and J. Chrostowski, *Effects of concentration on the performance of erbium-doped fiber amplifiers.* Journal of Lightwave Technology, 1997. **15**(1): p. 112-120.
31. Sanchez-Martin, J.A., et al., *Amplifiers and Lasers Based on Erbium-Doped Photonic Crystal Fiber: Simulation and Experiments.* IEEE Journal of Quantum Electronics, 2012. **48**(3): p. 338-344.
32. Honkanen, S., et al. *High Er concentration phosphate glasses for planar waveguide amplifiers*. 1997.
33. Mears, R.J., et al. *Low-noise erbium-doped fibre amplifier operating at 1.54μm*. Electronics Letters, 1987. **23**, 1026-1028.
34. Desurvire, E., J.R. Simpson, and P.C. Becker, *High-gain erbium-doped traveling-wave fiber amplifier.* Optics Letters, 1987. **12**(11): p. 888-890.
35. Bowman, S.R., S. O'Connor, and N.J. Condon, *Diode pumped yellow dysprosium lasers.* Optics Express, 2012. **20**(12): p. 12906-12911.
36. Gün, T., P. Metz, and G. Huber, *Power scaling of laser diode pumped Pr^{3+}:$LiYF_4$ cw lasers: efficient laser operation at 522.6 nm, 545.9 nm, 607.2 nm, and 639.5 nm.* Optics Letters, 2011. **36**(6): p. 1002-1004.
37. Calmano, T., et al. *Ultrafast Laser Inscribed Pr:KY_3F_{10} Waveguides for Dual Wavelength and Switchable Waveguide Lasers in the Visible*. in *Advanced Solid State Lasers*. 2015. Berlin: Optical Society of America.
38. Xu, B., et al., *Highly efficient InGaN-LD-pumped bulk Pr:YLF orange laser at 607nm.* Optics Communications, 2013. **305**: p. 96-99.
39. Kaminskii, A.A., et al., *New laser properties and spectroscopy of orthorhombic crystals $YAlO_3$:Er_{3+}. Intensity luminescence characteristics, stimulated emission, and full set of squared reduced-matrix elements* $|\langle \alpha[SL]\, J|\, |U(t)||\alpha'[S'\, L']\, J'\rangle|^2$ *for Er^{3+} Ions.* physica status solidi (a), 1995. **151**(1): p. 231-255.
40. Mary, R., et al., *Compact, highly efficient ytterbium doped bismuthate glass waveguide laser.* Optics Letters, 2012. **37**(10): p. 1691-1693.

41. Ren, Y., et al., *Continuous wave channel waveguide lasers in Nd:$LuVO_4$ fabricated by direct femtosecond laser writing.* Opt Express, 2012. **20**(3): p. 1969-74.
42. Kojou, J., et al., *Wavelength tunable Q-switch laser in visible region with Pr^{3+}-doped fluoride-glass fiber pumped by GaN diode laser.* Optics Communications, 2013. **290**: p. 136-140.
43. Mary, R., et al., *1.5 GHz picosecond pulse generation from a monolithic waveguide laser with a graphene-film saturable output coupler.* Optics Express, 2013. **21**(7): p. 7943-7950.
44. Choudhary, A., et al., *Diode-pumped femtosecond solid-state waveguide laser with a 4.94 GHz pulse repetition rate.* Optics Letters, 2012. **37**(21): p. 4416-4418.
45. Steckl, A.J. and J.M. Zavada, *Photonic Applications of Rare-Earth-Doped Materials.* MRS Bulletin, 2013. **24**(9): p. 16-20.
46. Digonnet, M.J.F., *Rare-Earth-Doped Fiber Lasers and Amplifiers, Revised and Expanded*. 2001: CRC Press.
47. Katkova, M.A. and M.N. Bochkarev, *New trends in design of electroluminescent rare earth metallo-complexes for OLEDs.* Dalton Transactions, 2010. **39**(29): p. 6599-6612.
48. Mears, R.J., Reekie, L., Jauncey, I.M. and Payne, D.N., *High-gain rare-earth-doped fibre amplifier at 1.54μm*, in *International Conference on Integrated Optics and Optical Fiber Communication/Conference on Optical Fiber Communication (IOOC/OFC)*. 1987: United States.
49. Grasso, V.B., *Rare Earth Elements in National Defense: Background, Oversight Issues, and Options for Congress* C.R. Service, Editor. 2013.
50. Charalampides, G., et al., *Rare Earth Elements: Industrial Applications and Economic Dependency of Europe.* Procedia Economics and Finance, 2015. **24**: p. 126-135.
51. Bünzli, J.-C.G., et al., *New Opportunities for Lanthanide Luminescence.* Journal of Rare Earths, 2007. **25**(3): p. 257-274.
52. Wang, Y., et al., *Recent development in rare earth doped phosphors for white light emitting diodes.* Journal of Rare Earths, 2015. **33**(1): p. 1-12.
53. Extavour, M. *Rare Earth Elements: High Demand, Uncertain Supply*. 2011; Available from: https://www.osa-

opn.org/home/articles/volume_22/issue_7/features/rare_earth_elements_high_demand,_uncertain_supply/.

54. Eliseeva, S.V. and J.-C.G. Bunzli, *Rare earths: jewels for functional materials of the future.* New Journal of Chemistry, 2011. **35**(6): p. 1165-1176.
55. Poole, S.B., et al., *Characterization of special fibers and fiber devices.* Journal of Lightwave Technology, 1989. **7**(8): p. 1242-1255.
56. Royon, R., et al., *High power, continuous-wave ytterbium-doped fiber laser tunable from 976 to 1120 nm.* Optics Express, 2013. **21**(11): p. 13818-13823.
57. Farries, M.C., P.R. Morkel, and J.E. Townsend, *Samarium^{3+}-doped glass laser operating at 651 nm.* Electronics Letters, 1988. **24**(11): p. 709-711.
58. Jayasimhadri, M., et al., *Spectroscopic characteristics of Sm^{3+}-doped alkali fluorophosphate glasses.* Spectrochim Acta A Mol Biomol Spectrosc, 2006. **64**(4): p. 939-44.
59. Davis, K.M., et al., *Writing waveguides in glass with a femtosecond laser.* Optics Letters, 1996. **21**(21): p. 1729-1731.
60. DiGiovanni, D. *Specialty fiber: novel fibers for devices*. in *OFC 2003 Optical Fiber Communications Conference, 2003.* 2003.
61. *Editors A2 - Méndez, Alexis*, in *Specialty Optical Fibers Handbook*, T.F. Morse, Editor. 2007, Academic Press: Burlington. p. xxiii.
62. Choudhury, D., J.R. Macdonald, and A.K. Kar, *Ultrafast laser inscription: perspectives on future integrated applications.* Laser & Photonics Reviews, 2014. **8**(6): p. 827-846.
63. Jha, N., et al. *Multicore Optical Fibers for Multi-band Laser and Amplifier*. in *12th International Conference on Fiber Optics and Photonics*. 2014. Kharagpur: Optical Society of America.
64. Barrett, S.D. and S.S. Dhesi, *The Structure of Rare-Earth Metal Surfaces*. 2001.
65. Reisfeld, R., *Radiative and non-radiative transitions of rare-earth ions in glasses*, in *Rare Earths*. 1975, Springer Berlin Heidelberg: Berlin, Heidelberg. p. 123-175.
66. Li, J., et al., *Light Emission from Rare-Earth Doped Silicon Nanostructures.* Advances in Optical Technologies, 2008. **2008**: p. 10.
67. Roschuk, T., et al., *Lighting Applications of Rare Earth-Doped Silicon Oxides*, in *Silicon Nanocrystals*. 2010, Wiley-VCH Verlag GmbH & Co. KGaA. p. 487-506.

68. Ennen, H., et al., *Photoluminescence excitation measurements on GaAs:Er grown by molecular-beam epitaxy.* Journal of Applied Physics, 1987. **61**(10): p. 4877-4879.
69. Bantien, F., E. Bauser, and J. Weber, *Incorporation of erbium in GaAs by liquid-phase epitaxy.* Journal of Applied Physics, 1987. **61**(8): p. 2803-2806.
70. Levin, T.M., et al., *Low-energy cathodoluminescence spectroscopy of erbium-doped gallium nitride surfaces.* Journal of Vacuum Science & Technology A: Vacuum, Surfaces, and Films, 1999. **17**(6): p. 3437-3442.
71. Suratwala, T.I., et al., *Effects of OH content, water vapor pressure, and temperature on sub-critical crack growth in phosphate glass.* Journal of Non-Crystalline Solids, 2000. **263–264**: p. 213-227.
72. Venkatramu, V., et al., *Optical spectroscopy of Sm^{3+} ions in phosphate and fluorophosphate glasses.* Optical Materials, 2007. **29**(11): p. 1429-1439.
73. Marzahl, D.T., et al., *Spectroscopy and laser operation of $Sm^{(3+)}$-doped lithium lutetium tetrafluoride (LiLuF(4)) and strontium hexaaluminate (SrAl(12)O(19)).* Opt Express, 2015. **23**(16): p. 21118-27.
74. Naftaly, M. and A. Jha, *Nd^{3+}-doped fluoroaluminate glasses for a 1.3 μm amplifier*. Journal of Applied Physics, 2000. **87**(5): p. 2098-2104.
75. Kao, K.C. and G.A. Hockham, *Dielectric-fibre surface waveguides for optical frequencies.* Electrical Engineers, Proceedings of the Institution of, 1966. **113**(7): p. 1151-1158.
76. Nagel, S., J. MacChesney, and K. Walker, *An overview of the modified chemical vapor deposition (MCVD) process and performance.* IEEE Journal of Quantum Electronics, 1982. **18**(4): p. 459-476.
77. Dhar, A., *Fabrication of rare earth doped optical fibre using MCVD process*. Lambert academic publishing, Saarbruchen, Germany. 2010.
78. Bhadra, S. and A. Ghatak, *Guided Wave Optics and Photonic Devices*. 2016: CRC Press.
79. Paul, M.C., *Fabrication and radiation response behaviour of optical fibers*. Lambert academic publishing, Saarbruchen, Germany. 2012.
80. Townsend, J.E., S.B. Poole, and D.N. Payne, *Solution-doping technique for fabrication of rare-earth-doped optical fibres.* Electronics Letters, 1987. **23**(7): p. 329-331.

81. Valle, G.D., R. Osellame, and P. Laporta, *Micromachining of photonic devices by femtosecond laser pulses.* Journal of Optics A: Pure and Applied Optics, 2009. **11**(1): p. 013001.
82. Siebenmorgen, J., et al., *Highly efficient Yb:YAG channel waveguide laser written with a femtosecond-laser.* Optics Express, 2010. **18**(15): p. 16035-16041.
83. Burghoff, J., et al., *Efficient frequency doubling in femtosecond laser-written waveguides in lithium niobate.* Applied Physics Letters, 2006. **89**(8): p. 081108.
84. Stuart, B.C., et al., *Nanosecond-to-femtosecond laser-induced breakdown in dielectrics.* Physical Review B, 1996. **53**(4): p. 1749-1761.
85. C. B. Schaffer, A.B., and E. Mazur, *Laser-induced breakdown and damage in bulk transparent materials induced by tightly focused femtosecond laser pulses.* Meas. Sci. Technol. , (12): p. 1784-1794
86. Du, D., et al., *Laser-induced breakdown by impact ionization in SiO_2 with pulse widths from 7 ns to 150 fs.* Applied Physics Letters, 1994. **64**(23): p. 3071-3073.
87. Macdonald, J.R., et al., *Ultrafast laser inscription of near-infrared waveguides in polycrystalline ZnSe.* Optics Letters, 2010. **35**(23): p. 4036-4038.
88. Macdonald, J.R., et al., *Efficient mid-infrared Cr:ZnSe channel waveguide laser operating at 2486 nm.* Optics Letters, 2013. **38**(13): p. 2194-2196.
89. C. HnatovskyR.S. TaylorEmail authorE. SimovaP.P. RajeevD.M. RaynerV.R. Bhardwaj, a.P.B.C., *Fabrication of microchannels in glass using focused femtosecond laser radiation and selective chemical etching.* 2006. **84**(1): p. 47–61.
90. Rose, H., Ber. Akad. Wiss. Berlin, 1847. **1847**: p. 131-132.
91. Lecoq de Boisbaudran, P.E., Compt. Rend., 1879. **89**: p. 212-214.
92. Roscoe, H.E. and C. Schorlemmer, *A Treatise on Chemistry*. 1907. p. 782.
93. Nicolaou, K.C., S.P. Ellery, and J.S. Chen, Angew. Chem. Int. Ed., 2009. **48**: p. 7140-7165.
94. Finlay, I.G., M.D. Mason, and M. Shelley, Lancet Oncol., 2005. **6**: p. 392-400.
95. Thornton, J.R., et al., *Properties of Neodymium Laser Materials.* Applied Optics, 1969. **8**(6): p. 1087-1102.
96. J. Kido, K.N., Y. Okamoto and T. Skotheim, *Electroluminescence in a terbium complex.* Chem. Lett., 1990. **220**(4): p. 657-660.

97. J. Kido, K.N., Y. Okamoto and T. Skotheim, *Electroluminescence from polysilane film doped with europium complex.* Chem. Lett., 1992: p. 1267-1270.

98. Zellmer, H., P. Riedel, and A. Tünnermann, *Visible upconversion lasers in praseodymium-ytterbium-doped fibers.* Applied Physics B, 1999. **69**(5): p. 417-421.

99. B, E.M., A. Senin, and J.G. Eden. *Upconversion green fiber amplifier*. in *2001 Digest of LEOS Summer Topical Meetings: Advanced Semiconductor Lasers and Applications/Ultraviolet and Blue Lasers and Their Applications/Ultralong Haul DWDM Transmission and Networking/WDM Compo*. 2001.

100. Funk, D.S. and J.G. Eden, *Glass-fiber lasers in the ultraviolet and visible.* IEEE Journal of Selected Topics in Quantum Electronics, 1995. **1**(3): p. 784-791.

101. Jha, N., et al. *Sm^{3+} Ions Doped Phosphate Glasses for Multiband Visible Laser Applications*. in *CLEO: 2015*. 2015. San Jose, California: Optical Society of America.

102. Gün, T., P. Metz, and G. Huber, *Efficient continuous wave deep ultraviolet Pr^{3+}:$LiYF_4$ laser at 261.3 nm.* Applied Physics Letters, 2011. **99**(18): p. 181103.

103. Sharma, Y.K., et al., *Spectroscopic and radiative properties of Sm^{3+} doped zinc fluoride borophosphate glasses.* Materials Science and Engineering: B, 2005. **119**(2): p. 131-135.

104. Zhang, L., et al., *Spectroscopic properties of Sm^{3+}-doped phosphate glasses.* Journal of Materials Research, 2012. **27**(16): p. 2111-2115.

105. Souza Filho, A.G., et al., *Optical properties of Sm^{3+} doped lead fluoroborate glasses.* Journal of Physics and Chemistry of Solids, 2000. **61**(9): p. 1535-1542.

106. Kumar, A., D.K. Rai, and S.B. Rai, *Optical properties of Sm^{3+} ions doped in tellurite glass.* Spectrochimica Acta Part A: Molecular and Biomolecular Spectroscopy, 2003. **59**(5): p. 917-925.

107. Lin, H., et al., *Optical absorption and photoluminescence in Sm^{3+}- and Eu^{3+}-doped rare-earth borate glasses.* Journal of Luminescence, 2005. **113**(1-2): p. 121-128.

108. Dijk, J.M.F.v. and M.F.H. Schuurmans, *On the nonradiative and radiative decay rates and a modified exponential energy gap law for 4f–4f transitions in rare-earth ions.* The Journal of Chemical Physics, 1983. **78**(9): p. 5317-5323.

109. Pekgözlü, İ., et al., *Synthesis and Photoluminescence Properties of Sr2Be2B2O7 Doped with Dy^{3+}, Sm^{3+}, Tb^{3+}, and Pb^{2+}*. Journal of Applied Spectroscopy, 2016. **83**(3): p. 504-511.

110. Dominiak-Dzik, G., *Sm^{3+}-doped $LiNbO_3$ crystal, optical properties and emission cross-sections.* Journal of Alloys and Compounds, 2005. **391**(1–2): p. 26-32.

111. Gruber, J.B., B. Zandi, and M.F. Reid, *Spectra, energy levels, and transition line strengths for $Sm^{3+}Y_3Al_5O_{12}$.* Physical Review B, 1999. **60**(23): p. 15643-15653.

112. Ams, M., D.J. Little, and M.J. Withford, *10 - Femtosecond-laser-induced refractive index modifications for photonic device processing A2 - Vainos, Nikolaos A*, in *Laser Growth and Processing of Photonic Devices*. 2012, Woodhead Publishing. p. 305-332.

113. Gorieva, V., S. Korableva, and V. Semashko, *Excited-state absorption spectra of Pr3+ ions doped into LiY0.3Lu0.7F4 mixed crystal.* Optical Materials Express, 2016. **6**(4): p. 1146-1150.

114. Morkel, P.R. and R.I. Laming, *Theoretical modeling of erbium-doped fiber amplifiers with excited-state absorption.* Optics Letters, 1989. **14**(19): p. 1062-1064.

115. Burshtein, Z., et al., *Excited-state absorption studies of Cr^{4+} ions in several garnet host crystals.* IEEE Journal of Quantum Electronics, 1998. **34**(2): p. 292-299.

116. H. Rohde, S.S., E. Gottwald, and K. Kloppe, *"Next generation optical access: 1 Gbit/s for everyone*, in *Proceedings of 35th European Conference and Exhibition on Optical Communication (ECOC, 2009)*. 2009: Vienna, Austria.

117. Iano, S., et al. *Multicore optical fiber*. in *Optical Fiber Communication*. 1979. Washington, D.C.: Optical Society of America.

118. Richardson, D.J., J.M. Fini, and L.E. Nelson, *Space-division multiplexing in optical fibres.* Nature Photonics, 2013. **7**(5): p. 354-362.

119. Antonio-Lopez, J.E., et al., *Multicore fiber sensor for high-temperature applications up to 1000°C.* Optics Letters, 2014. **39**(15): p. 4309-4312.

120. Moore, J.P. and M.D. Rogge, *Shape sensing using multi-core fiber optic cable and parametric curve solutions.* Optics Express, 2012. **20**(3): p. 2967-2973.
121. Newkirk, A.V., et al., *Multicore Fiber Sensors for Simultaneous Measurement of Force and Temperature.* IEEE Photonics Technology Letters, 2015. **27**(14): p. 1523-1526.
122. Abedin, K.S., et al., *Amplification and noise properties of an erbium-doped multicore fiber amplifier.* Optics Express, 2011. **19**(17): p. 16715-16721.
123. Sakaguchi, J., et al., *19-core MCF transmission system using EDFA with shared core pumping coupled via free-space optics.* Optics Express, 2014. **22**(1): p. 90-95.
124. Bookey, H.T., et al., *Multiple rare earth emissions in a multicore tellurite fiber with a single pump wavelength.* Optics Express, 2007. **15**(26): p. 17554-17561.
125. Abedin, K.S., et al., *Multicore Erbium Doped Fiber Amplifiers for Space Division Multiplexing Systems.* Journal of Lightwave Technology, 2014. **32**(16): p. 2800-2808.
126. Snitzer, E., *Cylindrical Dielectric Waveguide Modes*.* Journal of the Optical Society of America, 1961. **51**(5): p. 491-498.
127. Marcuse, D., *Light transmission optics.* 1972.
128. Marcuse, D., *Theory of Dielectric Optical Waveguides*. 2013: Elsevier Science.
129. Saleh, B.E.A. and M.C. Teich, *Fundamentals of Photonics*. 2007: Wiley.
130. Bookey, H., et al., *Multiple rare earth emissions in a multicore tellurite fiber with a single pump wavelength.* Optics express, 2007. **15**(26): p. 17554-17561.
131. Birks, T.A., et al., *"Photonic lantern" spectral filters in multi-core fibre.* Optics Express, 2012. **20**(13): p. 13996-14008.
132. Kishi, N. and E. Yamashita. *A simple coupled-mode analysis method for multiple-core optical fiber and coupled dielectric waveguide structures*. in *1988., IEEE MTT-S International Microwave Symposium Digest*. 1988.
133. Koshiba, M., et al., *Multi-core fiber design and analysis: coupled-mode theory and coupled-power theory.* Opt Express, 2011. **19**(26): p. B102-11.
134. Yamashita, E., Y. Nishino, and K. Atsuki. *Analysis of Multiple Dielectric Wave Guide Systems with Extended Point-Matching Method*. in *1983 IEEE MTT-S International Microwave Symposium Digest*. 1983.
135. Kishi, N., E. Yamashita, and K. Atsuki, *Modal and coupling field analysis of optical fibers with circularly distributed multiple cores and a central core.* Journal of Lightwave Technology, 1986. **4**(8): p. 991-996.

136. Saitoh, K., et al., *Crosstalk and Core Density in Uncoupled Multicore Fibers.* IEEE Photonics Technology Letters, 2012. **24**(21): p. 1898-1901.
137. Koshiba, M., K. Saitoh, and Y. Kokubun, *Heterogeneous multi-core fibers: proposal and design principle.* IEICE Electronics Express, 2009. **6**(2): p. 98-103.
138. Joanna, M., S. George, and W. Gillian, *Design of a tunable L-band multi-wavelength laser system for application to gas spectroscopy.* Measurement Science and Technology, 2006. **17**(5): p. 1023.
139. Jauregui-Vazquez, D., et al., *A multi-wavelength erbium-doped fiber ring laser using an intrinsic Fabry–Perot interferometer.* Laser Physics, 2016. **26**(10): p. 105105.
140. Moon, D.S., et al., *Multi-wavelength linear-cavity tunable fiber laser using a chirped fiber Bragg grating and a few-mode fiber Bragg grating.* Optics Express, 2005. **13**(15): p. 5614-5620.
141. Richardson, D.J., J. Nilsson, and W.A. Clarkson, *High power fiber lasers: current status and future perspectives [Invited]*. Journal of the Optical Society of America B, 2010. **27**(11): p. B63-B92.
142. Thomson, R.R., et al., *Ultrafast laser inscription of an integrated photonic lantern.* Optics Express, 2011. **19**(6): p. 5698-5705.
143. Lancaster, D.G., et al., *2.1 μm waveguide laser fabricated by femtosecond laser direct-writing in Ho^{3+}, Tm^{3+}:ZBLAN glass.* Optics Letters, 2012. **37**(6): p. 996-998.
144. Fusari, F., et al., *Lasing action at around 1.9 μm from an ultrafast laser inscribed Tm-doped glass waveguide.* Optics Letters, 2011. **36**(9): p. 1566-1568.
145. Ohishi, Y., et al., *Gain characteristics of tellurite-based erbium-doped fiber amplifiers for 1.5-μm broadband amplification.* Optics Letters, 1998. **23**(4): p. 274-276.
146. Yamada, M., et al., *Gain-flattened tellurite-based EDFA with a flat amplification bandwidth of 76 nm.* IEEE Photonics Technology Letters, 1998. **10**(9): p. 1244-1246.
147. Aozasa, S., et al., *Gain-shifted TDFA employing high concentration doping technique with high internal power conversion efficiency of 70%.* Electronics Letters, 2002. **38**(8): p. 361-363.

148. Jiang, S., et al., *Er3+-doped phosphate glasses for fiber amplifiers with high gain per unit length.* Journal of Non-Crystalline Solids, 2000. **263-264**(Supplement C): p. 364-368.
149. Thomson, R.R., et al., *Ultrafast laser inscription of a high-gain Er-doped bismuthate glass waveguide amplifier.* Optics Express, 2010. **18**(12): p. 13212-13219.
150. Beecher, S.J., et al., *320 fs pulse generation from an ultrafast laser inscribed waveguide laser mode-locked by a nanotube saturable absorber.* Applied Physics Letters, 2010. **97**(11): p. 111114.
151. Nasu, Y., M. Kohtoku, and Y. Hibino, *Low-loss waveguides written with a femtosecond laser for flexible interconnection in a planar light-wave circuit.* Optics Letters, 2005. **30**(7): p. 723-725.
152. Mary, R., et al. *Yb-doped Bismuthate Glass waveguide laser fabricated by Ultrafast Laser Inscription*. in *Lasers, Sources, and Related Photonic Devices*. 2012. San Diego, California: Optical Society of America.
153. Jones, D.J., et al., *Carrier-Envelope Phase Control of Femtosecond Mode-Locked Lasers and Direct Optical Frequency Synthesis.* Science, 2000. **288**(5466): p. 635-639.
154. Chai, Y.J., et al., *1.36-Tb/s spectral slicing source based on a Cr^{4+}-YAG femtosecond laser*. Journal of Lightwave Technology, 2005. **23**(3): p. 1319-1324.
155. Bartels, A., et al., *Ultrafast time-domain spectroscopy based on high-speed asynchronous optical sampling.* Review of Scientific Instruments, 2007. **78**(3): p. 035107.
156. Chu, S.-W., et al., *Real-time second-harmonic-generation microscopy based on a 2-GHz repetition rate Ti:sapphire laser.* Optics Express, 2003. **11**(8): p. 933-938.
157. Diddams, S.A., L. Hollberg, and V. Mbele, *Molecular fingerprinting with the resolved modes of a femtosecond laser frequency comb.* Nature, 2007. **445**: p. 627.
158. Brown, C.T.A., et al., *Compact laser-diode-based femtosecond sources.* New Journal of Physics, 2004. **6**(1): p. 175.
159. Wilcox, K.G., et al., *High Peak Power Femtosecond Pulse Passively Mode-Locked Vertical-External-Cavity Surface-Emitting Laser.* IEEE Photonics Technology Letters, 2010. **22**(14): p. 1021-1023.

160. Tourrenc, J.P., et al., *Experimental investigation of the timing jitter in self-pulsating quantum-dash lasers operating at 1.55 μm.* Optics Express, 2008. **16**(22): p. 17706-17713.
161. Gee, S., et al., *Self-Stabilization of an Actively Mode-Locked Semiconductor-Based Fiber-Ring Laser for Ultralow Jitter.* IEEE Photonics Technology Letters, 2007. **19**(7): p. 498-500.
162. Grudinin, A.B. and S. Gray, *Passive harmonic mode locking in soliton fiber lasers.* Journal of the Optical Society of America B, 1997. **14**(1): p. 144-154.
163. Chen, Y.F., et al., *High-power subpicosecond harmonically mode-locked Yb:YAG laser with pulse repetition rate up to 240 GHz.* Laser Physics Letters, 2013. **10**(1): p. 015803.
164. Quarterman, A.H., et al., *Passively harmonically mode-locked vertical-external-cavity surface-emitting laser emitting 1.1 ps pulses at 147 GHz repetition rate.* Applied Physics Letters, 2010. **97**(25): p. 251101.
165. Keller, U., *Recent developments in compact ultrafast lasers.* Nature, 2003. **424**(6950): p. 831-8.
166. Obraztsov, P.A., et al., *Multi-gigahertz repetition rate ultrafast waveguide lasers mode-locked with graphene saturable absorbers.* Laser Physics, 2016. **26**(8): p. 084008.
167. Popa, D., et al., *Graphene Q-switched, tunable fiber laser.* Applied Physics Letters, 2011. **98**(7): p. 073106.
168. Popa, D., et al., *74-fs nanotube-mode-locked fiber laser.* Applied Physics Letters, 2012. **101**(15): p. 153107.
169. Sun, Z., et al., *Graphene Mode-Locked Ultrafast Laser.* ACS Nano, 2010. **4**(2): p. 803-810.
170. Ma, J., et al., *Graphene mode-locked femtosecond laser at 2μm wavelength.* Optics Letters, 2012. **37**(11): p. 2085-2087.
171. Wang, F., et al., *Wideband-tuneable, nanotube mode-locked, fibre laser.* Nature Nanotechnology, 2008. **3**: p. 738.
172. Choudhary, A., et al., *A diode-pumped 1.5 μm waveguide laser mode-locked at 6.8 GHz by a quantum dot SESAM.* Laser Physics Letters, 2013. **10**(10): p. 105803.
173. Choudhary, A., et al. *Near- infrared, mode-locked waveguide lasers with multi-GHz repetition rates*. in *SPIE LASE*. 2014. SPIE.

174. Lagatsky, A.A., et al., *Fundamentally mode-locked, femtosecond waveguide oscillators with multi-gigahertz repetition frequencies up to 15 GHz.* Optics Express, 2013. **21**(17): p. 19608-19614.
175. Schlager, J.B., et al., *Passively mode-locked waveguide laser with low residual jitter.* IEEE Photonics Technology Letters, 2002. **14**(9): p. 1351-1353.
176. Schlager, J.B., et al., *Passively mode-locked glass waveguide laser with 14-fs timing jitter.* Optics Letters, 2003. **28**(23): p. 2411-2413.
177. Kuhl, J. and J. Heppner, *Compression of femtosecond optical pulses with dielectric multilayer interferometers.* IEEE Journal of Quantum Electronics, 1986. **22**(1): p. 182-185.
178. Krainer, L., et al., *77 GHz soliton modelocked Nd:YVO_4 laser.* Electronics Letters, 2000. **36**(22): p. 1846-1848.